Susanne Othilie Gulbrandsen

Modelling of An Offshore Wind Farm for Multi-Frequency Stability Analysis

June 2019

NTNU
Norwegian University of Science and Technology
Faculty of Information Technology and Electrical Engineering
Department of Electric Power Engineering

Master's thesis

2019

Susanne Othilie Gulbrandsen

Master's thesis

NTNU
Norwegian University of Science and Technology

NTNU
Norwegian University of Science and Technology

NTNU

Norwegian University of
Science and Technology

Modelling of An Offshore Wind Farm for Multi-Frequency Stability Analysis

Susanne Othilie Gulbrandsen

Master of Energy and Environmental Engineering
Submission date: June 2019
Supervisor: Elisabetta Tedeschi, IEL
Co-supervisor: Fernando P. Marafão, São Paulo State University
Łukasz Kocewiak, Ørsted

Norwegian University of Science and Technology
Department of Electric Power Engineering

Abstract

In this master thesis, two functional simulation models that resemble the benchmark systems recently suggested by CIGRE's working group C4.49 *Multi-frequency stability of converter-based modern power systems* have been developed. The increasing complexity of the electrical infrastructure over the last years has turned out to introduce new challenges related to multi-frequency stability in terms of interactions and resonances between physical components in the grid and the converter control. C4.49 is established to describe the phenomenon and explain available *methods* for analyses, in addition to provide a common understanding on modelling, analysis, evaluation, and mitigation methods. The scope of this master thesis is to make a contribution to C4.49 related to the modelling.

The benchmark systems represent power electronic dominated grids where both power generators and loads are interfaced by power electronic converters. The system design suggested by C4.49 is not limited to a certain type of power source. However, it has been chosen for this thesis to treat the generating units in the benchmark systems as wind turbines. The first system consists solely of a single generating unit connected to an ideal voltage source, while the second system is built up of two converter configurations connected to the grid. The two converter configurations in the second system are in this thesis representing a cluster of 58 wind turbines. To make the model as realistic as possible, parameter data from the Hornsea Project ONE wind power plant has been used. The design of the converters' control system is derived from a methodology-based approach and has been explained thoroughly.

The modelling process revealed a challenge with the up-scaled representation of a single wind turbine with the chosen control strategy. The trouble, which introduced a tremendous amount of harmonic distortion to the system, is believed to originate from an increased difference in the energy storage capability of the filter inductors and filter capacitor. The problem was solved by adjusting the voltage level on the DC side of the converter. Investigation indicated that the reason for the successful adjustment of the DC voltage was a sufficient regulation of an uncontrolled power flow between the two converter sides due to the large filter capacitance. Seen from the grid, the representation of the filter impedance is adequate. However, the problem is not expected to be present in real-life applications as the wind farm in reality consists of many separate units with a much lower ratio between the inductance and capacitance. The finding is considered as a weakness with the model which is worth being highlighted and discussed.

A frequency sweep of the converter model under different operating conditions showed a significant and hardly predictable variation in the impedance magnitude for frequencies below 200 Hz. In this region, the impedance was susceptible to all the various operating conditions applied.

Sammendrag

I denne masteroppgaven er det blitt utviklet to funksjonelle simuleringsmodeller som likner svært på modellene CIGREs arbeidsgruppe C4.49 *Multi-frequency stability of converter-based modern power systems* har designet. Den økende kompleksiteten i den elektriske kraftsystemet de siste årene har vist seg å introdusere nye utfordringer knyttet til fler-frekvens stabilitet i form av interaksjoner og resonans mellom passive komponenter i nettet og kontrollsystemet til omformere. C4.49 er etablert for å beskrive fenomenet og forklare tilgjengelige *metoder* for analyser, samt gi en felles forståelse av modellering, analyse, evaluering og metoder for redusere problemet. Formålet med denne masteroppgaven er å komme med et bidrag til C4.49 i forbindelse med modelleringen.

Systemene, som er designet for å illustrere problemet, representerer nett som er dominert av kraftelektronikk hvor både generatorer og laster er koblet sammen via omformere. Systemdesignet foreslått av C4.49 er ikke begrenset til én bestemt type genererende enhet. Likevel, er det for denne masteroppgaven blitt bestemt å betrakte de strømgenererende enhetene som vindturbiner. Det første systemet består kun av en enkelt genererende enhet koblet til en ideell spenningskilde, mens det andre systemet er bygget opp av to omformerkonfigurasjoner som er koblet til kraftnettet. De to omformerkonfigurasjoner i det andre systemet representerer i denne masteren en samling av 58 vindturbiner. For å gjøre modellen så realistisk som mulig er det blitt benyttet parameterdata fra vindkraftverket HORNSEA Project ONE. Designet av omformernes kontrollsystem er utledet basert på metoder fra litteraturen og er blitt grundig forklart.

Modelleringsprosessen avdekket en utfordring med den oppskalerte representasjonen av en enkelt vindturbin, gitt den valgte kontrollstrategien. Problemet, som introduserte en enorm mengde harmonisk støy for systemet, er antatt å ha sin opprinnelse i en økt differanse mellom energilagringskapasiteten til filterinduktansen og filterkondensatoren. Problemet ble løst ved å justere spenningsnivået på DC-siden av omformeren. Undersøkelser indikerte at grunnen til den vellykkede justeringen av DC-spenningen skyldtes en tilstrekkelig regulering av en ukontrollert effektflyt mellom de to sidene av omformeren på grunn av den store filterkapasitansen. Den ekvivalente representasjonen av den samlede filterimpedansen er riktig sett fra nettet. Likevel forventes ikke problemet å oppstå i virkeligheten ettersom vindkraftverk i realiteten består av mange enkeltstående enheter med et mye lavere forhold mellom induktansen og kapasitansen. Funnene betraktes som en svakhet ved modellen som det er verdt å diskutere videre.

En frekvensskanning av omformerne under ulike driftsforhold viste en signifikant og lite forutsigbar variasjon i impedansen for frekvenser under 200 Hz. Impedansen var i denne regionen følsom for alle de ulike driftsforholdene som ble testet.

Preface

This master thesis is a completion of the five year integrated master program Energy and Environmental Engineering at the Norwegian University of Science and Technology (NTNU) with a specialization in electrical power systems/electrical energy conversion. The foundation for the understanding of the theoretical background of the thesis was laid autumn 2018 during the work with a project assignment on shunt active power filter as a harmonic mitigation method in offshore wind farms.

The master thesis is a part of the international research project NBPOCCREI: *Norwegian-Brazilian collaboration on Power theories and Cooperative Control of Renewable Energy Integration*. The thesis has been carried out in cooperation with São Paulo State University (UNESP) and two and a half months were spent at their campus in Sorocaba this spring.

Acknowledgements

The working process with this thesis has introduced me to several inspiring and incredibly competent people who all have been of vital importance for the final result. I am hugely grateful for their encouragement and all the time they have spent helping me.

I want to direct my thankfulness to Fernando P. Marafão and Augusto M. S. Alonso in Sorocaba for taking such good care of me and always being available for discussions related to my project. I am also very thankful for Danilo I. Brandão's availability. Next, I want to thank Łukasz H. Kocewiak and M. Kazem B. Dowlatabadi from Ørsted for discussions, explanations, and valuable insight into existing issues related to the integration of offshore wind farms. I do also want to thank my fellow student Jostein Gjevre, who challenged my way of meeting simulation issues, and friends and family, who have supported me through some intense months.

Last but not least, I want to express my deepest gratefulness to my supervisor Professor Elisabetta Tedeschi at the Department of Electrical Engineering at NTNU. Her guidance and help over the last year has been a vital source to inspiration and knowledge. I highly appreciate how her expectations has resulted in a steep learning curve and a very rewarding learning process.

Susanne Othilie Gulbrandsen
Trondheim, 27 June 2019

Contents

List of Figures

List of Tables

Abbreviations

2L-VSC	=	Two-level voltage source converter
BTB	=	Back-to-back
C4.49	=	Working group "Multi-frequency stability of converter-based modern power systems" established by CIGRE
CIGRE	=	Conseil International des Grands Réseaux Électriques (The International Council on Large Electric Systems)
EHV	=	Extra high voltage
FFT	=	Fast Fourier Transform
IEEE	=	Institute of Electrical and Electronics Engineers
IGBT	=	Insulated gate bipolar transistor
HV	=	High voltage
HVAC	=	High voltage alternating current
HVDC	=	High voltage direct current
LV	=	Low voltage
MV	=	Medium voltage
PI	=	Proportional-integral
PLL	=	Phase-locked loop
PCC	=	Point of Common Coupling
pu	=	Per unit
PWM	=	Pulse width modulator
TDD	=	Total demand distortion
THD	=	Total harmonic distortion
VSC	=	Voltage source converter

Chapter 1

Introduction

1.1 Background

There has been an exponential increase in the installed wind power capacity over the last couple of decades [1]. Being one of the fastest growing renewable energy technologies, wind energy is expected to become one of the major contributors to the generation of electricity in the future power industry [2]. Related to this development, the location of wind farms offshore has received more attention over the the last years. Since 2000, the installed capacity from offshore wind has increased from 67 MW to 18.7 GW in 2017. But this is only the beginning as another 500 GWs is recommended in the years to come in order to maintain an temperature increase of less than 2°C [1]. Due to more stable and stronger wind conditions in addition to less conflicts regarding available land, offshore wind industry has a tremendous potential [1, 3].

Despite that the principle of operation is the same regardless of whether the wind farms are located onshore or offshore, the improved wind conditions offshore come at a cost. The wind turbines offshore are typically connected through a widespread medium voltage (MV) cable system before the power is transformed and transmitted to the grid with long high voltage (HV) cables [4]. The more complex structure can, especially for high voltage alternating current (HVAC) connections, introduce critical resonance points in the lower frequency range and cause challenges related to harmonic amplification and propagation within the offshore wind farm [4–6]. Insufficient damping of the harmonic frequencies can affect the control of the wind turbine and hence be of concern for the overall stability of the system [4].

1.2 Requirements for the Wind Power Industry

A healthy operation of the power system requires a balance between consumption and generation of electricity. Based on predictions and forecasts, the producers will bid to the market. The

operators with the lowest marginal costs will cover the base loads while the peak hours will be covered by operators with higher marginal costs. As renewable energy such as wind power normally would have a marginal cost of zero, those units will always be used whenever available [7]. This economic characteristic is vital for the wind power energy in order to be competitive on the market as the energy source cannot be stored and thus has to be used whenever available. However, there are certain challenges that must be taken into consideration as the penetration of wind power connected to the grid is increasing. In order to ensure a safe and operational power system both during normal conditions and faults, it is important that the generating units can provide flexibility and regulation in terms of control of active and reactive power, adjust frequency and regulate voltage levels, power quality, harmonic levels, flickers, protection and fault-ride through [3]. Traditionally, this responsibility has been assigned to the conventional power plants with large synchronous generators. With the fast development in the wind industry and its increased implementation, there has been a need for a development of satisfactory grid code requirements for wind generation [8]. The overall trend of the development in the local grid codes is that the wind farms should be capable of providing the same control and regulation as conventional plants.

To comply with the grid codes, all wind turbines must have integrated converters. The full-scale back-to-back converter, often referred to in the literature as *Type 4*, is more and more commonly used in the offshore wind farm industry and is expected to take over the market [3,4]. This type of converter allows full decoupling of the wind turbine from the grid and can therefore operate at full speed range.

1.3 Amplification of Harmonics in Offshore Wind Power Systems

According to the grid codes, harmonic levels are one of the issues that the power plants should regulate. Usually, harmonics as a phenomenon is referred to as the steady-state harmonics generated from non-linear loads which are amplified by resonance points present in the system for the specific harmonic order. The acceptable level of those harmonics is well defined in grid code requirements such as the one recommended in the standard from the Institute of Electrical and Electronics Engineers (IEEE).

According to The International Council on Large Electric Systems (CIGRE), challenges with co-ordination and operation of grid-connected converters have arisen as a result of the increased implementation of power electronic equipment in high voltage systems [9]. Mainly due to relatively low damping, interaction of converter controllers with grid resonances appear and cause high harmonics in the grid [9]. This type of amplification of harmonic signals is different to the steady-state harmonics mentioned above. Thus, there is a need for different modelling, analysis techniques and mitigation methods to provide solutions to the problem [9].

1.3.1 CIGRE

CIGRE is a global community with the purpose of gathering the worldwide power system expertise to ensure an improvement and collaborative development in the field. It has the vision of being recognized as the leading global community in all aspects of the power system. Working groups are established to solve specific existing and future challenges related to the power system [10].

At the moment, there is no common practise on how to approach the problem regarding the interactions and resonances between physical components in the grid and the converter control. Therefore, CIGRE established a new working group (C4.49) on the topic in 2018 named *Multi-frequency stability of converter-based modern power systems* under the lead of Łukasz H. Kocewiak. The objective of the working group is to describe the phenomenon and explain available *methods* for analyses, in addition to provide a common understanding on modelling, analysis, evaluation, and mitigation methods [9]. In order to do so, the working group has designed two very simple benchmark systems to investigate the interactions between the different system components under various conditions.

1.4 Scope

The scope of this master thesis is to make a contribution to C4.49 related to the modelling of the benchmark systems which will be used to study the multi-frequency stability of converters. The objective can be divided into the four following parts:

1. Provide a background explanation of the problem of harmonic interactions in a power electronic dominated grid and shed light on the critical relevance of converter control in such application.

2. Build a simulation model that resembles the simplest benchmark system defined by C4.49 in Matlab/Simulink consisting of a converter configuration with filter connected to an ideal AC voltage source.

3. Build a modified version of the second benchmark system defined by C4.49 with focus on its two grid following converters. The converter configurations should represent the production from 30 and 28 wind turbines, respectively.

4. Analyse the frequency response of the load following converter representation in the benchmark systems. Discuss the implementation of an impedance model of the converters with the purpose of mapping the resonance points in the grid that potentially can lead to interactions between the grid and the converter control.

1.5 Structure of Thesis

In order to obtain the objective described above, the structure of the master thesis is as follows:

1. Chapter 2 - Background theory: Covers basic theory on harmonics and resonance to see how those two phenomena are closely related. The chapter also comments on different filtering techniques and introduces harmonic standards as a reference point.

2. Chapter 3 - Topology of benchmark systems: Topology of benchmark system 1 is presented with focus on the grid-connected converter including its LCL-filter and description on how the passive components can be sized. Further, the chapter introduces benchmark system 2 and any deviations from the original benchmark systems designed by C4.49. A list of system parameters and per-unit (pu) representation to be used in the simulation model is provided in the end.

3. Chapter 4 - Control theory for converter modelling: Provides a thorough explanation of the methodology applied when developing the simulation models of the benchmark systems.

4. Chapter 5 - Modelling approaches and limitations: Gives an overview of the cases to be tested during the construction of the simulation model and takes the reader through the milestones of the design process while presenting the corresponding results. Further, the chapter presents the results from frequency scans of the converters and how the response is obtained.

5. Chapter 6 - Discussion: Discusses the findings during the modelling process and from the frequency scan analysis.

6. Chapter 7 - Conclusion and suggestion for further work: Concludes the simulation modelling of the benchmark systems, comments on the frequency responses, and share thoughts for further work.

The benchmark systems are frequently addressed throughout the thesis. Unless otherwise is stressed, this is referring to the modified versions used in this thesis. Any deviations from the original models suggested by C4.49 are clearly described in Chapter 4 where the benchmark systems are introduced.

Chapter 2

Background Theory

In order to understand how to deal with the amplification of harmonics due to the issue related to interactions of converter controllers with grid resonances, the first part of the master thesis will look into the definitions of harmonics and resonance, and why they are closely related. Then, the concepts of passive and active filtering will be introduced to explain different approaches to mitigate harmonic distortion. The last section will be dedicated to harmonic standards to give an insight into the present requirements from the industry.

2.1 Harmonic Distortion

Today, the presence of non-linear loads in the grid is increasing [11]. The change in load structure has raised the concern about harmonic distortion in the grid, and the topic has received more attention lately [11]. Harmonics can cause interference with communication, increased losses, heating of devices, and cause malfunction of relays [11, 12]. Solutions to harmonic distortion are becoming more and more important to maintain a stable grid with a satisfactory power factor [11].

Harmonic distortion in the power industry is commonly referred to as the frequency components in a waveform that cause a sine-shaped voltage or current signal not to be perfectly sinusoidal. The major part of the distortion is called power system harmonics and is composed of sinusoidal voltage and current signals at frequencies that are integer multiples of the fundamental frequency [13].

Sources of harmonics in the power system are non-linear loads such as static converters, arc discharge devices, saturated magnetic devices, and to some extent rotating machines [12]. Today, it is the growing use of power electronic converters that causes the major concern about harmonic distortion in the grid [13]. Depending on the switching devices used, converters can be divided into two groups: grid-commutated and self-commutated. Grid-commutated converters, normally

using thyristors, are controlled based on the current flowing through the device [7]. Their switching characteristics cause the generation of low-order steady-state harmonics [7]. Self-commutated converters, on the other hand, can be controlled independently of the grid both in turn on- and turn off mode and are characterized by their high switching frequency. This property allows for a better filtering of low-order harmonics, and the converter itself should only generate higher order harmonics where the first order lies around the switching frequency of the component [7]. The most common transistor for wind energy converters is the insulated gate bipolar transistor (IGBT) as it can operate in the range of switching frequencies between 1 and 20 kHz [3, 7].

In addition to the steady-state harmonics generated, power electronic devices can also produce varying harmonic distortion which depends on control, loading, and characteristics of the system [12].

2.1.1 Definition of Harmonics

All continuous waveforms which are repetitive with a constant time period, T, can be expressed as an infinite sum of sines and cosines [14]. The expansion of the waveform, commonly known as Fourier series, can be expressed mathematically as

$$x(t) = X_0 + \sum_{h=1}^{\infty} x_h(t) = a_0 + \sum_{h=1}^{\infty} [a_h \cdot cos(h\omega t) + b_h \cdot sin(h\omega t)] \tag{2.1}$$

with X_0 representing the average value and where

$$a_0 = \frac{1}{2\pi} \int_{-\pi}^{\pi} x(t) d(\omega t) \tag{2.2}$$

$$a_h = \frac{1}{\pi} \int_{-\pi}^{\pi} x(t) \cdot cos(h\omega t) d(\omega t) \tag{2.3}$$

$$b_h = \frac{1}{\pi} \int_{-\pi}^{\pi} x(t) \cdot sin(h\omega t) d(\omega t) \tag{2.4}$$

h is an integer representing the h_{th} harmonic order with a frequency h times the fundamental frequency, $f_1 = \omega/2\pi$ [13].

2.1.2 Waveform Characteristics

By definition, a function has even symmetry if $x(t) = x(-t)$, odd symmetry if $x(t) = -x(-t)$, and half-wave symmetry if $x(t) = -x(t + T/2)$ [13]. The symmetry characteristics of $x(t)$

influence the properties of the Fourier series parameters as both sines and cosines happen to have half-wave symmetry. Table 2.1 provides an overview of the simplifications of the harmonic coefficients resulting from the waveform symmetry. It can be noted that the mathematical properties of half-wave symmetry results in sinusoidal waveform only containing odd harmonics.

Table 2.1: Simplifications due to waveform symmetry

Symmetry	**h**	**Coefficient**
Even $x(t) = x(-t)$	Even/odd	$a_h = \frac{2}{\pi}\int_0^\pi x(t)cos(h\omega t)d(\omega t)$ $b_h = 0$
Odd $x(t) = -x(-t)$	Even/odd	$a_h = 0$ $b_h = \frac{2}{\pi}\int_0^\pi x(t)sin(h\omega t)d(\omega t)$
Half-wave $x(t) = -x(t + T/2)$	Even	$a_h = 0$ $b_h = 0$
	Odd	$a_h = \frac{2}{\pi}\int_0^\pi x(t)cos(h\omega t)d(\omega t)$ $b_h = \frac{2}{\pi}\int_0^\pi x(t)sin(h\omega t)d(\omega t)$

Fig. 2.1 illustrates how a distorted waveform can be decomposed into a series of sinusoidal signals with different frequencies. In addition to the fundamental frequency component that would have provided a perfect sinusoidal signal, the waveform depicted in Figure 2.1a consists of another three sinusoidal signals with frequencies that are 5, 7, and 11 multiples of f_1. The distorted waveform is obtained when the four pure sinusoidal waveforms shown in Fig. 2.1b with different frequencies and phase shifts are added together.

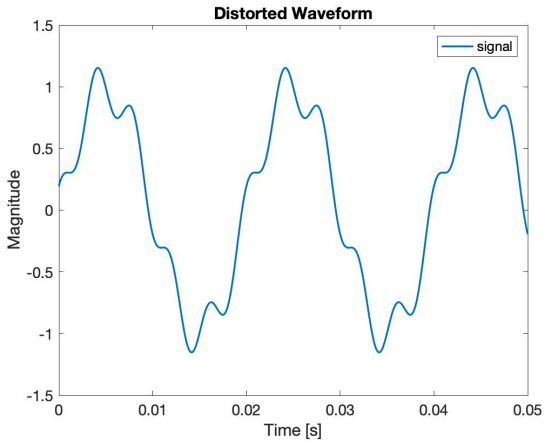

(a) Distorted periodic waveform

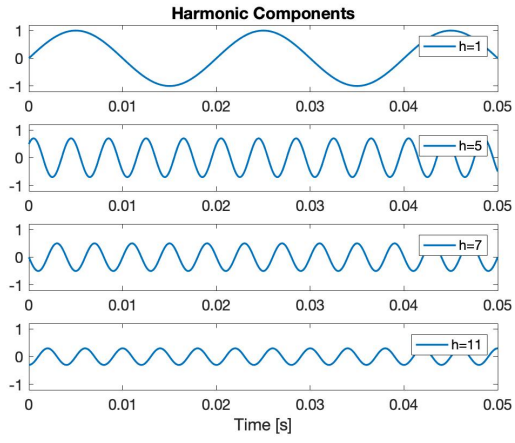

(b) Harmonic components of distorted waveform

Figure 2.1: Illustration of Fourier series expansion

2.1.3 Measurement of Harmonic Distortion

The amount of distortion in a sinusoidal waveform is commonly measured by an index called *total harmonic distortion* (THD) [12, 15]. By expressing the distorted part of a waveform as

$$x_{dis}(t) = x(t) - x_1(t) \tag{2.5}$$

where $x_1(t)$ is the fundamental frequency component and $x_{dis}(t)$ is the sum of all the harmonic frequency components $x_h(t)$, the THD of the signal is defined as

$$\%THD = 100 \cdot \sqrt{\sum_{h \neq 1} \left(\frac{x_h}{x_1}\right)^2} \tag{2.6}$$

Eq. 2.5 shows that THD expresses the root mean square of the harmonic content as a percent of the fundamental. Another index used in harmonic standards is the total demand distortion (TDD) where the only difference compared to THD is that the harmonic content is expressed as a percentage of the maximum demand current $x_{max}(t)$ instead of $x_1(t)$ [12].

2.2 Resonance

Unlike resistors, the impedance of inductive and capacitive components is frequency dependent. As a result, the system impedance differs depending on the frequency of the signal injected. Inductors are directly proportional to the frequency while capacitors are inversely proportional. Consequently, in a circuit containing both inductive and capacitive components there will exist a certain frequency where the reactance of the two components cancels out. The phenomenon is called resonance. Depending on the circuit configuration and where the system is being regarded from, the effect of resonance to the system will alter. Therefore, it is common practice to distinguish between series and parallel resonance [13]. The different characteristics will be explained by the simple circuit configurations in Fig. 2.2.

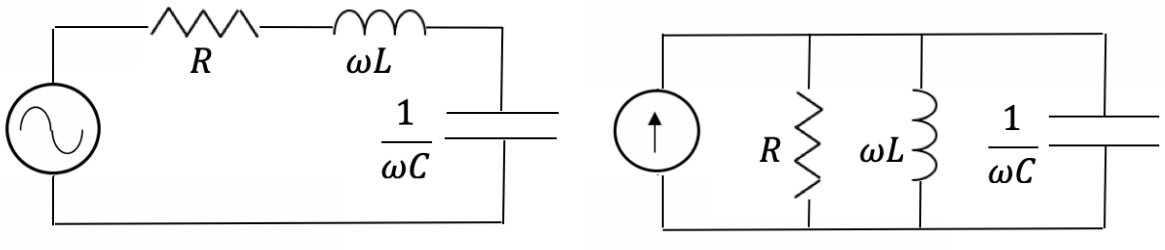

(a) Series connected circuit

(b) Parallel connected circuit

Figure 2.2: Basic circuits for resonance analysis

2.2.1 Series Resonance

Fig. 2.2a shows a series connection of a resistor, inductor, and capacitor connected to a voltage source. The circuit reactance can be expressed as

$$X_{series} = \frac{\omega^2 LC - 1}{\omega C} \tag{2.7}$$

where $\omega = 2\pi f$. It can be seen from Eq. 2.7 that the circuit will experience its lowest impedance when

$$f = \frac{1}{2\pi\sqrt{LC}} \tag{2.8}$$

as the numerator of Eq. 2.7 at this frequency, referred to as the resonance frequency f_r, becomes zero. At f_r, the energy exchange between the inductor and capacitor will resonate between the two components, resulting in an equivalent impedance only containing a resistive part. If first neglecting the resistor, a series connected circuit with zero impedance is equivalent to a short-circuited system and the current will as a result from Ohm's law go towards infinity. The behaviour is independent of the size of the voltage source and can consequently be observed even from small-signal voltage sources. The presence of a resistor provides damping of the current flowing through the circuit. If the resistance is too low, the current becomes critically high. This causes an amplification of the harmonic level, can shorten the useful lifetime of equipment, and lead to malfunctioning of the system and its components [13].

2.2.2 Parallel Resonance

The other circuit presented in Fig. 2.2 presents a parallel connection of the same passive components introduced above. Basic circuit analysis provides the following expression for the reactance of the parallel circuit

$$X_{parallel} = \frac{\omega L}{(\omega^2 LC - 1)} \tag{2.9}$$

Dual to the series connected circuit, Eq. 2.9 shows that the total impedance will experience a critical point when the frequency satisfies the condition described in Eq. 2.8. However, in this case the reactance will go towards infinity at the point of resonance since the denominator becomes zero. An infinitely high impedance connected in parallel to a current source will in theory supply an infinite voltage over the output. Thus, the resistor will also in this case contribute with damping at the point of resonance. The consequences of parallel resonance are similar to the issues resulting from series resonance. Though, in this case it is mainly the

components connected in shunt that will be exposed to the tremendous voltage level. The series connected elements are primarily vulnerable to amplified current signals from series resonance.

2.2.3 System Response to Different Frequencies

The variation in impedance as a function of frequency can be observed in the Bode plots presented in Fig. 2.3 and 2.4. The graphs show the response for the series and parallel connected circuits with two different parameter combinations of the reactive components. The capacitance is set to 10 μF in both cases, while the inductance is 40.5 mH in the first and 8.4 mH in the second. The two different ratios between inductance and capacitance leads to resonance points at system frequencies of 250 Hz and 550 Hz, respectively. To illustrate the damping effect from the resistance, each combination is plotted with two different values of the resistor. In the case of a series configuration, zero resistance will result in the most critical state for the system. For the parallel circuit, an infinite value of the resistor, will cause the worst case scenario as this can be interpreted as no parallel branch with resistance at all. This can clearly be observed in the magnitude plots of Fig. 2.3 and 2.4 as the impedance spikes are clearly reduced when damping is provided. The phase plots presents whether the inductive or the capacitive components is dominating the system.

The different graphs in Fig. 2.3 and 2.4 illustrate how the points of resonance vary depending on the system parameters. In a grid, different resonance points will be present depending on where the system is regarded from simply because the equivalent impedance will alter. In addition, the impedance seen from one point can vary due to change in loads, faults, and tripping of lines. When a distorted current or voltage signal sees a resonance point which matches one of its frequency components, an amplification of the distorted signal occurs.

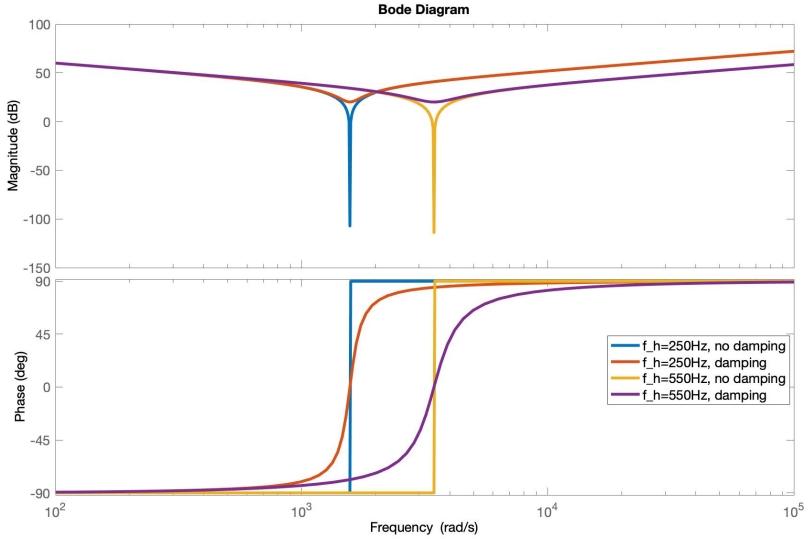

Figure 2.3: System response from series connection

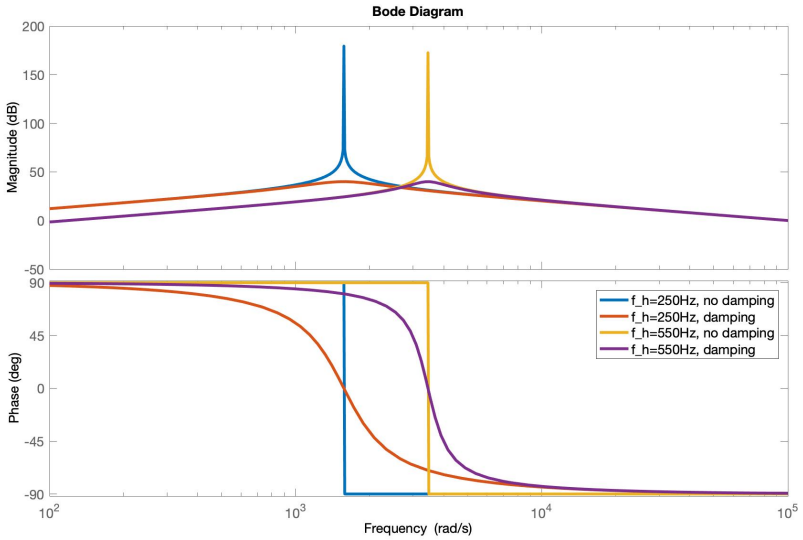

Figure 2.4: System response from parallel connection

2.2.4 Components Causing Resonance

The combination of long cable arrays and large transformers causes resonance points in the lower frequency range in HVAC connected offshore wind farms [5, 6]. The lower frequency range is in this thesis defined as frequencies up to 1000 Hz and is the frequency region of interest in this context. Thus, a brief description of the characteristics of cables and transformers is needed to understand how the components should be modelled.

2.2.4.1 Cables

The capacitance of a conductor is mainly influenced by the surrounding dielectric medium, conductor size and length, as well as the spacing between adjacent conductors and ground [16]. Compared to overhead transmission lines of the same length, the capacitance in cables is normally much higher. The main reasons are that the cable conductors in the three phases are located closer to each other and that there is a higher permittivity in the ground than in the air [16]. In reality, the capacitance is equally distributed over the whole cable length, but it is common practice to model the conductor as a π-equivalent circuit with lumped parameters. Research has shown that the π-representation is only valid for short lengths and low frequencies as the voltages and currents are affected by standing wave effects [17]. As a general guideline, the lumped representation can be applied for lengths up to $240/h$. For lengths above this, the use of distributed parameters is recommended [17]. For the sake of simplicity, frequency-dependent characteristics for cable modelling are left outside the scope of this thesis. The assumption is in compliance with C4.49's suggested modelling simplifications.

2.2.4.2 Transformers

Transformers are one of the most common elements in the power system. Capacitance from transformers do not have any effect on low-order harmonics and the losses in the magnetic core can be neglected under the assumption that the transformer is operating in its linear region [17]. Hence, the transformer can be represented as a series inductance connected between the two transformer terminals.

2.3 Filtering Techniques

External compensation of harmonics can be achieved by means of filters. The different filters can be classified as either passive or active filters, depending on their characteristics. Passive filters are achieved from various designs of passive components while active filters provide compensation with power electronic devices [13].

2.3.1 Passive Filters

Despite that resonance is caused due to the relationship between reactive components and frequency, the same characteristic can be exploited to mitigate the harmonic distortion by adding series or shunt configurations of inductors and capacitors to the system. Accordingly, the filters can be defined as low-pass, high-pass, bandpass, and bandreject filters depending on the desired characteristics [18]. A passive filter connected in series is implemented to generate a very large impedance for the frequency of interest and consequently block that frequency component from entering the system [13]. Shunt passive filters provides a path with an impedance so low for the designated current harmonic that the targeted current component will experience the branch as short-circuited. As a result, the harmonic will flow through the filter and consequently not distort the rest of the system [13]. If for example both 5^{th}, 7^{th}, and 11^{th} current harmonics are expected, a shunt passive filter consisting of three parallel branches designed to filter out one of the harmonic components each, can be installed. Fig. 2.5 illustrates a single line diagram of such a LC-filter configuration together with a high-pass filter to mitigate high-order harmonics. The magnitude of the equivalent impedance as a function of the frequency is presented in Fig. 2.6.

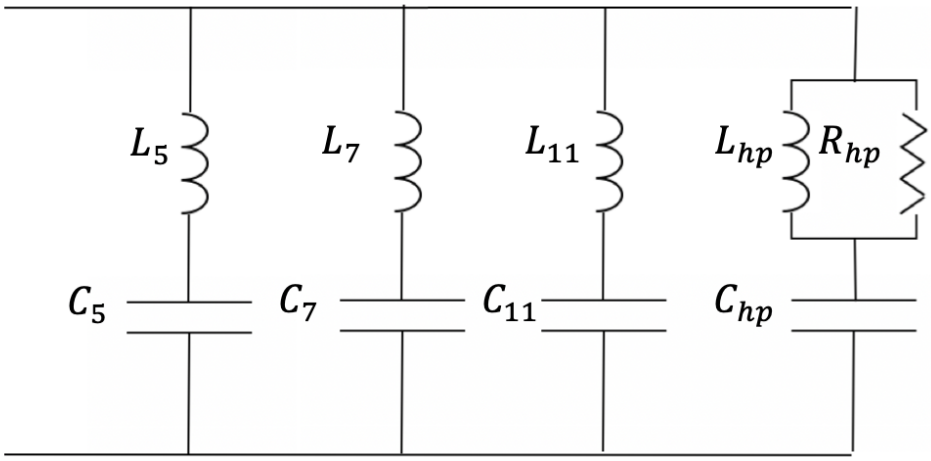

Figure 2.5: Several LC filters in parallel

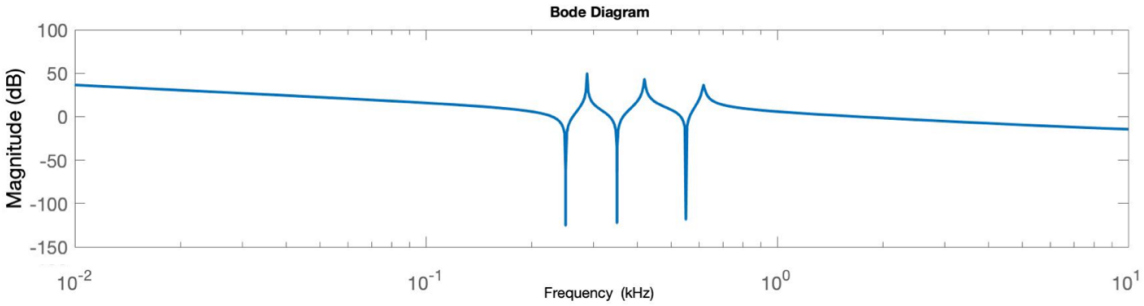

Figure 2.6: Shunt impedance of LC-filter configuration from Fig. 2.5 as a function of frequency

A physical filter is not capable of acting only on the tuned frequency component without causing any filtering of signals in the surrounding frequency region. The portion let through the filter decays exponentially. Chapter 2.2.3 showed how the presence of resistors provide damping to the system at the point of resonance. Hence, resistors can be added to the LC-filters. The sharpness of tuning for a low-pass filter can be expressed by the quality factor of the filter, Q, in Eq. 2.10 as the ratio of the inductance (or capacitance) to resistance at the tuned frequency [13, 19].

$$Q = \frac{X_{tuned}}{R} \tag{2.10}$$

The quality factor of a high-pass filter is found by taking the reciprocal of Eq. 2.10.

2.3.1.1 Challenges and Drawbacks with Passive Filters

Passive filters are widely applied in the interface between power electronic devices and the grid [20]. However, such filters have several drawbacks. Since the filters are made of passive

components, their implementation will change the equivalent impedance seen from other nodes. Consequently, there is a risk for introducing new critical resonances. The estimation of all possible resonances is a strenuous task as asymmetrical connections generates various combinations and outcomes. Further, it requires data for the surrounding grid and precise knowledge of the impedances might be challenging. In addition, the equivalent impedance can vary due to various load conditions, fault, aging effects etc. The resonance impedances are therefore not necessarily static. Another issue is that the size of the current flowing through the filter can be higher than first assumed when providing an unexpected compensation for nearby loads. Choosing the optimal rating of components can therefore be demanding. Because each filter typically handles only one harmonic component, filtering out several harmonic orders can require much space and be costly, especially if available area is limited, as it can be i.e. for offshore applications.

2.3.2 Active Filters

Passive filters appear to be efficient to prevent harmonic currents at specific frequencies from entering the system [13]. However, there are serious weaknesses with solely using passive filters for harmonic mitigation as discussed above. This has lead to the development of harmonic compensation from power electronic devices, commonly referred to as active filters [13].

Compared to passive filter solutions which only consists of capacitors, inductors, and resistors, active filters are based on active components such as power electronic applications that transfer energy from their power supply to the load [13, 21]. Dhua *et al.* [21] define active filters as any control functionality that improves the level of harmonic distortion at the point of interest. This may include additional capability of noise rejection, reduction of harmonic pollution from non-linear loads and controlled injection of harmonic currents. Active filters are beneficial due to their dynamic characteristics as they can follow changes in the resonance frequency. In addition, no extra space is required when it is implemented as an additional control application in already constructed converters.

In general, it is common to distinguish between series and shunt connected active filters depending on the connection to the network [11, 13]. The series active filter prevents the harmonics from flowing into the system while the shunt active filter reduces the harmonic content.

2.3.2.1 Series Active Filter

The objective of a series connected active filter is to block the harmonic components from entering the rest of the system. As seen from Fig. 2.7, a non-linear load with a load current consisting of a fundamental component, i_{L1}, and the sum of distorted components, i_{dis}, is connected to the grid through a series active filter. The filter itself is connected in series with the system through a transformer and is represented by a voltage source converter (VSC) with a filter inductor on the AC side and a DC-capacitor on the rectified side. The implementation

of the active filter can be regarded as a controlled voltage source, v_{AF}, which provides very high impedances to signals at frequencies other than the one of the fundamental component [13]. The isolated harmonic components require a path to flow and the series active filter should therefore be combined with some kind of passive filtering [13]. An advantage of this type of active filtering is that the harmonic voltage can be directly influenced since the filter is behaving as a voltage source. However, the filter is difficult to retrofit and more expensive than the shunt type as it requires an additional transformer [11].

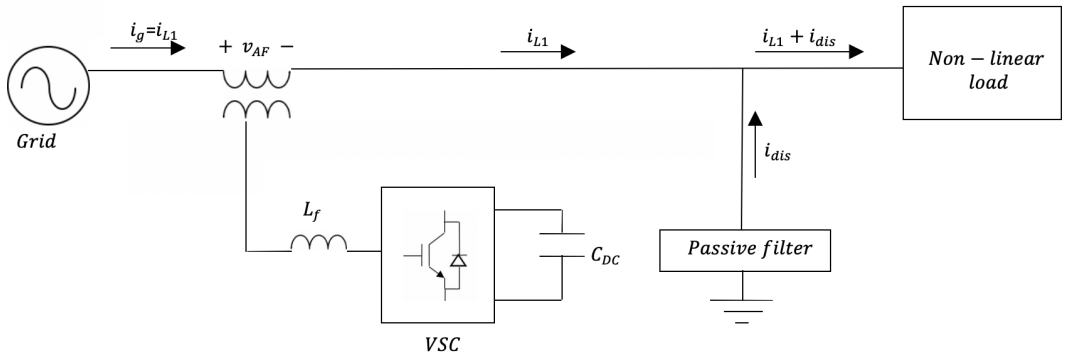

Figure 2.7: Scheme of series active filter

2.3.2.2 Shunt Active Filter

The objective of a shunt active filter is to eliminate the current harmonic components seen from the grid by injecting a current signal equal, but 180° phase-shifted, to the harmonic components detected at the point of connection. The principle of operation is depicted in Fig. 2.8 containing the same nomenclature as used in Fig. 2.7. Despite that the shunt connected filter is not capable of attenuate voltage harmonics directly, an advantage over the series connected is that it can be tuned both during commissioning and operation. In addition to its lower costs, the shunt type is the most used solution out of the two today [11].

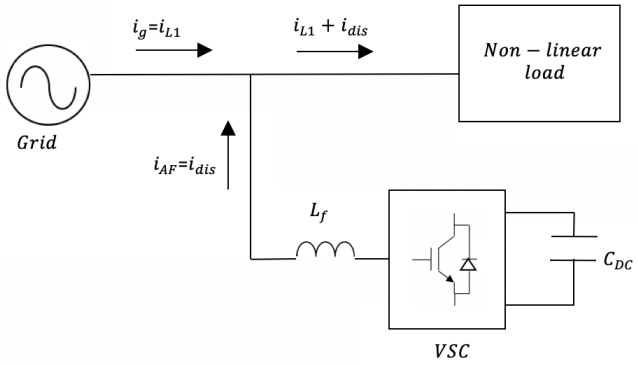

Figure 2.8: Scheme of shunt active filter

2.4 Harmonic Standards

To ensure that the harmonic levels are kept within reasonable limits, harmonic standards are developed. An overview of the revised IEEE 519-1992 standard from 2014 is presented below. The standard sets the acceptable limit to be met at the point of common coupling (PCC) under steady-state conditions. This master thesis is concerning the harmonic levels within an offshore wind farm. Hence, deciding PCC becomes a matter of definition as it potentially is not present in the system to be regarded at all. However, the standards are provided to establish a reference to acceptable levels of harmonic distortion in the grid for the reader.

2.4.1 Standards for Voltage Harmonics at PCC

IEEE's recommended practice and requirement for harmonic control suggests that the voltage distortion should be kept below the limits presented in Table 2.2. The acceptable limit of harmonic distortion decreases the higher the voltage level is.

Table 2.2: Limits for voltage distortion at PCC [12]

Bus Voltage at PCC [V]	**Individual harmonic** [%]	**THD** [%]
V $\leq$ 1.0 kV	5.0	8.0
1 kV $\leq$ V $\leq$69 kV	3.0	5.0
69 kV $\leq$ V $\leq$ 161 kV	1.5	2.5
161 kV $\leq$ V	1.0	1.5

2.4.2 Standards for Current Harmonics at PCC

With regard to current harmonics, IEEE's recommended practice and requirement for harmonic control suggests that the current distortion from odd harmonics should be kept below the limits presented in Table 2.3, 2.4, and 2.5. I_{sc} describes the maximum short-circuit current at PCC, while I_L expresses the maximum demand load current at PCC under normal conditions. The column to the very left in the subsequent tables becomes therefore a measurement of the ratio between the grid strength and loading. The harmonic distortion from even harmonics is limited to 25% of the limits for odd harmonics.

Table 2.3: Limits for current distortion from odd harmonics in percent of I_L at PCC for systems rated 120 V through 69 kV [12]

I_{SC}/I_L	**3$\leq$ h $<$ 11**	**11$\leq$ h $<$ 17**	**17$\leq$ h $<$ 23**	**23$\leq$ h $\leq$ 35**	**35$\leq$ h $\leq$ 50**	**TDD**
$<$ 20	4.0	2.0	1.5	0.6	0.3	5.0
20$<$50	3.5	1.75	1.25	0.5	0.25	4.0
50$<$100	5.0	2.25	2.0	0.75	0.35	6.0

Table 2.4: Limits for current distortion from odd harmonics in percent of I_L at PCC for systems rated above 69 kV through 161 kV [12]

I_{SC}/I_L	**3≤ h < 11**	**11≤ h < 17**	**17≤ h < 23**	**23≤ h ≤ 35**	**35≤ h ≤ 50**	**TDD**
< 20	2.0	1.0	0.75	0.3	0.15	2.5
20<50	3.5	1.75	1.25	0.5	0.25	4.0
50<100	5.0	2.25	2.0	0.75	0.35	6.0
100<1000	6.0	2.75	2.5	1.0	0.5	7.5
> 1000	7.5	3.5	3.0	1.25	0.7	10.0

Table 2.5: Limits for current distortion from odd harmonics in percent of I_L at PCC for systems rated above 161 kV [12]

I_{SC}/I_L	**3≤ h < 11**	**11≤ h < 17**	**17≤ h < 23**	**23≤ h ≤ 35**	**35≤ h ≤ 50**	**TDD**
< 25	1.0	0.5	0.38	0.15	0.1	1.5
25<50	2.0	1.0	0.75	0.3	0.15	2.5
≥ 50	3.0	1.5	1.15	0.45	0.22	3.75

The standards for current harmonics show how the stringency increases with the voltage levels and harmonic order, but decreases with an increasing grid strength ratio.

Chapter 3

Topology of Benchmark Systems

3.1 Objective for CIGRE's Working Group C4.49 *Multi-frequency stability of converter-based modern power systems*

The introduction of long HVAC cables, HVAC/HVDC connections and widespread distributed renewable energy sources increases the complexity of the electrical infrastructure [5, 9]. In particular, this have turned out to be a challenge for HVAC connected offshore wind farms. The combination of long AC cable connections and large transformers can introduce poorly damped resonances in the lower frequency range which can interact with the converter control and cause high harmonics in the grid [9]. Those harmonics, which are different from steady-state harmonics from non-linear loads, do not have a common standard [9]. Thus, C4.49 was established to describe the phenomenon and provide a common understanding on modelling, analysis, evaluation, and mitigation techniques. During the time of this thesis, the group has evolved the design of two benchmark systems that will be used as a common starting point. The systems should be as simple as possible, but at the same time manage to represent the main criticalities that can arise in a power-electronic dominated system in terms of multi-frequency harmonic instabilities.

This chapter will present the benchmark systems as well as adjustments, simplifications, and assumptions that have been made. Suggestions from the literature on how to estimate the passive components related to the converter will be introduced. A comment on system parameters and base values is given in the end of the chapter.

3.2 Benchmark System 1

The rapid increase in penetration of wind power to the grid has forced a stricter development of grid code requirements for the wind power industry. This has lead to a development of the wind turbine designs [3]. Even though a comparison of different kinds of wind turbine technology is

beyond the scope of this thesis, it should be mentioned that the so-called *Type* 4 wind turbine is among the best selling wind turbines on the market today [3]. The *Type* 4 wind turbine is connected to the grid through an integrated back-to-back (BTB) two-level voltage source converter (2L-VSC) which allows full decoupling of the wind turbine from the grid. Hence, the turbine can operate at full speed range in addition to its capability of providing reactive power compensation [3]. Fig. 3.1 depicts the general structure of a *Type* 4 wind turbine with blades, gearbox, generator, back-to-back converter, and transformer [22].

The area of interest for C4.49 as well as for this master thesis is the interaction between the generating unit's grid side converter controller and physical elements the grid. It should be stressed that C4.49 does not only limit their research to offshore wind farms as i.e. large photovoltaic power plants can introduce the same issues. However, it has been a choice of this thesis only to look at the benchmark systems in the context of offshore wind farms. By excluding the components before the DC-link capacitor in Fig. 3.1 from the model, as they are not of interest for the analysis, the wind turbine model corresponds to benchmark system 1 defined by C4.49. A more detailed representation is presented in Fig. 3.2.

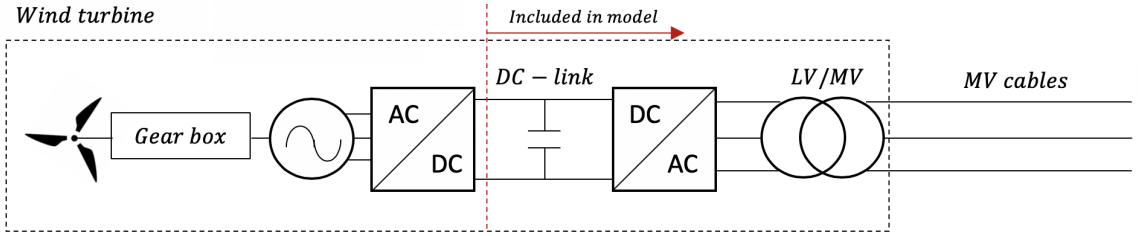

Figure 3.1: Major components in a wind turbine

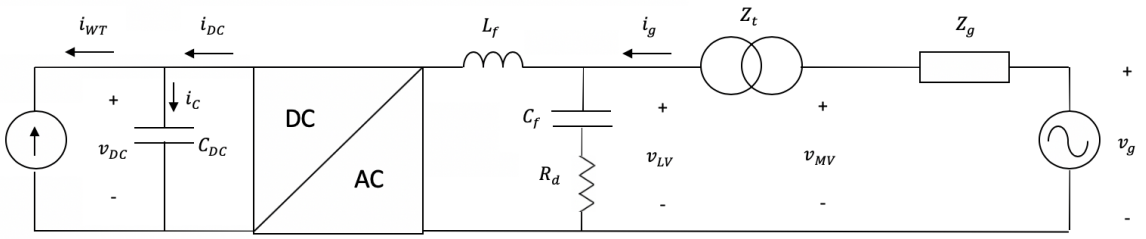

Figure 3.2: Benchmark system 1

Benchmark system 1 shows a current source injecting current to the grid through a 2L-VSC represented as a DC/AC block. The DC side is maintained stable with a sufficiently large DC-link capacitor, C_{DC}, and properly tuned DC voltage control. On the AC side, a series inductor and a shunt capacitor with the values of L_f and C_f are connected for filtering purposes. Damping is provided by the resistor R_d in series with the filter capacitor. Together with the mainly inductive LV/MV transformer impedance, Z_t, L_f and C_f provides a LCL-filter. An equivalent grid impedance, Z_g, is present between the MV-side of the transformer and the AC

voltage source. Since no further specification is given from C4.49 for this component, Z_g will be disregarded in the later analysis.

3.2.1 Two-Level Voltage Source Converter

The most complex component in the system representation of the wind turbine is the 2L-VSC. The topology of such a converter is shown in Fig. 3.3. The circuit diagram shows how the DC side is connected to the AC side through three legs, one for each phase, each consisting of two switching devices, here referred to as IGBTs. As mentioned in Chapter 2, IGBT is the most common switching device in self-commutated converters for wind applications today due to its control capability and high switching frequency [7]. It is well known from basic circuit analysis that the two IGBTs in each leg cannot conduct simultaneously as this would short-circuit the system. The state of the switches are controlled by injecting a control signal, δ_i where $i = a, b, c$, consisting of binary values. If $\delta_i = 1$, S_i is conducting and S_i' open. On the contrary, if $\delta_i = 0$, S_i open and S_i' is conducting. As a result, the operation of the 2L-VSC provides a discrete characteristic to the system.

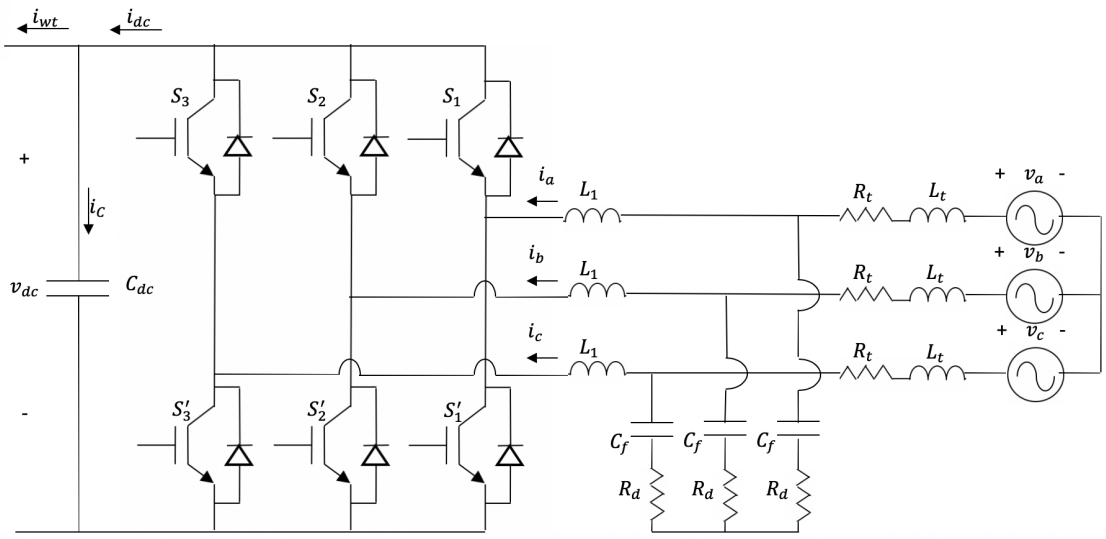

Figure 3.3: Topology for a 2L-VSC

3.2.1.1 LCL-filter: The Grid Interface of the Converter

In context of the wind power systems, the wind turbine inverter is normally connected to the grid through a passive filter to improve the performance of the grid current [23]. For this purpose, LCL-filters have turned out to be efficient as they can provide much better attenuation of harmonics and ripples over a higher frequency range by using smaller passive components than basic L-filters [24, 25]. However, the capacitance does theoretically introduce resonance points

which can cause amplification of harmonics and lead to closed-loop instability [24]. Therefore, the application requires methods for damping.

3.2.1.2 Estimating Size of DC-link Capacitance

The DC-link capacitor must be large enough to compensate for voltage variations as well as keeping the DC voltage ripples originated from the IGBTs within acceptable limits [26, 27]. For this master thesis the acceptable magnitude of ripples is decided to be 5% of the base value of the DC voltage. Authors use different approaches to estimate C_{DC}. Since the AC side of the converter comprises a three phase system, Eq. 3.1 is proposed for calculating C_{DC} [27]. The estimation of the required capacitance is based on the magnitude of the phase currents, I_b, the switching frequency, f_{sw}, and the maximum allowed voltage ripple, Δv_{pp}^{max}.

$$C_{DC} \geq \frac{1}{4f_{sw}} \frac{I_b}{\Delta v_{pp}^{max}} \tag{3.1}$$

3.2.1.3 Estimating Size of Filter Inductance

A common practice is to design the LCL-filter so that the current ripple is limited to 2% of the output peak-to-peak current. As a result, L_f is typically designed to keep the ripple below 10% of the rated current [25, 28]. H. Brantsæter *et al.* [28] provides the following expression for estimating the filter inductor size

$$L_f = \frac{1}{8} \cdot \frac{V_{dc}}{0.1\sqrt{3} I_b f_{sw}} \tag{3.2}$$

while A. Reznik *et al.* [25] have replaced the factor of 1/8 with 1/6. As the filter inductor value to be used in the simulations of this master thesis is provided by C4.49, Eq. 3.2 will only be needed to analyze the impact of changing the system ratings. Thus, a further investigation of the difference of the scaling factors in the two references is left out.

Compared to basic L-filters, the presence of an additional capacitor introduces a resonance frequency, expressed by Eq. 3.3.

$$f_r = \frac{1}{2\pi} \sqrt{\frac{L_f + L_t}{L_f L_t C_f}} \tag{3.3}$$

To avoid interactions with low-order harmonics and switching frequency harmonics, the following constraint should be fulfilled

$$10 \cdot f_{nom} \leq f_r \leq 0.5 \cdot f_{sw} \tag{3.4}$$

The relationship between the grid side - and converter side inductor can be expressed as

$$L_t = r \cdot L_f \tag{3.5}$$

where r is ratio between the two inductors.

3.2.1.4 Estimating Size of Filter Capacitance

The size of the filter capacitor is typically chosen so that it can provide a reactive power equal 5% of the rated power of the converter [25, 28].

3.2.1.5 Estimating Size of Passive Damping Component

The system requires damping to mitigate resonances around the resonance frequency introduced by C_f. This can either be solved by passive or active damping. Passive damping can be applied by a resistor in series with the filter capacitor while active damping can be provided as an additional application in the control system of the converter [29]. Despite its introduction of additional losses, passive damping will be used in this thesis because of its simple implementation. Sizing of the damping resistor can be done with Eq. 3.6 [25, 28].

$$R_d = \frac{1}{3 \cdot 2\pi f_r \cdot C_f} \tag{3.6}$$

3.3 Benchmark System 2

A strength of C4.49 is its unique combination of experience from research and real life applications as the members are coming from both academia and the industry. The good knowledge to ongoing projects gives access to actual sizes and dimensions which makes the modelling as reasonable as possible. Despite that the models should be simple, it has been important for C4.49 to make realistic benchmark systems. The combination of a system presenting the issues to be investigated with sensible parameters is a time consuming task. However, as it was decided for this thesis to treat the generating units as wind turbines, it was eventually chosen to let the second benchmark system represent one of the clusters in the Hornsea Project ONE wind power plant. The wind farm is an offshore wind integration project with HVAC connection located approximately 100 km from the east coast of Great Britain [6]. The whole wind farm consists of 174 wind turbines, each with a rated power of 7 MW. The wind farm is grouped in three

clusters, each containing 58 wind turbines. Thus, benchmark system 2 is designed with a total capacity of 406 MW.

The second benchmark system used for this master thesis is shown in Fig. 3.4. The wind turbines are represented by two generating units, from now referred to as A and B, equal to the one defined as benchmark system 1. In order to represent the cluster of 58 wind turbines, A and B are serving as 30 and 28 wind turbines, respectively. This can be done by scaling up the representation of a single wind turbine and will be discussed later. A and B are connected to two MV/HV transformers via MV cable arrays before they are connected together on the HV side of those transformers. The wind farm is connected with the grid though a long HVAC cable and two HV/EHV transformers.

Benchmark system 2 as presented in Fig. 3.4 is a little changed from the system suggested by C4.49. The AC voltage source was initially a grid forming converter interconnecting to a hypothetical HVDC transmission. In addition, the shunt reactor is here located on the converter side of the HVAC cable.

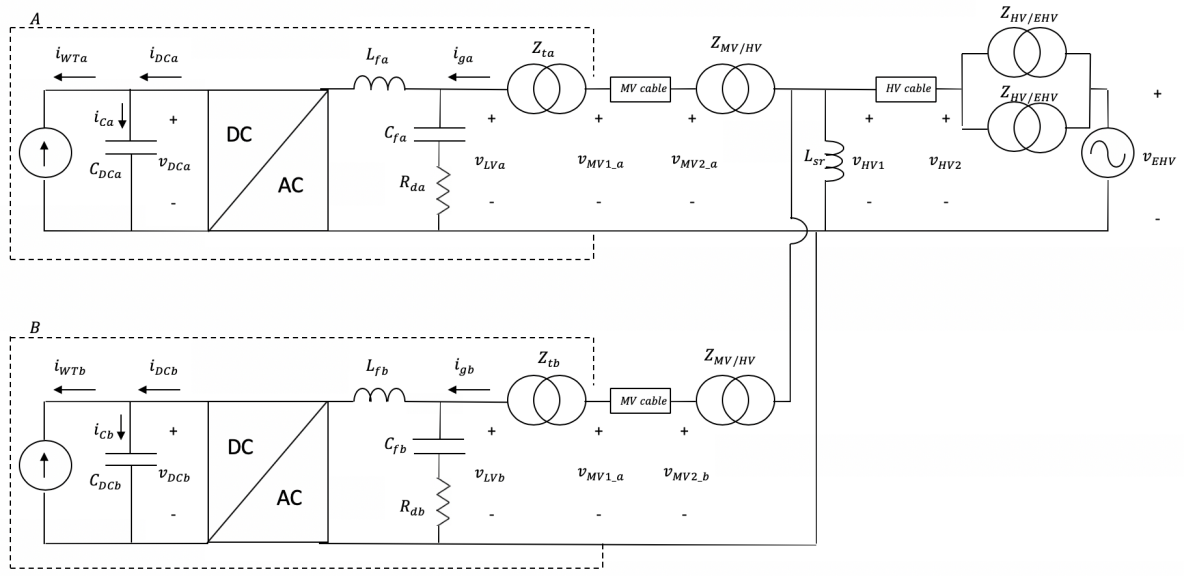

Figure 3.4: Benchmark system 2

In order to better illustrate what A and B are representing, Fig. 3.5 illustrates the system with all the 58 wind turbines included. 6 radials with 5 wind turbines on each are connected to one bus on the MV-side of the park transformer and are represented by A in the benchmark system. The remaining 28 wind turbines represented by B are equally distributed over 7 radials. The distribution of the wind turbines are chosen by the author. The decision is made based on the fact that the cluster in the Hornsea Project ONE consists of 12 strings [6] as well as a desire for obtaining symmetry within A and B.

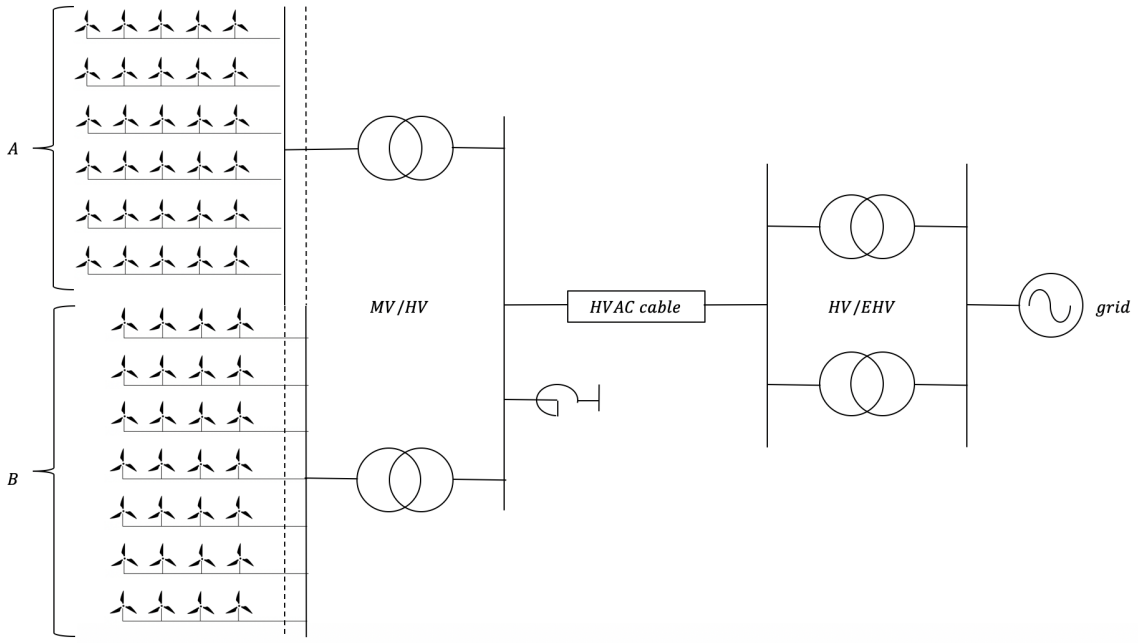

Figure 3.5: Illustration of benchmark system 2 with all wind turbines included

3.3.1 Lumped Representation of MV Collection Grid

Since the wind turbines are represented with only two generating units in the benchmark system, a lumped representation of the MV collection grid is required. Fig. 3.5 shows that wind turbines are distributed over the whole radial. Therefore, the amount of current flowing through the cable depends on the location in radial. This must be taken into consideration when estimating the equivalent impedance, $Z_{MV,ab}$, of the MV arrays [30]. Using an aggregation based on voltage drop gives the following expression for calculating the equivalent impedance of radial m

$$Z_{eq_m} = \sum_{n_m=1}^{N_m} \frac{n_m}{N_m} Z_{n_m} \tag{3.7}$$

where N_m is the number of wind turbines in radial m and Z_{n_m} is the cable impedance between the n^{th} and $(n+1)^{th}$ wind turbine on radial m [30]. It is assumed that the radials within one cluster are symmetrical and that Z_{n_m} is the same between all adjacent turbines and therefore can be treated as the constant Z_{cable}. Consequently, Z_{eq_m} is the same for all the radials in one cluster. This results in $Z_{eq} = 3Z_{cable}$ in A and $Z_{eq} = 2.5Z_{cable}$ in B. The overall aggregated impedance is calculated with Eq. 3.8 as the radials are in parallel.

$$Z_{MV,ab} = \frac{1}{\sum_{m=1}^{M} \frac{1}{Z_{cable}}} \tag{3.8}$$

3.4 System Parameters and Per Unit Representation

Table 3.1 presents the values of the voltage levels in the benchmark systems. The parameters for the cables, transformers, and the wind turbine provided by C4.49 are given in Appendix A.

Table 3.1: Definition of base values for the benchmark systems

Voltage (rms, ph-ph)	**Size [kV]**
V_{EHV}	400
V_{HV}	220
V_{MV}	34
V_{LV}	1

In consideration of the need to up-scale the single wind turbine, a pu-representation was regarded as beneficial for the control design. Table 3.2 gives an overview of the defined base values for the wind turbine representations. It should be noted that the base value for the AC voltages and currents are defined as the magnitude of phase-to-ground. Hence, it differs from the more commonly applied definition of voltage base values as the rms value of line-to-line voltage, which is the base definition used for the transformer data in Appendix A. Further, it should be noted for later discussion that the base values of the apparent power are based on the apparent power of the wind turbine transformer which is 9 MW, and not 7 MW which is the rated power of the wind turbines.

Table 3.2: Definition of base values for control system

Parameter	**Base Value**
f_1	50 Hz
w_b	$2\pi f_1$
V_b	$\frac{\sqrt{2}}{\sqrt{3}} V_{LV}$
V_{dcb}	2000
N_a	30
N_b	28
S_{b_a}	$N_a \cdot S_{LV/MV}$
S_{b_b}	$N_b \cdot S_{LV/MV}$
I_{b_a}	$\frac{2}{3} S_{b_a}/V_b$
I_{b_b}	$\frac{2}{3} S_{b_b}/V_b$
I_{dcb_a}	S_{b_a}/V_{dcb}
I_{dcb_b}	S_{b_b}/V_{dcb}
Z_{b_a}	V_b/I_{b_a}
Z_{b_b}	V_b/I_{b_b}
Z_{dcb_a}	V_{dcb}/I_{dcb_a}
Z_{dcb_b}	V_{dcb}/I_{dcb_b}

General expressions for estimating pu-values of passive components are provided in Table 3.3.

Table 3.3: Pu-representation of passive components

Parameter	**Pu-representation**
R_{pu}	R/Z_b
L_{pu}	$(w_b L)/Z_b$
C_{pu}	$1/(w_b C Z_b)$

Chapter 4

Control Theory For Converter Modelling

The purpose of this chapter is to present the control theory for the 2L-VSC introduced in Chapter 3. In order to achieve a well-functioning converter, it is essential to work with properly tuned control parameters. There are different techniques and ways to model the control system and tune the parameters. This chapter will introduce the methods applied and the assumptions that have been made.

4.1 Principle of Control Design

The design of the converter control is based on the principle of power balance between the DC and the AC side. Transients in the power injected from the DC current source as well as fluctuations due to the switching frequency of the converter cause transients and small variations in the DC link voltage. The error is detected and compensated for by a DC voltage control which generates a signal equal to the required current flowing to the AC side to maintain power balance. This signal becomes the reference for an inner current control loop which responds by generating a signal corresponding to the required voltage level on the AC side of the converter to allow the demanded current to flow [31, 32].

Many papers, like [32, 33], implement the converter control in the synchronous reference frame, also known as *dq*-frame. It is also desired from C4.49 as this control reference frame is quite common in the industry. A *dq*-representation of the voltage and current waveforms provides a presentation of the signals that is rotating synchronously with the grid voltage. Such a DC representation of the signals can be favourable as it allows direct and independent control of active and reactive power [32, 33]. A transformation from the *abc*-frame to the *dq*-frame can be conducted with Eq. 4.1 and 4.2 known as Clarke and Park transform, respectively. The relationship between the different phasors is presented in Fig. 4.1 [34, 35]. The *d*-axis of the

rotating reference frame is aligned with phase a of the AC grid voltage signal causing v_q to be zero [32, 36].

$$v_\alpha = \frac{1}{3}(2v_a - v_b - v_c) \tag{4.1a}$$

$$v_\beta = \frac{1}{\sqrt{3}}(v_b - v_c) \tag{4.1b}$$

$$v_0 = \frac{1}{3}(v_a + v_b + v_c) \tag{4.1c}$$

$$v_d = v_\alpha cos(\omega t) + v_\beta sin(\omega t) \tag{4.2a}$$

$$v_q = v_\beta cos(\omega t) - v_\alpha sin(\omega t) \tag{4.2b}$$

$$v_0 = v_0 \tag{4.2c}$$

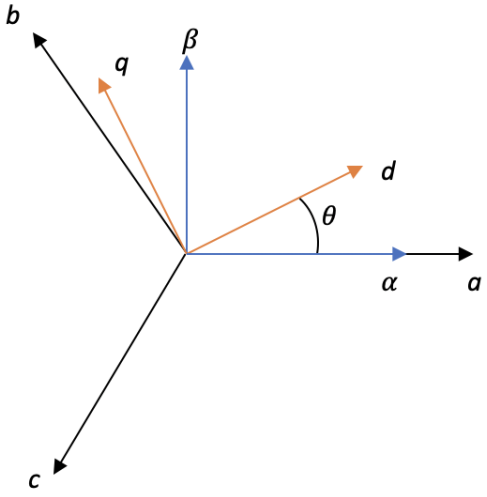

Figure 4.1: Relationship between the various phasors in the different reference frames

Due to its resilience and simple structure when regulating DC signals, the proportional-integral (PI) controller is often used for converter control in synchronous reference frame [32, 33]. As the name implies, the regulator consists of one proportional term and one integral term, each determined by the control parameters K_p and K_i. By feeding the PI-regulator with a system error, a properly tuned controller will provide a modified output corresponding to the required state of the system to remove the error. K_p is basically an amplifier with an adjustable gain. Thus, the proportional controller alone will result in a steady-state error. By including the integral control, the steady-state error can be eliminated [37]. The transfer function of a PI-controller can in the Laplace domain be written as

$$G_{pi}(s) = K_p + \frac{K_i}{s} \tag{4.3a}$$

$$= K_p \frac{(T_{pi}s + 1)}{T_{pi}s} \tag{4.3b}$$

where $T_{pi} = K_p/K_i$. The tuning of the parameters depends on the characteristics of the control loop and must be analyzed individually for each system.

4.2 Mathematical Modelling of a 2L-VSC

A proper adjustment of control parameters requires a mathematical representation of the system. The topology of the 2L-VSC seen in Fig. 3.3 shows that a LCL-filter is used as an interface between the converter and the grid. From a modelling perspective, the presence of the filter capacitance, C_f, makes the mathematical modelling much more complex compared to a simple L-filter. However, as the purpose of the filter capacitance is to mitigate the high-frequency switching ripples from the converter and the current control mainly influences the low-order harmonics, C_f can be neglected when designing the current control [8, 38]. Hence, the system equations for the 2L-VSC become

$$e_d = L\frac{\delta i_d}{\delta t} - j\omega L i_q + R i_d + \delta_d v_{DC} \tag{4.4a}$$

$$e_q = L\frac{\delta i_q}{\delta t} + j\omega L i_d + R i_q + \delta_q v_{DC} \tag{4.4b}$$

$$C\frac{\delta v_{DC}}{\delta t} = \frac{3}{2}(\delta_d i_d + \delta_q i_q) \tag{4.4c}$$

in the dq-frame when neglecting C_f and where $L = L_f + L_t$ and $R = R_t$ [8,32,38]. Eq. 4.4(a,b) show a cross-coupling between i_d and i_q. Despite that the system itself cannot be changed, feed-forward of measured signals can compensate for the coupling. In this way, the current components can be controlled independently [32, 39].

4.3 Control Applications

A schematic illustration of the control applications is presented in Fig. 4.2. The illustration shows that the DC voltage is measured and used as input for the DC voltage control together with a set reference. The DC controller generates a reference for the d-component of the inner current control. The reference for the reactive current component, $I_{q,ref}$, is typically set to zero [33]. Measured values of the AC current and AC voltage are also required as inputs for the inner control loop. Based on the inputs, the current control generates the voltage reference

signal for the converter. The signal is processed through a pulse width modulator (PWM) which is assigned the task to generate the sufficient control signals for the IGBTs in the 2L-VSC. A phase-looked loop (PLL) is necessary for the transformation between *abc* and *dq* frame.

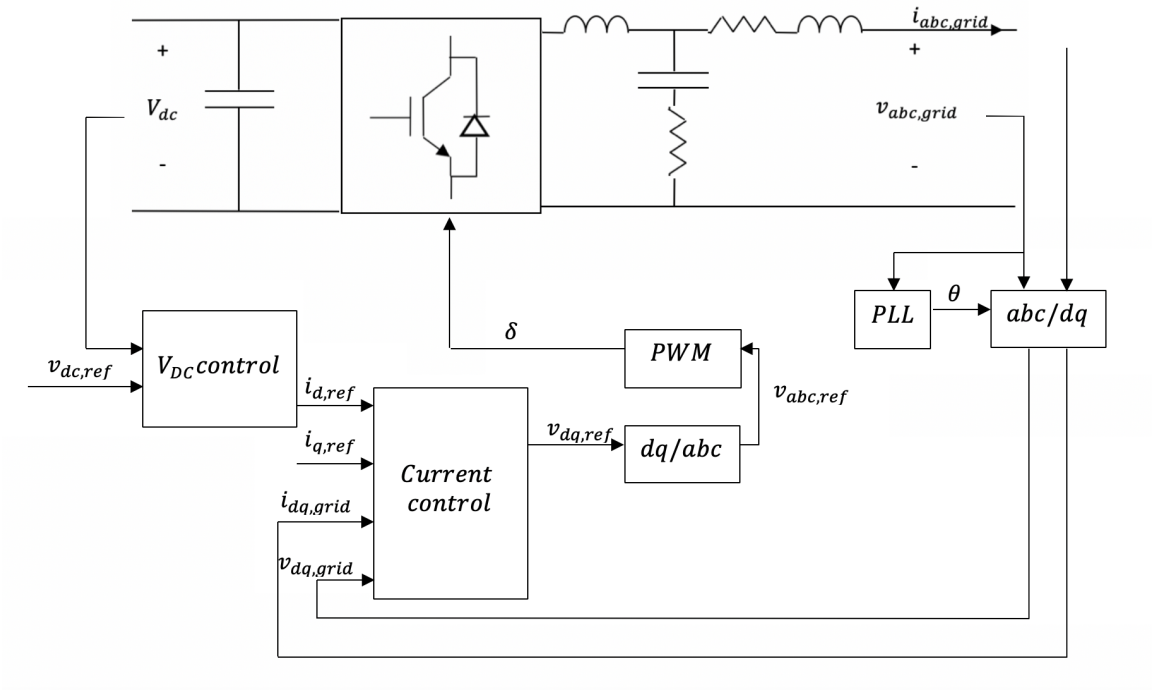

Figure 4.2: Overview of coupling between control applications and system

4.3.1 Pulse Width Modulator

A PWM generates the control signals to the converter based on a comparison between the desired output voltage waveform, v_{ref}, and a high-frequency triangular signal, v_{tri}. Depending on whether the value of v_{ref} is higher or lower than v_{tri}, binary numbers are created and sent to the respective switch. A command of 1 signalizes that the switch should conduct, while a command equal 0 tells the switch to be open. The frequency of the triangular signal decides the switching frequency, f_{sw}, of the converter and is in this case set to 2500 Hz based on the suggestions from C4.49.

As PWMs are most likely to be digitally implemented, some time delay is expected. In this master thesis, the total time delay is assumed to be 1.5 T_{sw} with $T_{sw} = 1/f_{sw}$. 0.5 T_{sw} is compensating for the sample and hold effect in the PWM, while 1 T_{sw} makes up for computation time [8, 39]. By applying a first order approximation of the delay, the transfer function for the delay time of the PWM becomes

$$G_{pwm}(s) = \frac{1}{1 + sT_e} \tag{4.5}$$

where $T_e = 1.5T_{sw}$ [8, 39].

4.3.2 Phase-Locked Loop

Based on the definition of the relationship between the different phasors presented in Fig. 4.1, the angle between phase a and the d-axis must be known to fulfill the transformation from a stationary to synchronous reference frame. The purpose with a phase-locked loop is to obtain this angle which should increase linearly from 0 to 2π with time steps corresponding to f_1. The approach is based on the fact that the d-component in the dq-frame is aligned with phase a on the real axis. The grid voltage is being used as the reference. Thus, the q-component, $v_{q,grid}$ should be zero at all times [32, 36]. A PI-controller is integrated in the PLL to regulate any deviation from the reference in the rotational speed and should be detected at the moment $v_{q,grid} \neq 0$. Fig. 4.3 illustrates the principle of operation for the PLL.

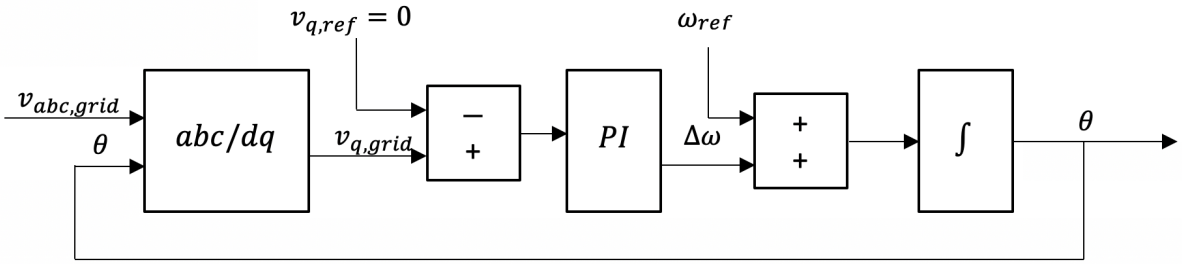

Figure 4.3: Principle of operation for a PLL

The block illustration depicts how the grid voltage in the abc-frame is used as input and converted to dq-representation with a feedback of the calculated value of θ. The deviation from the reference value of $v_{q,grid}$ is processed through the PI-controller. To compensate for the error, the required rotational speed is integrated to achieve the new phase angle of the system. Mathematically, the signal which is being integrated to obtain θ can be expressed by Eq. 4.6 [40].

$$\frac{\delta\theta}{\delta t} = \omega_{ref} + \Delta\omega = \omega_{ref} + [K_p(x_q - x_{q,ref}) + K_i \int (x_q - x_{q,ref})\delta t] \tag{4.6}$$

The value of the control parameters are chosen based on the assumption that the closed loop transfer function of the PLL can be reduced to the canonical form of a second order system as done by F. Marafão *et al.* [41]. Thus,

$$K_{p,pll} = 2\xi\omega_n \tag{4.7a}$$

$$K_{i,pll} = \omega_n^2 \tag{4.7b}$$

where ω_n is the crossover frequency and ξ is the damping factor [41]. Similar to A. Alonso [42], a cross-over frequency of 10 Hz is chosen. The damping factor is set to 1.

4.3.3 Current Control of a 2L-VSC

Fig. 4.4 presents a block diagram of the inner current control loop with the mathematical representation in Laplace domain of the PI-controller, PWM, and system.

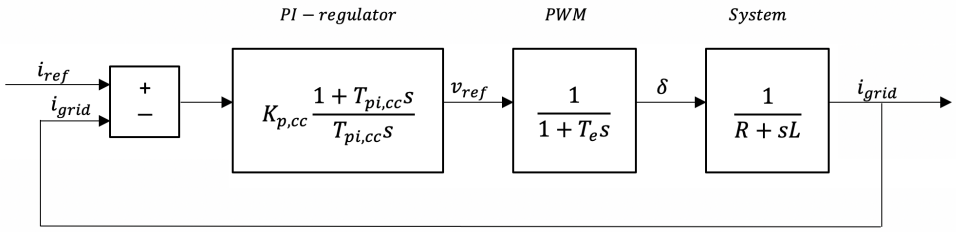

Figure 4.4: Block diagram of the inner current control

As seen from the illustration, the system for the inner current control is expressed by Eq. 4.8. This is a correct mathematical representation once the d and q-component of the current are decoupled and the filter capacitance is neglected.

$$\frac{I(s)}{V_{DC}D(s)} = \frac{1}{R+sL} \tag{4.8}$$

The open loop transfer function of the inner control loop can be written as

$$G_{cc,ol}(s) = K_{p,cc,pu}\frac{1+T_{pi,cc}s}{T_{pi,cc}s} \cdot \frac{1}{1+T_e s} \cdot \frac{1}{R_{pu}} \cdot \frac{1}{1+\tau_{pu}s} \tag{4.9}$$

in pu-representation where $\tau_{pu} = L_{pu}/(R_{pu}\omega_b)$.

4.3.3.1 Tuning of Current Control Parameters

Tuning of controllers is one of the critical stages when designing control systems. Depending on the characteristics of the control loop, different tuning methods can be applied. For control loops with only one dominant time constant, modulus optimum can be used for controller tuning [32]. The tuning technique is based on providing a zero in the PI-controller that cancels out the dominant pole of the system while keeping the closed loop gain at unity up to frequencies as high as possible [39]. At the same time it should be ensured that the crossover frequency of the open loop transfer function is kept well below the switching frequency of the converter to avoid higher-order frequency noise [32].

The closed loop transfer function of the system provided in Eq. 4.10 is proportional to the standard form of second order systems described by Eq. 4.11 [37].

$$G_{cc,cl}(s) = \frac{\omega_b K_{p,cc,pu}}{L_{pu} T_e} \cdot \frac{1}{s^2 + \frac{1}{T_e}s + \frac{\omega_b K_{p,cc,pu}}{L_{pu} T_e}} \tag{4.10}$$

$$G(s) = \frac{\omega_n^2}{s^2 + 2\xi\omega_n s + \omega_n^2} \tag{4.11}$$

As introduced when describing the PLL, ω_n represents the undamped natural frequency and ξ describes the damping ratio of the system. Applying modulus optimum to the current control provides the following general expressions for the control parameters in pu-representation [32,39]:

$$K_{p,cc,pu} = \frac{L_{pu}}{2\xi_{cc}^2 T_e \omega_b} \tag{4.12a}$$

$$T_{pi,cc} = \frac{L_{pu}}{R_{pu}\omega_b} \tag{4.12b}$$

$$K_{i,cc,pu} = \frac{K_p}{T_{pi,cc}} \tag{4.12c}$$

Based on the defined base values and parameter data provided by C4.49, $L_{pu} = 0.1748$, $R_{pu} = 0.0039$, and $T_e = 0.0006$. When $\xi_{cc}^2 = 1$, Eq. 4.12 results in the following control parameters for the current control:

$$K_{p,cc,pu} = 0.2319$$
$$K_{i,cc,pu} = 1.6204$$

4.3.3.2 Stability Analysis of Current Control

C_f was neglected during the tuning process of the current control parameters. This is an acceptable approximation in the lower frequency range of the magnitude response as shown by Tang *et al.* [24]. However, the paper also shows that the estimate is not valid for the phase response. Hence, it was necessary to run a stability analysis of the actual control system with the calculated control parameters. The actual transfer function of the system included in the current control is expressed with Eq. 4.13 when the voltage on the AC terminal is regarded as system input and the current flowing through the LV/MV-transformer is defined as the output. The expression is derived from the matrix form in E. Liberdado's PhD thesis [43].

$$H_{LCL}(s) = \frac{R_f C_f s + 1}{L_f L_t C_f s^3 + (R_t L_f + R_f L_f + R_f L_t) C_f s^2 + (R_t R_f C_f + L_f + L_t)s + R_t} \tag{4.13}$$

Applying the calculated control parameters to the open loop transfer function for the current control generates a stable loop when all system parameters are represented with real values. A gain margin of 18.7 dB is well beyond the recommended minimum of 6 dB, while a phase margin of 76.7° is outside the suggested phase margin region of 30-60° [37]. But the system is stable and the control parameters are regarded as acceptable.

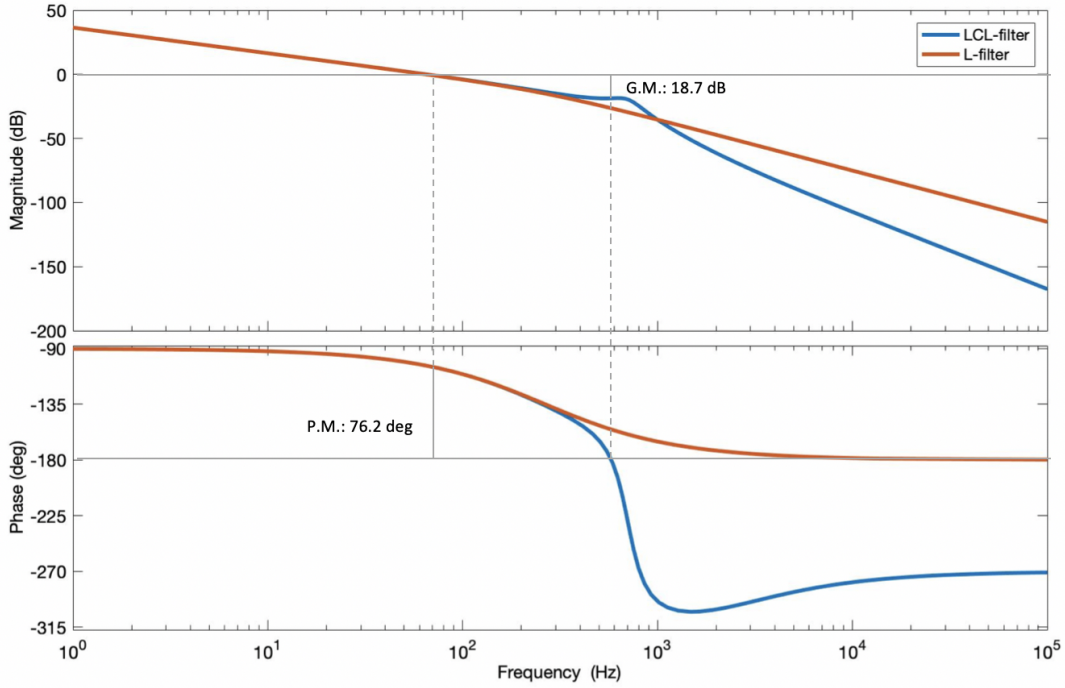

Figure 4.5: Comparison of open loop transfer function response for current control system when C_f is included (blue) and neglected (orange)

In addition to illustrate the stability margins of the current control system, Fig. 4.5 shows that neglecting C_f is a decent assumption for low frequencies. From around 280 Hz, an increasing deviation both in magnitude and phase shift is observed between the two transfer functions.

4.3.4 DC Voltage Control of a 2L-VSC

The purpose of the outer DC voltage control loop is to ensure optimum regulation and stability while the inner current control requires a quick response [8]. Therefore, one can consider the current control to be in steady-state when designing the DC voltage control and a linearization of the inner control loop is acceptable to simplify the transfer function of the outer control loop [8]. The linearization of the current control can be expressed as

$$H_{cc}(s) = \frac{1}{1 + sT_{eq}} \tag{4.14}$$

where $T_{eq} = 2T_e$ when an equal-area criterion of the steady-state error is applied [44]. By applying Kirchhoff's current law to the system, the current flowing through the capacitor can be expressed as

$$C_{DC}\frac{dv_{DC}}{dt} = i_{DC} - i_{wt} \tag{4.15}$$

Since power balance between the DC and AC side must fulfill

$$\frac{3}{2}v_d i_d = v_{DC} i_{DC} \tag{4.16}$$

when the d-axis is defined on the real axis, Eq. 4.15 can be expressed as the non-linear equation

$$C_{DC}\frac{dv_{DC}}{dt} = \frac{3}{2}\frac{v_d i_d}{v_{DC}} - i_L \tag{4.17}$$

The output of the DC voltage control is used as a reference for the d-component of the current and the control parameters of the PI-regulator should be selected with a linearized representation of the system model around the operating point [32]. Hence, the current injected from the wind turbine can be used as feed-forward. In this way, the DC voltage control will only provide compensation for the error. Fig. 4.6 depicts the block representation of the outer DC voltage control loop. The feed-forward term of the current is derived from Eq. 4.17 at equilibrium when $i_{C_{DC}} = 0$.

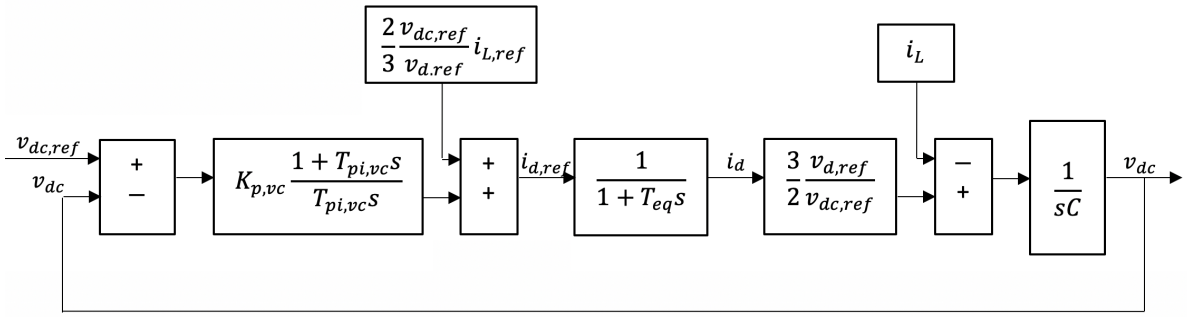

Figure 4.6: Block diagram of the outer DC voltage control loop

In pu-representation, the open loop transfer function of the DC voltage control can be written as

$$G_{vc,ol}(s) = K \cdot K_{p,vc,pu}\frac{1+T_{vc,pu}s}{T_{vc,pu}s} \cdot \frac{1}{1+T_{eq}} \cdot \frac{1}{\tau_c s} \tag{4.18}$$

where $K = V_{d,pu}/V_{dc,pu}$ and $\tau_c = 1/(\omega_b C_{dc,pu})$ [32]. The control parameters can be tuned with the symmetrical optimum method with the goal of maximizing the phase margin at the crossover frequency where $|G_{vc,ol} = 1|$ [32]. By differentiating the expression for the phase of $G_{vc,ol}$, the maximum phase margin is found at

$$\omega_D = \sqrt{\frac{1}{T_{vc,pu} T_{eq}}} \tag{4.19}$$

which is symmetric about $1/T_{vc,pu}$ and $1/T_{eq}$. Hence, the phase at ω_D can be written as

$$\angle G_{vc,ol}(\omega_D) = -180^o + \Phi_m \tag{4.20}$$

where

$$\Phi_m = tan^{-1}\left(\sqrt{\frac{T_{vc,pu}}{T_{eq}}}\right) - tan^{-1}\left(\sqrt{\frac{T_{eq}}{T_{vc,pu}}}\right) \tag{4.21}$$

Due to the symmetrical properties, the relationship between $T_{vc,pu}$ and T_{eq} can be expressed as

$$T_{vc,pu} = T_{eq} a^2 \tag{4.22}$$

where $a = \sqrt{T_{vc,pu}/T_{eq}}$ is the symmetrical distance from $1/T_{vc,pu}$ to ω_D and from ω_D to $1/T_{eq}$ [32, 44]. a gives the system one degree of freedom and should be decided based on a trade-off between the presence of oscillations and speed of system response. An expression for $K_{p,vc,pu}$ is found by calculating $|G_{p,vc,pu(\omega_D)}| = 1$. The general expressions for the control parameters for DC voltage control in pu-representation when symmetrical optimum is applied are as follows

$$K_{p,vc,pu} = \frac{\tau_c}{K T_{eq} a} \tag{4.23a}$$

$$T_{pi,vc} = T_{eq} a^2 \tag{4.23b}$$

$$K_{i,vc,pu} = \frac{K_{p,vc,pu}}{T_{pi,vc}} \tag{4.23c}$$

Based on the defined base values and parameter data provided by C4.49, $\tau_c = 0.1431$, and $T_{eq} = 0.0012$. $K = 1$ under the assumption of ideal conditions. With $a = 2$, Eq. 4.12 results in the following control parameters for the current control:

$$K_{p,vc,pu} = 1.1703$$
$$K_{i,vc,pu} = 243.815$$

4.3.4.1 Stability Analysis of DC Voltage Control

Applying the calculated control parameters for the DC voltage control gave a satisfactory phase margin of 36.9°. The response is depicted in Fig. 4.7.

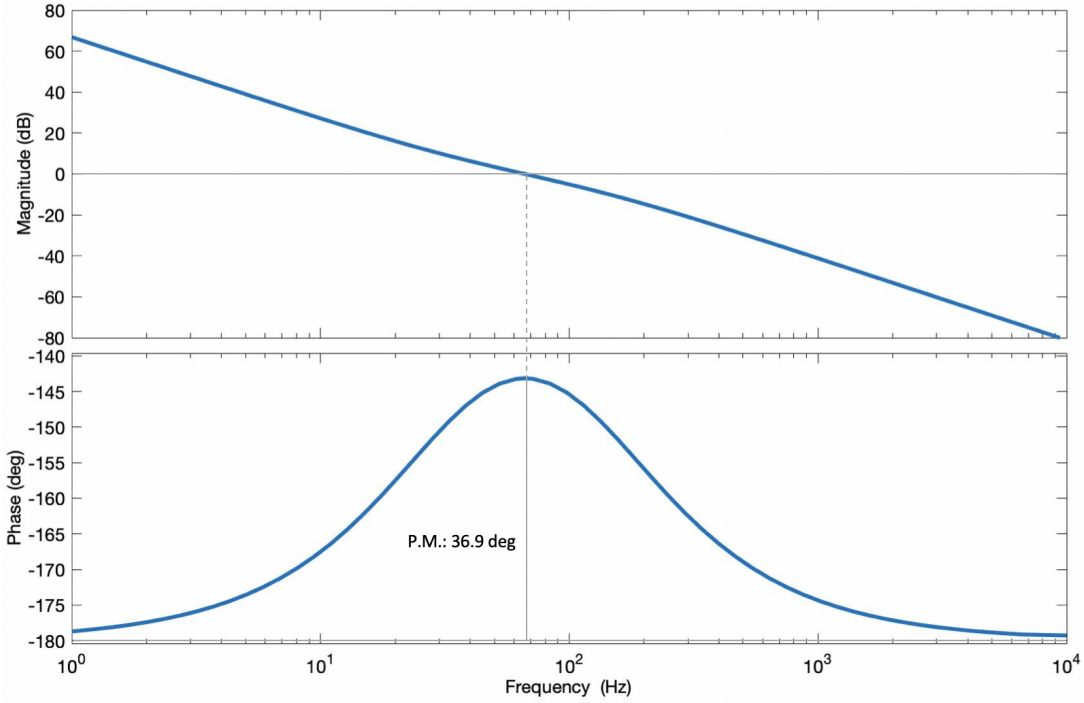

Figure 4.7: Open loop transfer function response for DC voltage control

Chapter 5

Modelling Approaches And Limitations

This chapter consists of two parts. Section 5.1 covers the modelling process of the benchmark systems, while section 5.2 presents the results from the frequency scan of the converters.

5.1 Simulation Models of the Benchmark Systems

Simulation models of the two benchmark systems have been built in Matlab/Simulink based on the topology and control theory presented in the two previous chapters. During the modelling process it has been necessary to test the system at different stages. Therefore, the five different cases described in Table 5.1 have been defined.

The first part of the chapter will present the simulation results from the different cases. First, the system response from case 1, which corresponds to benchmark system 1, is presented before the model is expanded to case 2 where the model is representing 30 wind turbines. Then the requirement for shunt compensation is discussed before the results from case 3 and 4 are discussed. The results from the simulation of case 5, which is matching benchmark system 2, are given in the end.

The simulations have been run with rated power applied to the system after 0.3 s. A decrease to half-rated power is applied to the simulation after 1.5 s. THD has been calculated based on 15 cycles of the fundamental frequency starting 0.6 s after the step change in current was applied. As the base values of the control system are defined based on the transformer ratings, the rated power of the converters equals 7/9 in pu representation on LV and MV levels.

Table 5.1: Cases

Case	System Representation	Illustration
1	Representation of a single wind turbine connected directly to an ideal MV AC voltage source	Fig. 3.2
2	Representation of 30 wind turbines connected directly to an ideal MV AC voltage source	Fig. 3.2
3	Representation of a single wind turbine connected to the collection grid	Upper part of Fig. 3.4
4	Representation of 30 turbines connected to the collection grid	Upper part of Fig. 3.4
5	Representation of 58 wind turbines connected to the collection grid	Fig. 3.4

5.1.1 Case 1 and 2: Wind Turbine Modelling

A simulation model has been developed in Simulink based on the topology of benchmark system 1 as illustrated in Fig. 3.2. Since no specification of Z_g is has been provided by C4.49, the impedance is disregarded. Consequently, the representation of the single wind turbine is connected directly to an ideal MV AC voltage source. The configuration is suited for testing the functionality of the control applications. Hence, a simulation was run when the wind turbine was developed to represent 30 wind turbines as well. The analyses conducted includes a study of the controller's tracking capability, harmonic analysis, and the response from the PLL.

5.1.1.1 Case 1: System Response From Benchmark System 1

To ensure that the converter is capable of providing the desired power, the tracking capability of the reference signals has been studied. Fig. 5.1 shows a comparison of the reference and measured current in the *dq*-frame while the response from the DC voltage control is presented in Fig. 5.2. The current plots show how the current quickly responds to a step change in the controlled current source at 1.5 s. Fig. 5.2 shows that the DC voltage is maintained stable. Ripples are present due to the switching of the IGBTs in the converter and the magnitude of the ripples increases once the wind turbine is injecting power. Still, the peak-to-peak value of the ripples are kept within the designed limit of 5%.

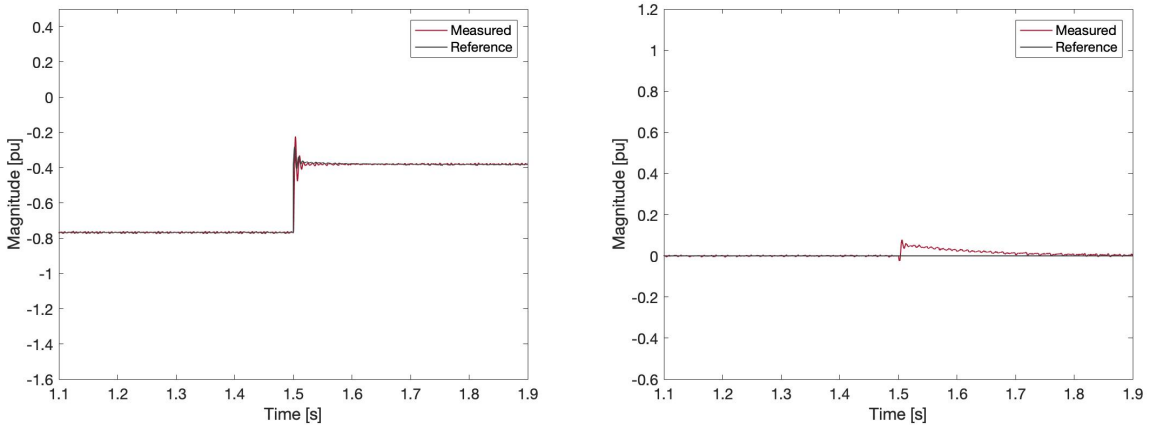

(a) Measured and reference current on the d-axis (b) Measured and reference current on the q-axis

Figure 5.1: Current tracking capability

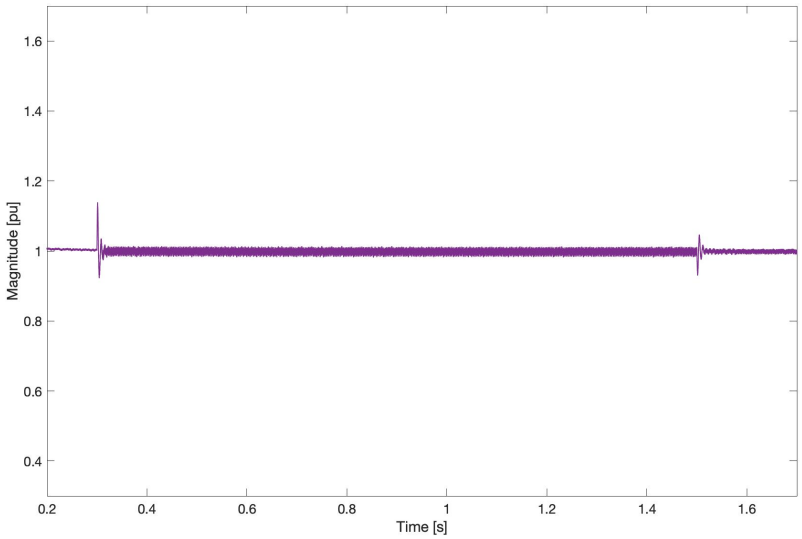

Figure 5.2: Voltage over DC-link capacitor

Fig. 5.3 presents the phase voltages and currents on the LV-side of the converter when the wind turbine is injecting rated power. The choice of studying the harmonic content on the LV-side of the transformer is simply due to the fact that the infinitely strong grid suppresses any voltage harmonics on the MV-side. Some distortion is observed and the results from a Fast Fourier Transform (FFT) analysis conducted in Simulink are provided in Fig. 5.4 and 5.5. The THD is 3.15% and 1.00% for the voltage and current, respectively. The major contribution comes from values around the switching frequency and multiples of those, but there is also some contribution from low-order harmonics.

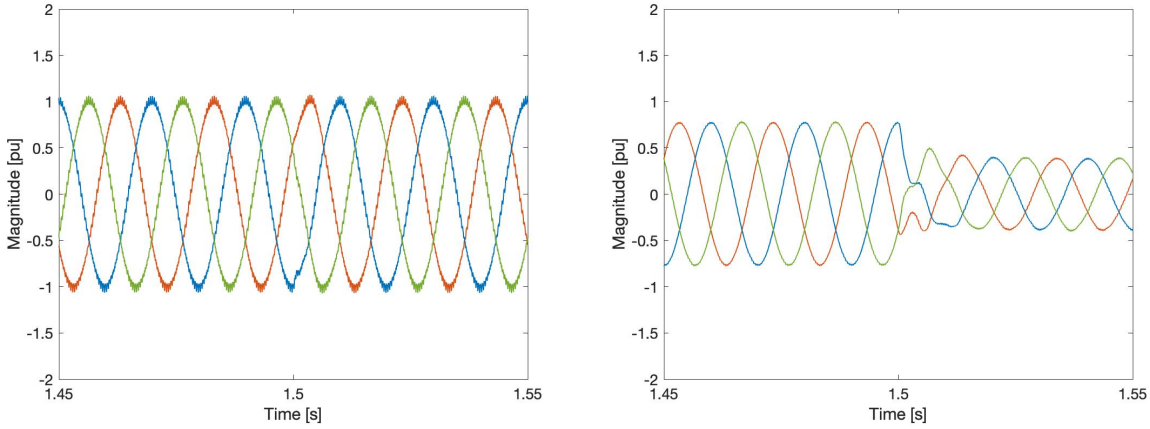

(a) LV phase voltage (b) LV phase current

Figure 5.3: Voltage and current on LV-side of transformer

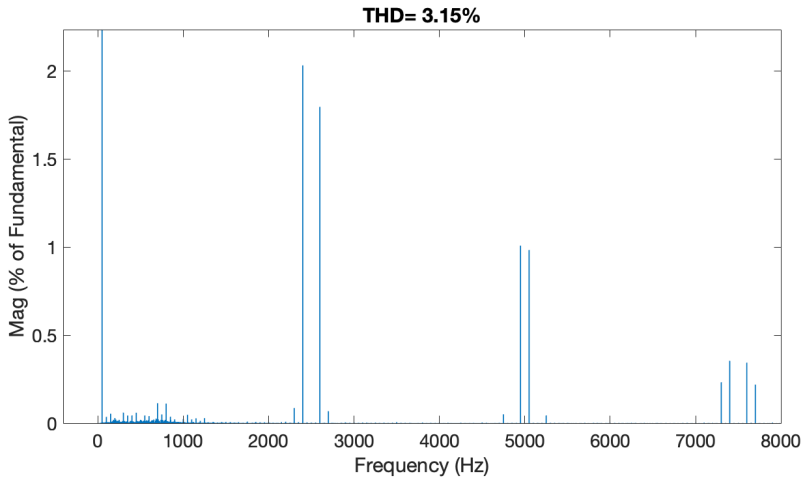

Figure 5.4: Voltage harmonic components on LV-side of transformer

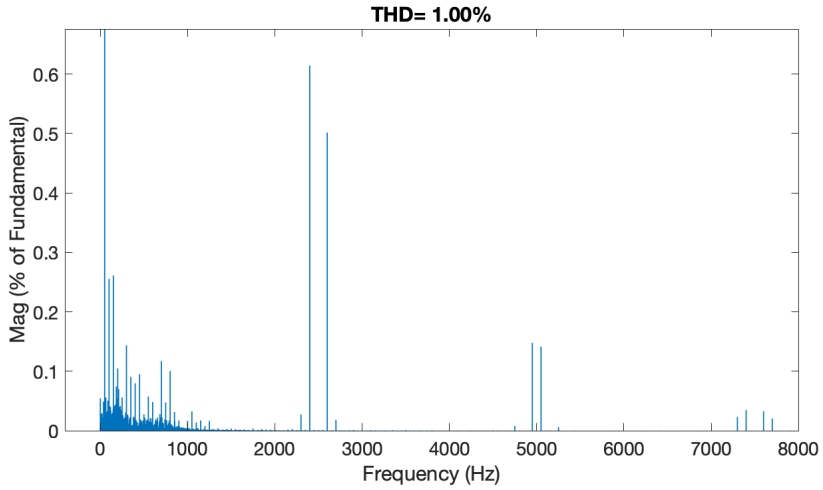

Figure 5.5: Current harmonic components on LV-side of transformer

The response from the PLL is shown in Fig. 5.6. It is observed that the angle, θ, is increasing linearly from 0 to 2π over a period of 1/50 Hz and that the rotational speed, ω, is stable at 1 pu.

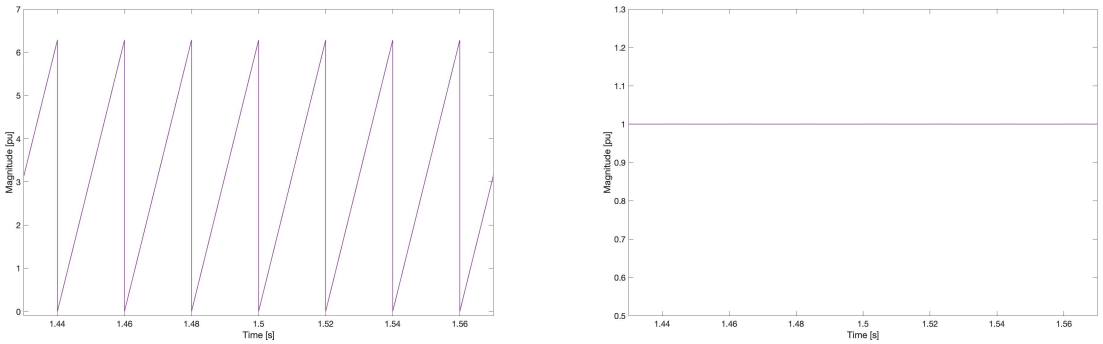

(a) Angle used for abc to dq transformation (b) Omega used in the control system

Figure 5.6: Response from the PLL

5.1.1.2 Case 2: System Response When A Represents 30 Wind Turbines

Because the generating units A and B in benchmark system 2 are representing 30 and 28 wind turbines, it has been necessary to implement an up-scaling possibility of the simple wind turbine model in benchmark system 1. Since the control system of the converter has been designed in pu, this was done by updating the rated power of the system and scale the passive components correspondingly. By multiplying the rated power of the simple wind turbine model with the desired number it should represent, N_a, the required size of the DC-link capacitor was automatically updated as its size is calculated with Eq. 3.1. Despite that the value of the filter inductance was given directly from C4.49, the value of the component had to be updated. Its relationship to the rated power can be seen from Eq. 3.2 showing that L_f should decrease with a factor of N_a. As C_f is design to provide 5% of the rated power, this parameter must increase with N_a. R_d is updated automatically according to Eq. 3.6. To ensure a stable system and avoid a change in the resonance frequency, the ratio between L_f and the internal inductance in the LV/MV transformer, L_t, should remain the same. The change in L_f was compensated for in the transformer by scaling the rated power of the transformer with N_a. The scaling of the initial wind turbine model revealed that the default value of the internal resistance in the IGBT bridge had significant impact on the results. The converter will cause losses in reality. However, as this parameter is not provided from the working group and additional resistance will provide damping to the system, the internal resistance of the IGBT was reduced to 10^{-8} Ω.

Running the simulation with an up-scaled system representing 30 wind turbines generated identical graphical results as the ones obtained from a single wind turbine representation. Only minor variations in the order of $0.01 - 0.02\%$ were observed from the THD analysis.

5.1.2 Grid Connection: Need for Reactor Compensation

The long HVAC cable causes a significant voltage rise on the converter side of the cable connection due to its large capacitance. Hence, compensation was required and a static shunt rector was implemented on the wind turbine side of the HVAC cable. Delta-connection was chosen over wye-connection as this configuration should trip triplen current harmonics under balanced conditions [17]. When estimating the necessary size of the compensation device, L_{sr}, the grid as modelled in benchmark system 2 was decoupled from the generating units at MV1 and MV2 and connected to a large load of 10^5 Ω. Table 5.2 presents the different voltage levels and reactive power flow in the grid without any shunt compensation. The measured voltage levels correspond to the peak value of the phase voltage, $V_{ph-gr,pk}$, while Q_{1ph} refers to the reactive power flow per phase. The different measured locations are specified in Fig. 3.4 in terms of voltage levels.

Table 5.2: Voltage levels and reactive power in the grid without reactive compensation

Measured	**EHV**	**HV2**	**HV1**	**MV2a**	**MV2b**	**MV1a**	**MV1b**
$V_{ph-gr,pk}$ [pu]	1.0	1.098	1.138	1.139	1.139	1.139	1.139
Q_{1ph} [MVA]	-97.98	-107.80	-0.34	-0.27	-0.38	0	0

The inductive shunt compensation per phase can be estimated from Eq. 5.1 where V_{HV1} and V_{HV2} refer to the phase voltages on the two sides of the HVAC cable. The expression is written in more detail in Eq. 5.2 since the measured voltages from the simulation are of the magnitude and in pu. As introduced in Table 3.1, V_{HV} represents the rms value of the rated line-to-line voltage at HV level.

$$L_{sr} = \frac{V_{HV1} \cdot (V_{HV1} - V_{HV2})}{\omega \cdot \Big(Q_{1ph,HV1} - Q_{1ph,HV2}\Big)} \tag{5.1}$$

$$L_{sr} = \Big(\frac{V_{HV}}{\sqrt{2}\sqrt{3}}\Big)^2 \cdot \frac{V_{ph-gr,pk,HV1} \cdot \Big(V_{ph-gr,pk,HV1} - V_{ph-gr,pk,HV2}\Big)}{\omega \cdot \Big(Q_{1ph,HV1} - Q_{1ph,HV2}\Big)} \tag{5.2}$$

The inductors are connected phase to phase. Thus, the estimated value of the per phase inductance must be transformed to an equivalent value in delta-configuration which can be done with Eq. 5.3 [45] where the sub-scripts a, b, c, n stands for phase a, b, c and neutral and refer to the point of coupling. Since a balanced system is assumed and L_{sr} will be the same in each phase, the transform to delta-configuration equals multiplying the calculated value of L_{sr} from Eq. 5.2 with 3.

$$L_{ab} = \frac{L_{an}L_{bn} + L_{an}L_{cn} + L_{bn}L_{cn}}{L_{cn}} \tag{5.3}$$

Based on the results generated from the simulation without any compensation, the required inductance was calculated to be 0.5438 H for wye-connection and 1.632 H for delta-configuration. The new voltage levels and reactive power flow after the compensation are presented in Table 5.3.

Table 5.3: Voltage levels and reactive power in the grid with reactive compensation

Measured	**EHV**	**HV2**	**HV1**	**MV2a**	**MV2b**	**MV1a**	**MV1b**
$V_{ph,pk-pk}$ [pu]	1.0	1.004	0.971	0.971	0.972	0.971	0.972
Q_{1ph} [MVA]	-3.52	-3.77	-0.25	-0.20	-0.28	0	0

The results show a significant decrease in the reactive power flowing towards the grid from the HVAC cable. As a result, the voltage levels are considerably improved. A comparison of the deviation from the rated voltage levels with and without shunt compensation is given in Table 5.4.

Table 5.4: Comparison of voltage level variations with and without shunt compensation relative to rated conditions

Lsr	**EHV**	**HV2**	**HV1**	**MV2a**	**MV2b**	**MV1a**	**MV1b**
No	0.0 %	9.8 %	13.8 %	13.8 %	13.9 %	13.9 %	13.9%
Yes	0.0 %	0.4 %	-2.9 %	-2.9 %	-2.9 %	-2.9 %	-2.8 %

5.1.3 Case 3 and 4: Modelling of Wind Turbine Connected to the Grid

With the shunt reactor implemented, the model of the wind turbine was connected to the grid. Two simulations were run where A was representing a single and 30 wind turbines, respectively.

5.1.3.1 Case 3: System Response When A Represents A Single Wind Turbine

The settling time from the simulation started until rated power was applied at 0.3 s seemed to be a bit longer and contained more fluctuations than for the previous cases. Fig. 5.7 shows the settling time for V_{DC}, the reference signal to the PWM, and for the line currents in the dq-frame. However, THD measurements from time intervals when rated and half-rated power was injected showed that the connection to the grid did basically not affect the system response in steady-state as the largest deviation in THD levels from previous results was found to be 0.4%. Thus, the graphical representations of the voltages, currents, θ, and ω presented for case 1 are still representative and no further investigation was conducted at this point.

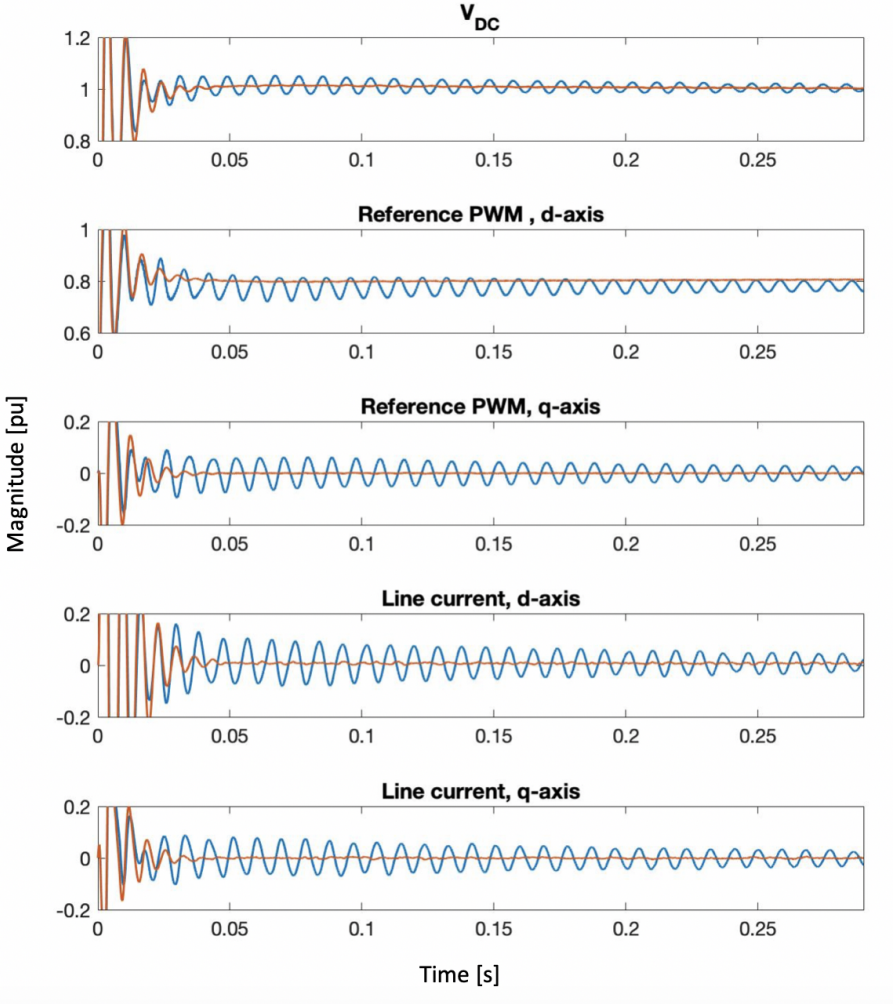

Figure 5.7: Comparison of case 1 (orange) and case 3 (blue) of the settling time for various signals before power is injected at t=0.3 s

5.1.3.2 Case 4: System Response When A Represents 30 Wind Turbines

The system responded differently from the three first cases when the up-scaled wind turbine representation was connected to the collection grid. The results showed that all signals were highly distorted when either no power or half-rated power was injected. The control system does under those operation conditions manage to track its references and the system does not reach instability. However, the reference signals are highly distorted and the control system is not capable of providing any attenuation of the harmonics present. The distortion was even reflected in the PLL which could not provide an ideal sawtooth shape of θ once the distortions were introduced. Fig. 5.8-5.11 present the inputs for the current control, DC voltage, voltage and current levels on the MV side of the LV/MV transformer as well as the response in the PLL.

FFT analyses revealed a tremendous increase in distortion from the lower frequency range. The AC voltage source is only injecting a signal with a fundamental frequency component. Hence, the low-order harmonic components must have been generated in relation to the converter. Examination of the PWM uncovered overmodulation of the reference voltage as seen in Fig. 5.12. The observation had to be further investigated.

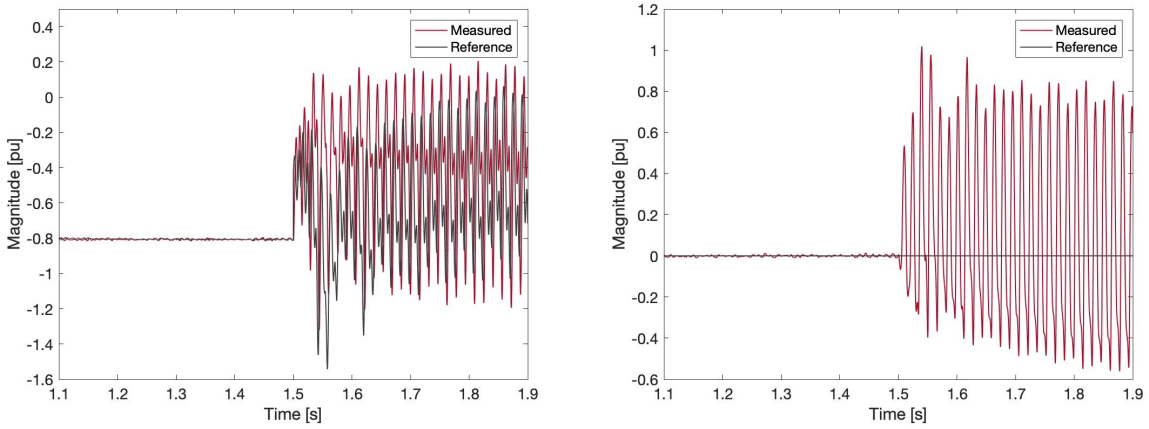

(a) Measured and reference current on the d-axis (b) Measured and reference current on the q-axis

Figure 5.8: Current tracking capability

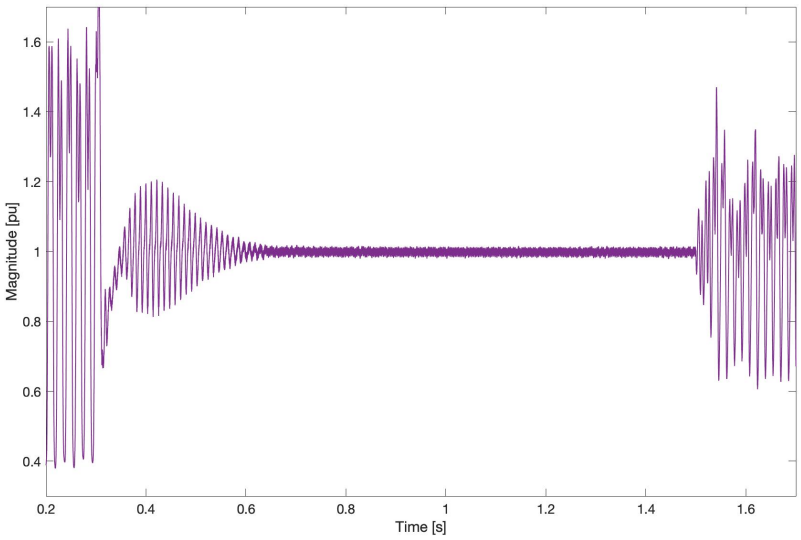

Figure 5.9: Voltage over DC-link capacitor

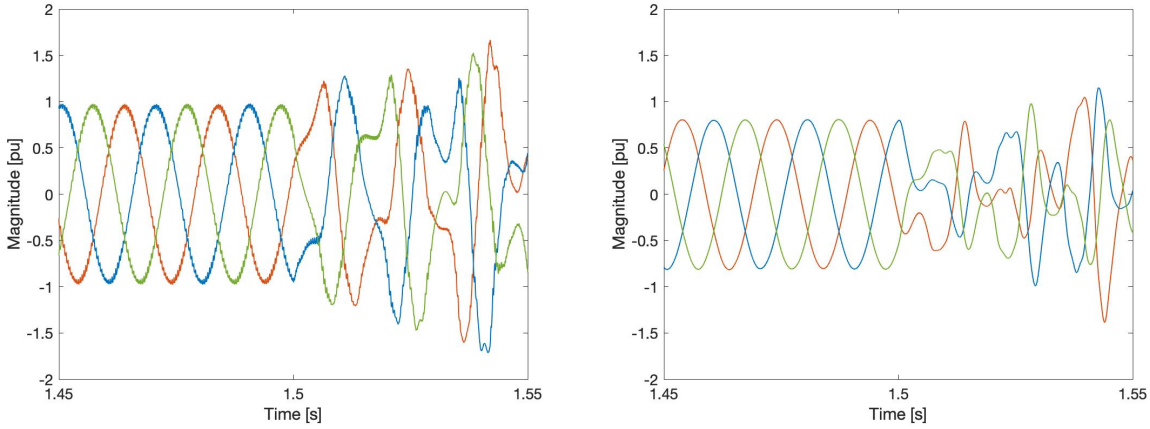

(a) MV phase voltage (b) MV phase current

Figure 5.10: Voltage and current on MV-side of LV/MV-transformer

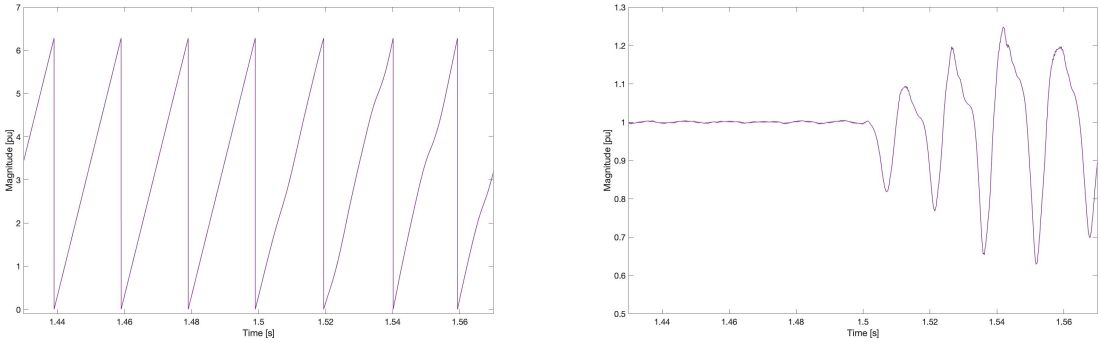

(a) Angle used for abc to dq transformation (b) Omega used in the control system

Figure 5.11: Response from the PLL

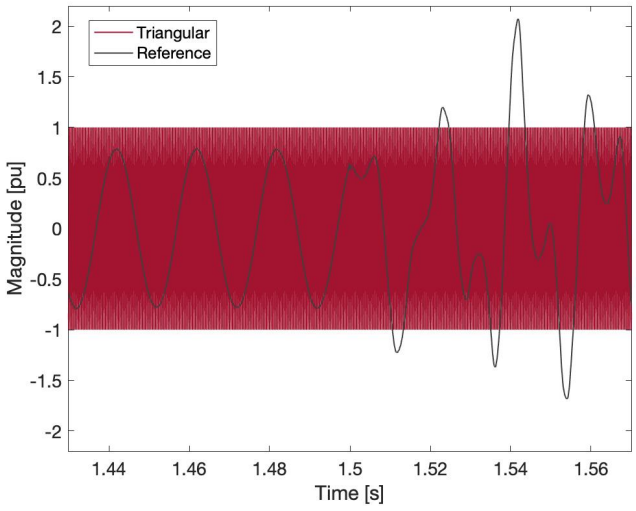

Figure 5.12: Reference voltage for phase a in the PWM

5.1.3.2.1 Cause of Low-Order Harmonic Distortion Operating in the overmodulation region generates low-order harmonics on the AC-side of the converter [46]. Therefore, the presence of a voltage reference with a magnitude higher than 1 pu can itself be an explanation to the generation of low-order harmonics. However, this does not explain reason for entering the overmodulation region in the first place.

In order to find the cause of overmodulation, one component after the other was modified to test its effect onto the system. Since the up-scaled representation of A provided the desired response when connected to an ideal 34 kV AC grid, the initial suspicion was related to possible resonances. However, it turned out that the problem was introduced once the feed-forward to the control system was not an ideal voltage source. Testing showed that disconnecting the feed-forward of the voltage signals provided a satisfactory response. As the converter is the most complex element in the circuit, the IGBT bridge was replaced with an average model representing the required AC voltage on the AC terminals of the converter. The simplification did not solve the problem. This narrowed down the possible sources of the distortion a lot because the only elements left that differed between a representation of a single and 30 wind turbines were the components of the LCL-filter. The overmodulation was removed once the filter capacitor was disconnected. Ergo, the source of the problem was detected.

Section 5.1.1.2 described how an up-scaling of the generating unit caused C_f to be amplified with N_a while L_f and L_t were reduced with a factor of $1/N_a$. Consequently, the more wind turbines to be represented by the converter, the higher capacitance and the lower inductance. The most reasonable explanation to the distortion gave the impression of being related to the charging and discharging currents of C_f. Investigations showed that the issue was solved once C_f was disconnected or even placed outside the defined boundaries of the converter. Therefore, such a big power exchange between the DC and the AC side within the borders of the converter's control system seemed to be a critical aspect. This power exchange could have been avoided if L_f was capable of balancing the charging and discharging of C_f. The necessary rms current to fulfill this requirement was calculated using the energy storage equations in Eq. 5.4 for inductors and capacitors [18]. For the purpose of analysis, the system was assumed to be under ideal conditions (rated values).

$$w_L = \frac{1}{2}Li^2 \tag{5.4a}$$

$$w_C = \frac{1}{2}Cv^2 \tag{5.4b}$$

Using the up-scaled parameters for L_f and C_f resulted in a required rms current, $I_{ph,rms}$, of 181.66 kA ($N_a = 30$). Hence, it would be of interest to find the DC current needed to achieve this. As a direct result of power balance between the DC and AC side, the power in one phase can be expressed by the DC states as follows

$$V_{ph,rms}I_{ph,rms} = \frac{1}{3}V_{DC}I_{DC} \tag{5.5}$$

Under rated conditions for the AC side and the DC voltage, I_{DC} must equal 135 kA. This results in a ratio of $I_{DC}/I_{ph,rms} = 0.86605$ and expresses the relationship between the DC current and the rms currents in the different phases. As a consequence, the required DC current to obtain a power balance between L_f and C_f becomes 157.33 kA for the scenario where the generating unit is representing 30 wind turbines. This value can be obtained if V_{DC} is set to 1716 V.

Further analysis was conducted to better understand the relationship between the required DC voltage level, presence of distortion, and number of wind turbines. Fig. 5.13 shows how the difference in energy storage capability between the inductor and capacitor increases with the increasing number of wind turbines to be represented by the converter.

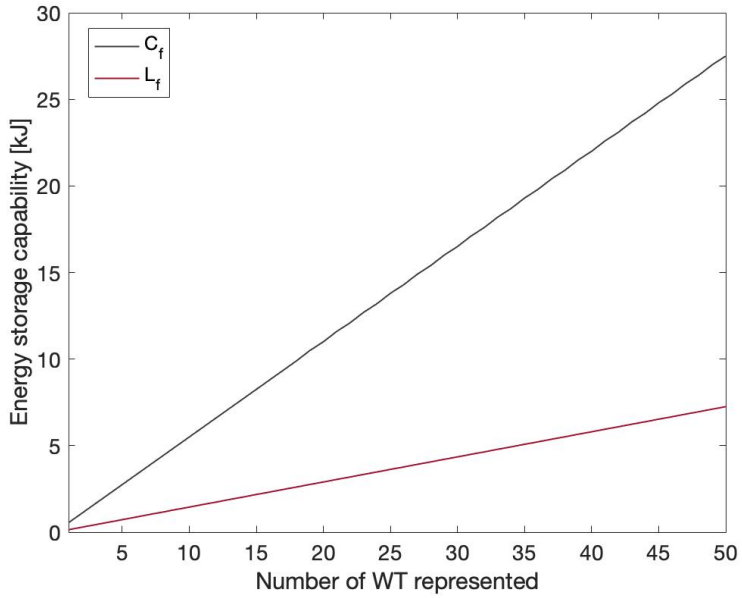

Figure 5.13: Energy storage capability under initial rated conditions

$I_{ph,rms}$ is proportional to N_a and so is I_{DC}. Consequently, V_{DC} should be 1716 V regardless of the scaling factor to achieve an equivalent energy storage capability for L_f and C_f. Hence, the results indicate that there might exist a compromise where a decrease in the DC voltage level provides the sufficient rms AC current without being actively controlled. Theoretically speaking, one could assume that the adjustment of the DC voltage level would provide no upper limit of wind turbines to be represented by the equivalent converter. However, once other passive components outside the generating unit are present, the system voltages and currents are not ideal anymore. Testing in Matlab/Simulink showed that changing V_{DC} to 1720 V was a sufficient solution for a scaling of up to around 40 wind turbines. This was valid both when the DC side was represented as a stiff DC source and when it was replaced with an actual capacitor.

5.1.3.2.2 THD Levels When V_{DC} Is Adjusted to 1720 V The following diagrams present the THD levels for case 4 at different locations in the grid when V_{DC} is changed to 1720 V. The results display the response for both voltages and currents when rated and half-rated power is injected. It is observed that the change in power injected has a very small effect on the voltage distortion level, while for the current the noise doubles. Still, the figures demonstrate that levels of distortion are within acceptable limits when using the IEEE 519 standards as reference. Also, FFT analyses ensured that no single harmonic component exceeded the recommended limits.

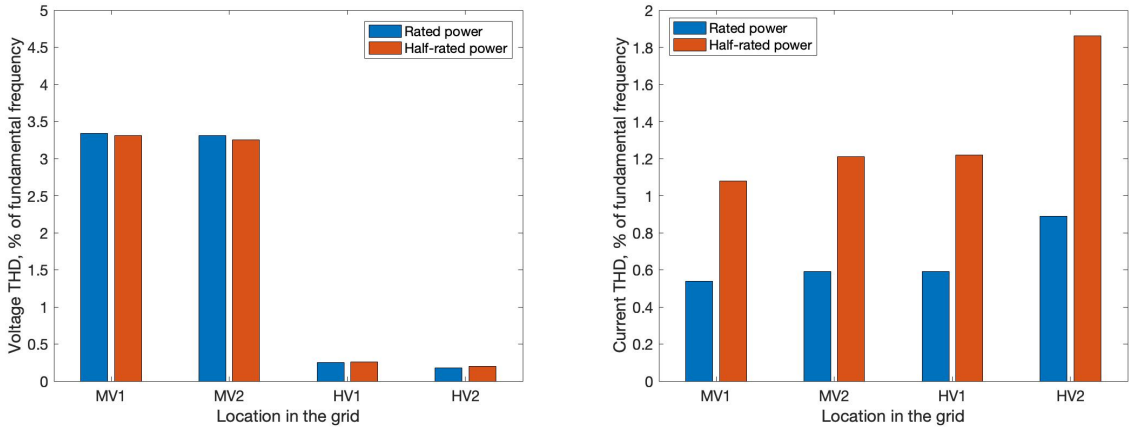

(a) Voltage THD

(b) Current THD

Figure 5.14: THD at different locations in the grid

5.1.3.2.3 Impact of Changing the DC voltage Level for Case 3 The analysis of possible causes to the tremendous harmonic distortion from low-order harmonic frequencies states that V_{DC} should be 1716 V for all values of N_a to obtain an equivalent energy storage capability for L_f and C_f. Despite that case 3 was considered as functional, some fluctuations were observed in the settling time. Therefore, it would be interesting to see if the change in the DC voltage level also causes any visible changes in the control response when the converter is only representing a single wind turbine. A comparison of the measured signals from V_{DC}, PWM, and line currents in the dq-frame in case 3 with the two different DC voltage levels is presented in Fig. 5.15. The results show that the fluctuations are damped faster when V_{DC} is 1720 V. Also the settling time seems to improve with the new DC voltage level.

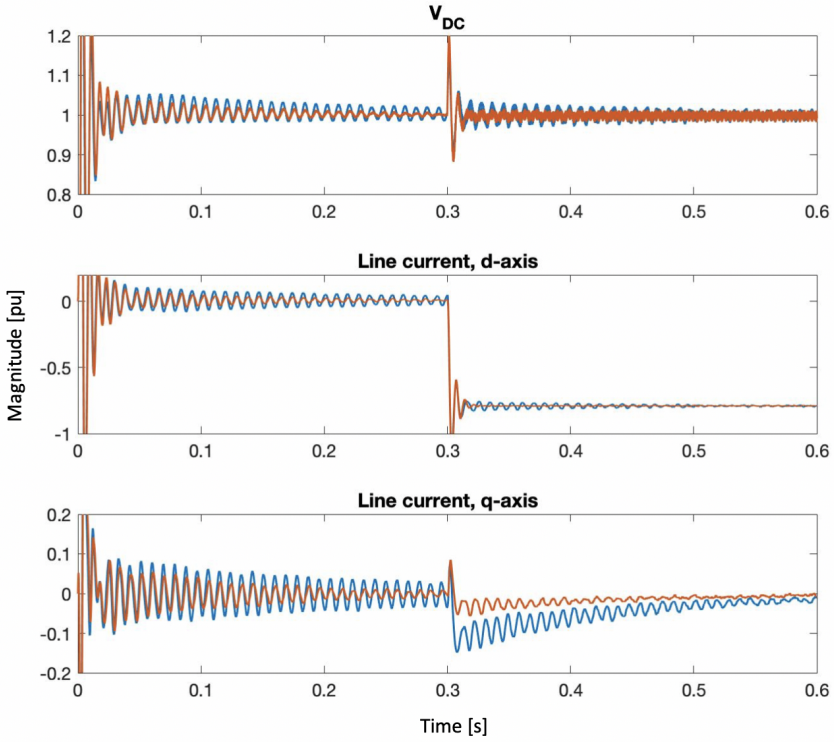

Figure 5.15: Comparison of V_{dc}=1720 V (orange) and V_{dc}=2000 V (blue) in case 3 for various signals before and after rated power is injected at t=0.3 s

5.1.4 Case 5: Modelling of Benchmark System 2

Once case 4 provided the desired response, the model was expanded to two generating units. In consistency with the system presented before, A and B were connected at the HV-side of the park transformer. The two generating units were modelled with independent control system with inputs taken from the MV-side of the LV/MV transformers.

5.1.4.1 Case 5: System Response from Benchmark System 2

Fig. 5.16 and 5.17 present the THD at different locations in the grid when rated and half-rated power is injected to the grid. As observed for case 4, the current harmonic distortion increases significantly when less power is injected from the wind turbine cluster. Further, it is observed that the distortion is higher for converter B than A. The noise level decreases the closer the measured location is to the grid. Fig. 5.18a-5.21b presents the FFT analysis of the different THD levels when rated power is injected.

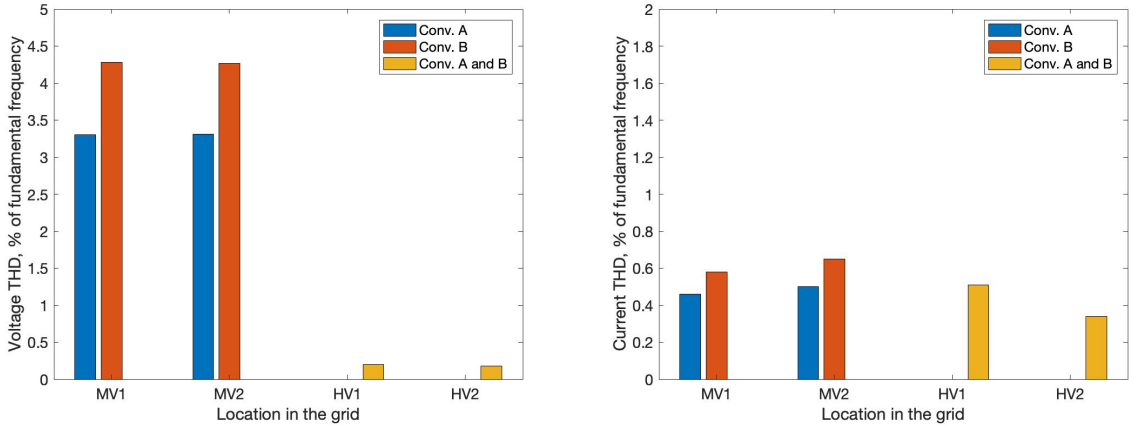

(a) Voltage THD at rated power (b) Current THD at rated power

Figure 5.16: THD at different locations in the grid with rated power injected

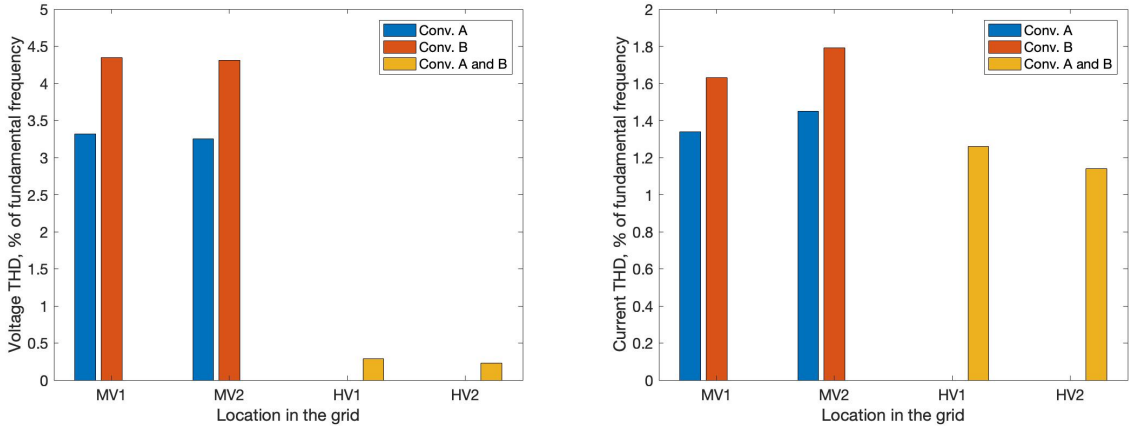

(a) Voltage THD at half-rated power (b) Current THD at half-rated power

Figure 5.17: THD at different locations in the grid with half-rated power injected

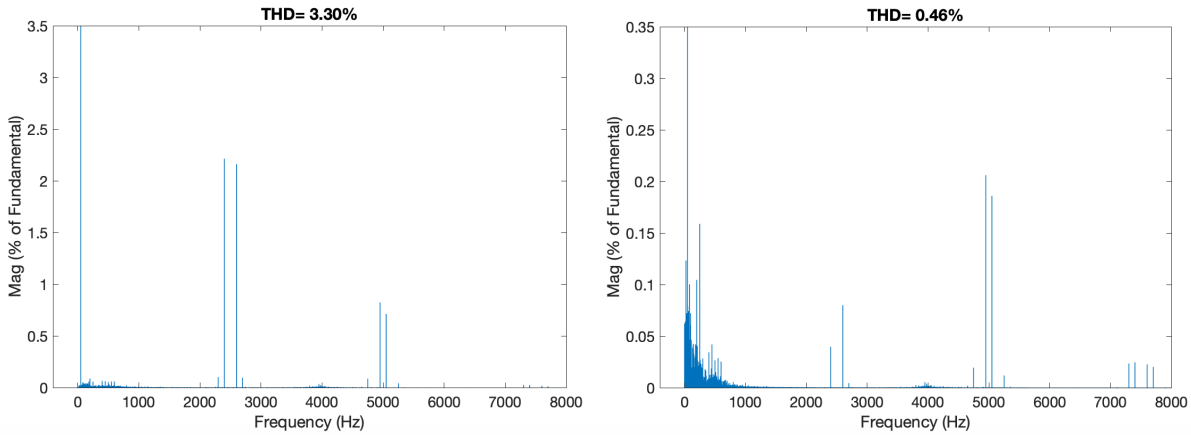

(a) Voltage harmonics (b) Current harmonics

Figure 5.18: Harmonic components at MV1a with rated power injected

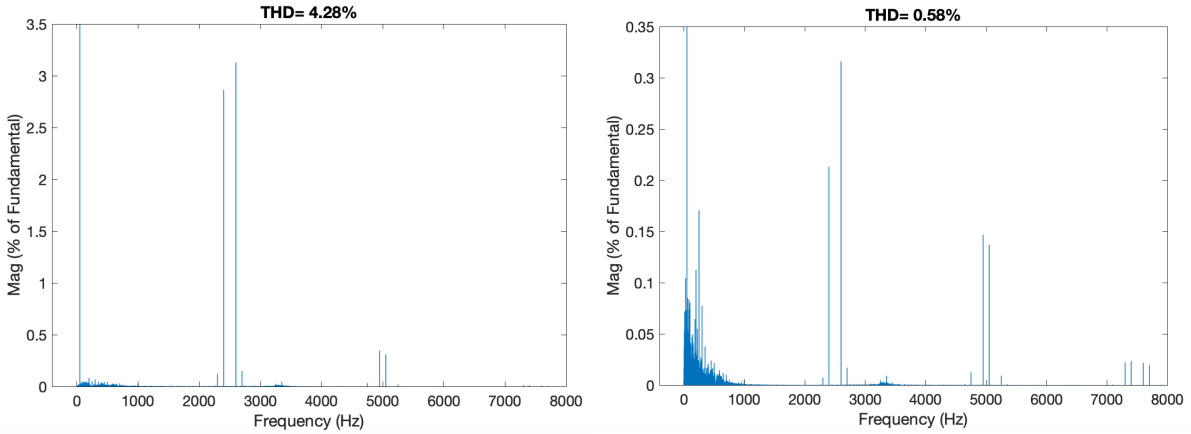

(a) Voltage harmonics (b) Current harmonics

Figure 5.19: Harmonic components at MV1b with rated power injected

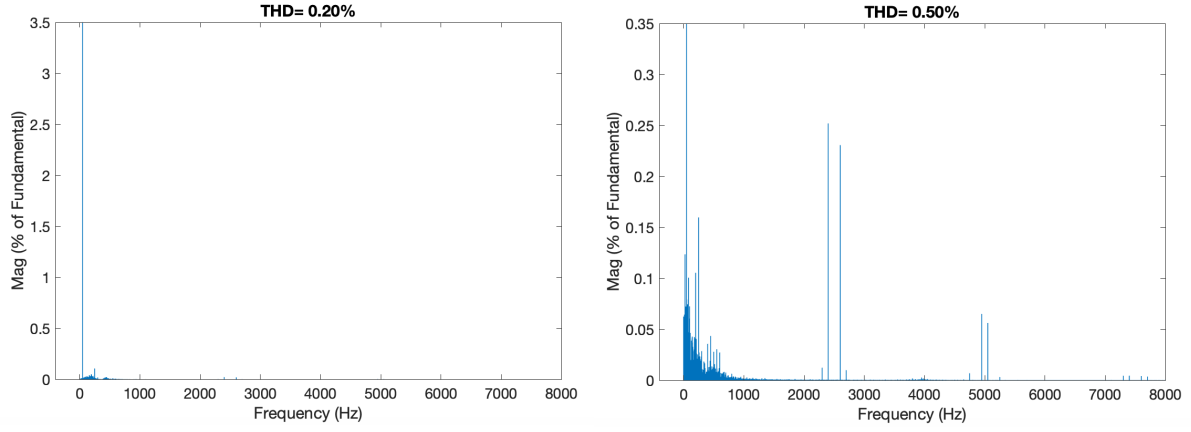

(a) Voltage harmonics (b) Current harmonics

Figure 5.20: Harmonic components at HV1 with rated power injected

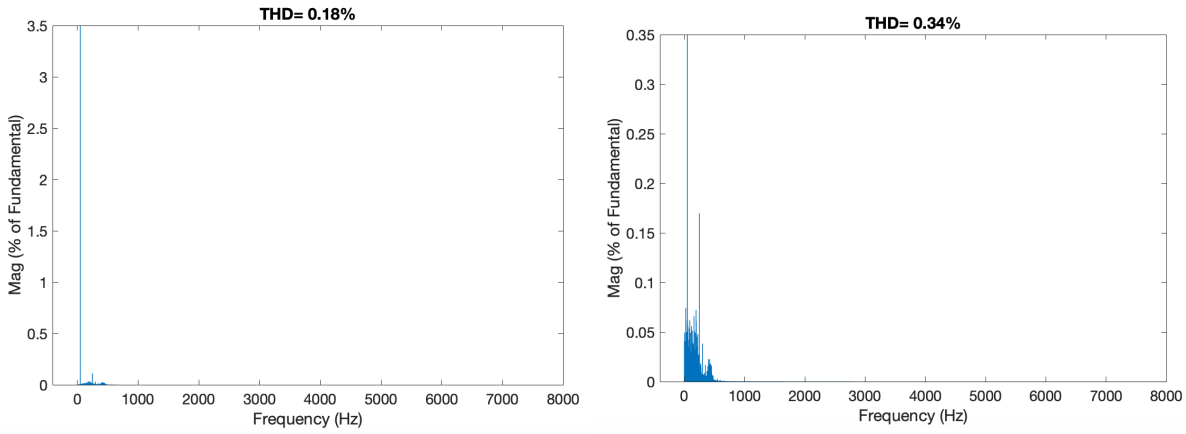

(a) Voltage harmonics

(b) Current harmonics

Figure 5.21: Harmonic components at HV2 with rated power injected

The FFT analyses clearly show how the high-order harmonics are more and more reduced the further away from the converters the analysis is conducted. The presence of low-order harmonics on the other hand, seems to be rather stable. A close-up of the frequency components up to 1000 Hz of the signals from MV1a, MV1b, HV1, and HV2 with rated power is provided in Appendix D. Despite that the harmonic components are small, those plots show that the major contribution on HV-level comes from the 5^{th} harmonic component at 250 Hz. At the connection point, MV1, for A and B the contribution is more widespread even though the 5^{th} harmonic stands out in the analysis of the current harmonic components here as well.

5.2 Frequency Responses in the Benchmark Systems

C4.49's work is related to multi-frequency stability in terms of interactions and resonances between physical components in the grid and the converter control. From an analytical perspective, it will be necessary to know something about at which frequencies the possible resonances can occur. Such an analysis requires knowledge of the characteristics of the converters which, due to their non-linear features, are more challenging to estimate than the rest of the system.

The external behaviour of VSCs can be modelled as a current source in parallel with an impedance where the impedance represents the frequency characteristics of the converter as measured on its terminals [47]. Different methods for expressing impedance models have been developed during the last couple of years. M. Cespedes and J. Sun present an analytical approach in [47] where a converter is modelled by a positive and negative sequence impedance in the phase domain. The paper concludes that the two sequences normally are decoupled and therefore can be studied independently from each other. The conclusion is questioned by M. K. Bakhshizadeh *et al.* in [48] who conclude that there exist couplings between the positive and negative sequences in the converter control even under balanced conditions. The latter paper

stresses that the couplings are important for the stability in the converter despite the small magnitude in the coupling terms.

Nyquist stability criterion and complex mathematical derivations for impedance modelling are considered as beyond the scope of this master thesis. Consequently, the subsequent section will present the frequency response of the converters without any impedance model strategy applied. A frequency scan has been used for the purpose.

5.2.1 Frequency Scan of the Converters in the Benchmark Systems

Simulink's block *Impedance Measurement* measures the impedance between two nodes as a function of the frequency. Unfortunately, the application does not consider nonlinear elements like converters [49]. Thus, the impedance measurement block cannot be directly applied to the Simulink models of the benchmark systems. The frequency scan has been conducted manually of the converters, which includes all components until the MV-side of the LV/MV transformer. Since the converter is operating at the fundamental frequency under normal operation, the scan was carried out by superimposing a small-signal waveform at a higher frequency and with a magnitude equal 1% of the rated voltage amplitude. The corresponding current component resulting from the injected disturbance was measured with Simulink's FFT analysis tool which allows to separate the different harmonic components in a signal from one another. The harmonic impedance was estimated by calculating the ratio between the harmonic voltage and current component. The procedure was conducted in the frequency range of 50-2000 Hz with rated power injected. Initially, the frequency scan was conducted with steps of 25 Hz. As the measurements especially for frequencies up to around 200 Hz did not generate any pattern, more data was required and simulations with smaller frequency steps were run for this region. Fig. 5.22 and 5.23 present the frequency response of the converters in the benchmark systems.

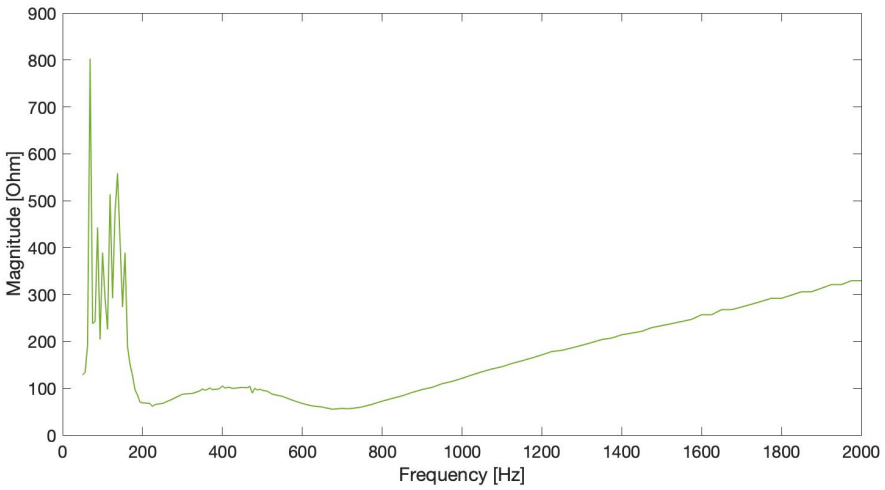

Figure 5.22: Frequency response from the converter in benchmark system 1

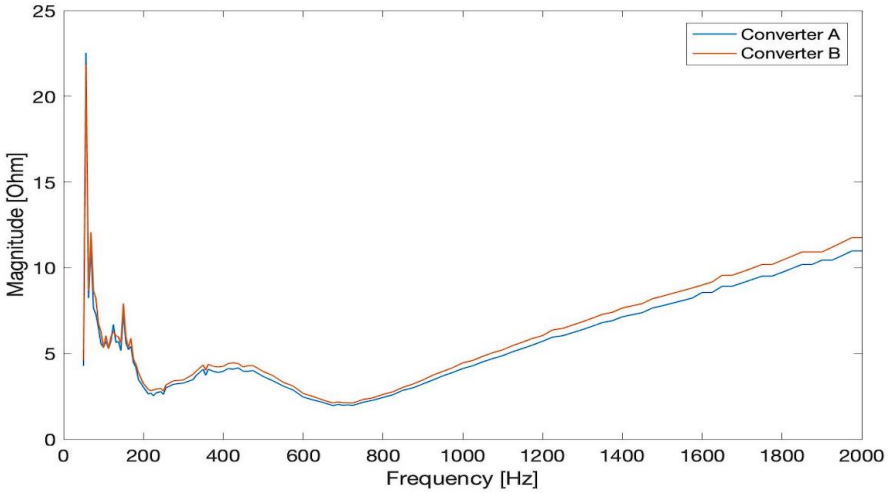

Figure 5.23: Frequency response from converter A and B in benchmark system 2

The base values of the converters depend on the number of turbines they are representing. Thus, the plots are not directly comparable in terms of magnitude values and a graphical representation in pu is provided below for the purpose.

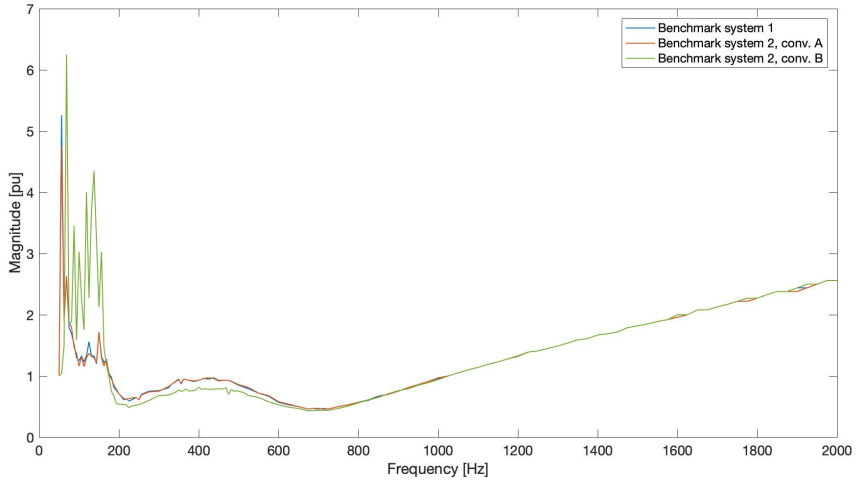

Figure 5.24: Comparison of frequency scans for the converters in benchmark system 1 and 2

The frequency response of the converters depicts a rather unpredictable response region for frequencies up to around 200 Hz. Even though it is observed some variation between the response from A and B in benchmark system 2 in this region, the most conspicuous observation is related to the different response between benchmark system 1 and 2. In addition to a higher impedance with more variation for the converter in benchmark system 1, it is observed that the first and most significant peak occurs at a slightly higher frequency than in benchmark system 2. The frequency response is much smoother above 200 Hz for all the converters. For frequencies between 200 and 2000 Hz, a local maximum is observed around 400 Hz and a global minimum is

detected around 700 Hz. It can be noted that the location of the global minimum corresponds to the resonance frequency of the LCL-filters. In the frequency range of approximately 200-700 Hz, it is observed that the impedance magnitude for the converters representing 30 and 28 wind turbines is slightly higher than for the one representing a single wind turbine. This may be due to the fact that benchmark system 1 has a DC-link capacitor calculated from a DC voltage of 2000 V, while it for benchmark system 2 has been adjusted to 1720 V. Still, the shapes of the waveforms follow each other at all times above 200 Hz.

5.2.1.1 Varying Operating Conditions

Due to the issues with the severe amount of harmonic distortion introduced in case 4 before the DC voltage level was adjusted, it was of interest to investigate if the frequency response could give any explanation. Two comparisons of different frequency scans are presented in Fig. 5.25 and 5.26. In Fig. 5.25, converter A is representing 30 wind turbines in all scenarios. The frequency scan from Fig. 5.23 is compared to the response when the converter is only injecting half-rated power and V_{dc} equals 1720 V and 2000 V, respectively. Fig. 5.26 compares the frequency response from converter A when it is representing a single wind turbine with the case when it is representing 30 wind turbines. Half-rated power is injected and the DC voltage level is set to 2000 V.

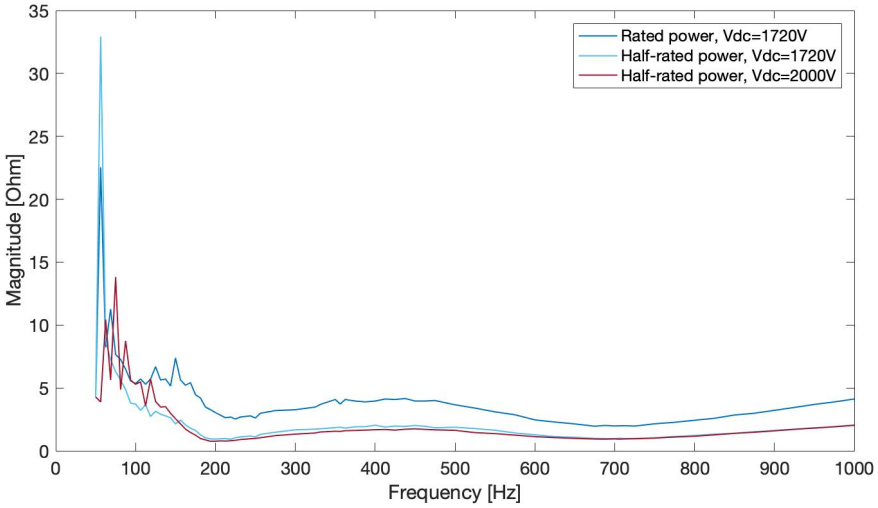

Figure 5.25: Comparison of frequency responses for converter A under different conditions

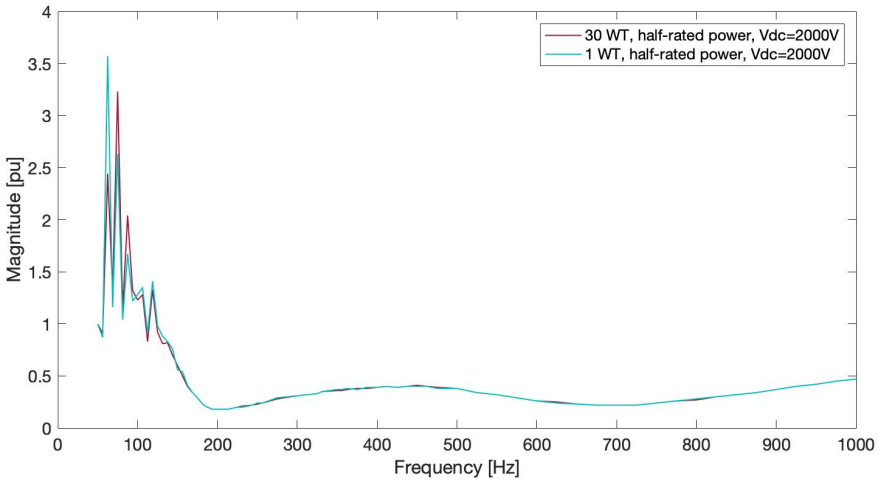

Figure 5.26: Comparison of frequency responses for converter A when representing a single versus 30 wind turbines

Once again, it is seen that the response from frequencies below 200 Hz is unpredictable and with a huge variation in the impedance magnitudes. But neither when comparing the different plots any clear coherence can be detected. The impact of a different DC voltage level seems insignificant for frequencies between 200 and 1000 Hz in Fig. 5.25. Further, the plots show a higher impedance magnitude in this region when rated power is injected. In 5.26, where a single versus 30 wind turbine representation is compared under the same operating conditions, the unpredictable and varying response is limited to frequencies up to only 100 Hz. Above this, the response is almost identical.

Chapter 6

Discussion

This chapter will discuss findings, issues, and results from the previous chapter. The modelling approaches and limitations of the benchmark simulation models will be discussed first before the the conduction of the frequency scan and its corresponding results will be reviewed.

6.1 Modelling Problem with the Benchmark Systems

Case 4 revealed a critical aspect with the modelling of the up-scaled wind turbine representation. The increasing difference in physical values between the filter inductor and filter capacitor gave the impression of causing a larger and larger uncontrolled power flow between the DC and AC side. The uncontrolled power flow is due to the fact that the two components are within the boundaries of the converter as seen from the control system. However, the sizing of the filter components seem reasonable when modelling a lumped representation of a wind farm cluster. Taking converter A as an example: The converter is representing 30 wind turbines configured with six strings which each has five turbines connected in line. As the current transmitted from the wind turbines further out is not flowing through the wind turbines closer to the transformer station, the turbines in one string are connected in parallel. Hence, the Thevenin equivalent of the filter inductance in one string equals $L_f/5$, while it becomes $5C_f$ for the filter capacitance. The total Thevenin equivalent of the filter impedance in converter A as seen from the resulting grid is derived from the parallel connection of 6 lumped representation of the strings. As a result, $L_{f,eq} = L_f/30$ and $C_{f,eq} = 30C_f$, which is exactly the same scaling that was applied to the model.

6.1.1 Introducing a Problem not Present in Reality

The lumped filter impedance used when the converters are representing N_a and N_b wind turbines is a reasonable modelling of the equivalent impedance as seen from the grid. Yet, the stability

issue and generation of low-order harmonics that arises in converter A due to the up-scaled filter impedance is not reflecting a real issue. In real-life applications, the difference in energy storage capability between the filter inductor and capacitor within each control system is small and does not cause a critical uncontrolled power flow between the DC and AC side of the IGBT bridge. Reducing the DC voltage level turned out to provide a solution to the problem when the converters were scaled to represent 30 and 28 wind turbines. Thus, the adjustment was applied to make the simulation model applicable for further analysis. However, the requirement for this modification is without doubt a weakness with the model.

6.1.2 Unsolved Issues Related to the Modelling Problem

Despite that an adjustment in the DC voltage level solved the distortion issue introduced in case 4, there are still some unexplained observations from the analysis. The main reason for running test cases during the modelling process was to intercept errors in the modelling at an early stage. Thus, case 2 was run to ensure that the up-scaled representation of a single wind turbine was functional. Hence, it is not explained why the decent results which insinuated a well-function system in case 2 were not reproduced in case 4. Neither has it been clarified why disconnecting the feed-forward of the voltage removed the distortion.

Common for the two observations is that their contribution to the control system is an ideal input (either 1 pu or 0 pu). In other words, neither of the two scenarios feeds the control system with voltage distortion. Changing the DC voltage level is a result of a solution based on that L_f should compensate for the whole charging and discharging of C_f. However, the filter capacitor is probably not drawing all power from the converter side initially. Thus, it is believed that the control system must be operating against itself since the reference current for the d-axis is zero when no power is injected from the turbine. This can potentially cause the distorted voltage waveform observed throughout the system and which is fed into the current control.

6.1.3 Choice of Measurement Location for Feedback Control

This master thesis has used a methodology-based approach on tuning of the control parameters. In accordance with suggestions from literature [8], the filter capacitor was neglected when designing the current control system. The simplification gave the impression of being an acceptable assumption based on the fact that C_f is present to filter out high-order frequency components. The validity of the adaption was verified by a sensitivity analysis which showed that the transfer function of the system was the same with and without C_f for frequencies up to around 280 Hz. The total filter inductance, L, became with this simplification the sum of L_f and L_t and it was natural to choose the point after L as the measurement location for the feedback control. Measuring the feedback control on the MV-side of the wind turbine transformer was advantageous from a tuning perspective as this allowed using modulus optimum to estimate the PI-controller parameters because of the resistance in the transformer. Since case 1 and 2 generated satis-

factory simulation results, the approach seemed adequate and was not questioned before high amounts of distortion were introduced when an up-scaled representation was connected to the grid in case 4.

6.1.4 Need for Additional Current Control Application

The principle of operation for the inner current control was described in Chapter 4. The same chapter also covered a thorough explanation of the tuning method applied. Fig. 6.1 illustrates the simplification of the LCL-filter which was used for the tuning of the current control parameter. Despite that neglecting C_f seemed to be an acceptable assumption for parameter tuning, the figure also illustrates how neglecting C_f causes an assumption of that the current flowing from the converter is the same as the current flowing to the grid.

A modified extract of the block diagram of the inner current control in Fig. 4.4 is presented in Fig. 6.2 and illustrates how the current control is implemented with regard to the filter. The illustration shows that using the MV-side of the wind turbine transformer should be okay when the filter is a basic L-filter or when one can assume that there is no current flowing through the capacitor. However, this control structure becomes problematic when the assumption does not hold and the current flowing thorough C_f is perceptible. It is believed that in those cases it is necessary with an additional control application in terms of for example a feed-forward of the capacitor current to compensate for the error. Another solution would be to measure the current before C_f. This control strategy will require additional filtering in the control system of the input signals.

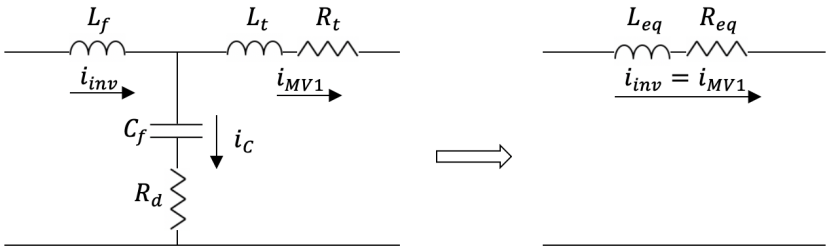

Figure 6.1: Simplification for parameter tuning of current control

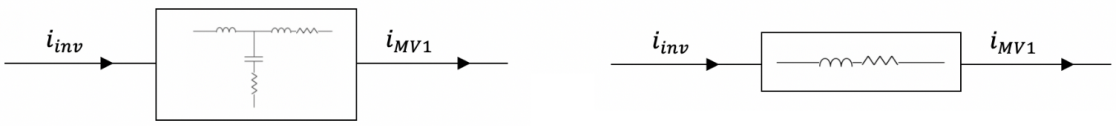

Figure 6.2: Block diagrams of current control with and without C_f as implemented in simulation model

The block diagrams show that it in principle should not matter whether the measurements

for feedback are taken on the LV or MV side of the wind turbine transformer since the two measurement points are both after the filter capacitor.

6.2 Contribution from Frequency Scan Analysis

The most striking finding from the frequency scan analysis was a significant and unpredictable magnitude variation for frequencies below 200 Hz. The response in the lowest frequency region differed under the various operating conditions without any clear coherence. The comparison of the different scenarios in converter A (30 wind turbines) in Fig. 5.25 showed that both changing the power injected and the DC voltage level caused significant variations in the response from the lowest frequency range. Variations were also observed when comparing the response from a single versus 30 wind turbine representation under equal operation conditions. In the latter comparison, the pu-representation of the converter should be identical. Hence, the comparison shows that the operation of the converter also must be affected by the physical values. At frequencies above 200 Hz, the data collected resulted in much smoother graphs and the results indicate that the major variation in the impedance magnitude in this frequency region is due to the load variations.

The results cannot directly give any further explanation to the introduction of the distortion issue introduced for case 4. However, it has been stated by M. K. Bakhshizadeh *et al.* that the effects of the outer control loops such as PLL and DC voltage control cannot be neglected in the lower frequency range around f_1 [50]. The paper comments that previous research has found that the PLL may introduce negative damping with a frequency coupling between the input voltage and output current. The frequency scan analysis has shown how susceptible the frequency response is to small changes in the lowest frequency range and it can therefore be argued that the results from the frequency scan of the converters do support the findings from the literature.

6.2.1 Development of Impedance Model

A frequency scan strategy based on manually varying the distorting frequency component is rather time consuming, especially as the control applications significantly increase the running time of each simulation. Therefore, it would be beneficial if the converters could be represented by an impedance model. With such a representation, the impedance measurement block can be used and frequency scan analysis from different locations in the grid can quickly be achieved with Simulink's impedance measurement block.

As previously stated, complex mathematical derivations and expressions of impedance models are outside the scope of this thesis. Therefore, it was tested if the data obtained from the frequency scan could be represented by a block in Simulink simply by transforming the data

in to a mathematical expression (i.e. a transfer function of the impedance). Matlab's System Identification Toolbox do among other things estimate transfer function models from data sets. Different combinations of poles and zeros of orders up to 30 were applied. However, the distinctive shape of the impedance plot made it difficult to create a mathematical function which was capable of recreating the impedance plot for frequencies below 200 Hz.

Chapter 7

Conclusion and Suggestion for Further Work

7.1 Conclusions Drawn From the Modelling Process of the Benchmark Systems

In this master thesis, it has been developed two functional simulation models that resemble the benchmark systems suggested by CIGRE's working group C4.49 *Multi-frequency stability of converter-based modern power systems*. The design of the control systems has followed a methodology-based approach and has been explained thoroughly.

The development of a simulation model for benchmark system 2 showed that the modelling strategy introduces a problem with the applied control system. The trouble introduced is believed to originate from an increasing difference in the energy storage capability of the filter inductors and the filter capacitor due to the scaling applied when the converters are representing several wind turbines. The problem is not expected to be present in reality as the real-life application consists of many separate units where the ratio between the filter inductors and filter capacitor is rather low. Since a model is supposed to recreate the reality as well as possible, this issue is a weakness with the adopted modelling strategy.

Simulation testing showed that the harmonic distortion was removed when the DC voltage level was reduced from 2000 V to 1720 V. With this change applied, the simulation model generated satisfactory responses and seemed ready for testing and further investigation/development. Investigation indicated that the reason for the success with the DC voltage adjustment is a sufficient regulation of an uncontrolled power flow between the DC and AC side of the converter due to the large filter capacitance. The required DC voltage level of 1720 V was derived from the energy equations for inductors and capacitors under the assumption that L_f should be capable of compensating for the charging- and discharging currents from the filter capacitor. Alterna-

tively to the solution with adjusting the DC voltage level, changes in the control structure can be applied.

7.2 Conclusions Drawn from Frequency Scan Analysis

A numerical approach in terms of frequency scan was applied to map the frequency response of the converters under various operating conditions. The frequency scan analyses showed a significant and hardly predictable magnitude variation for frequencies below 200 Hz. The impedance in this frequency region was susceptible to all the variations in the operating conditions applied: power injected, DC voltage level, and number of wind turbines represented.

7.3 Further Work Related to the Development of the Simulation Models

Further work to improve the simulation models of the benchmark systems and to analyze the phenomenon of concern for C4.49 is listed below.

1. Look into a control strategy that can compensate for the charging- and discharging currents from the filter capacitors.

2. Generate a frequency dependant impedance model of the converters based on numerical values as suggested by M. K. Bakhshizadeh *et al.* [50]. The impedance model allows Simulink to run frequency sweeps of the system with its internal impedance measurement block and can be a useful tool for predicting the frequencies where an interaction of a converter controller with a grid resonance can occur.

3. Implement active damping of the LCL-filter instead of passive damping with R_d since the presence of the resistor increases the power losses in the system.

4. Investigate the sensitivity of the grid-following converters when the grid is not modelled as an ideal AC voltage source. C4.49 has suggested a benchmark model where the wind farm cluster is interconnecting to a hypothetical HVDC transmission through a grid-forming converter. The HVAC/HVDC converter should at some point be included in the modelling, but a voltage source with a frequency dependent impedance that can mimic the frequency response of the real grid can be included as an intermediate step. Signals at frequencies different from the fundamental frequency should be injected to test how the converters respond.

5. Investigate how the system responds if harmonic compensation in terms of a compensating current for the amplified harmonic component is introduced. In reality, the compensation

current is i.e. coming from an active power filter. To start with, the compensating current can be modelled as a current source where its value is manually set based on the simulation results. Later, a proper model of a shunt active filter should be developed and implemented.

6. If the implementation of the active filter is functional and mitigates the distortion, a study of how the compensating current can be included as a control application in the converters should be done.

Appendices

A Parameters of the System

The subsequent tables present information provided by C4.49 about the cables, transformers, and the wind turbine which is used in the simulation model of the benchmark system.

Table 1: Cable data

Parameter	**Export cable (ABB)**	**Array cable (Nexans)**
Nominal voltage [kV]	220	34
Cross section [mm^2]	1000	630
AC resistance [Ω/km]	0.03	0.042
Inductance [mH/km]	0.38	0.31
Capacitance [μF/km]	0.19	0.32
Length [km]	100	3 (each section)

Table 2: Transformer data

Parameter	**400/220 kV**	**220/34 kV**	**34/1 kV**
Rated power [kV]	200	200	9
Leakage impedance [pu]	0.12	0.14	0.09
Copper losses [kW]	375	300	35

Table 3: Wind turbine data

Symbol	**Description**	**Value**
f_b	Nominal frequency	50 Hz
V_{dc}	DC link voltage	2000 V
P_{ref}	Active power set point	7 MW
C_f	Filter capacitance	3.3 mF
L_f	Coupling reactor	30 μH
f_{sw}	Switching frequency	2.5 kHz
K_p	Proportional gain of current controller	0.00007
K_i	Integrator gain of current controller	0.014
f_s	Sampling frequency	5 kHz
R_d	Damping resistor	1 mΩ

It should be noted that the parameters below the line in Table 3 are not included in the simulation model as other values have been used based on the methodology applied.

B Blocks from Simulation Model

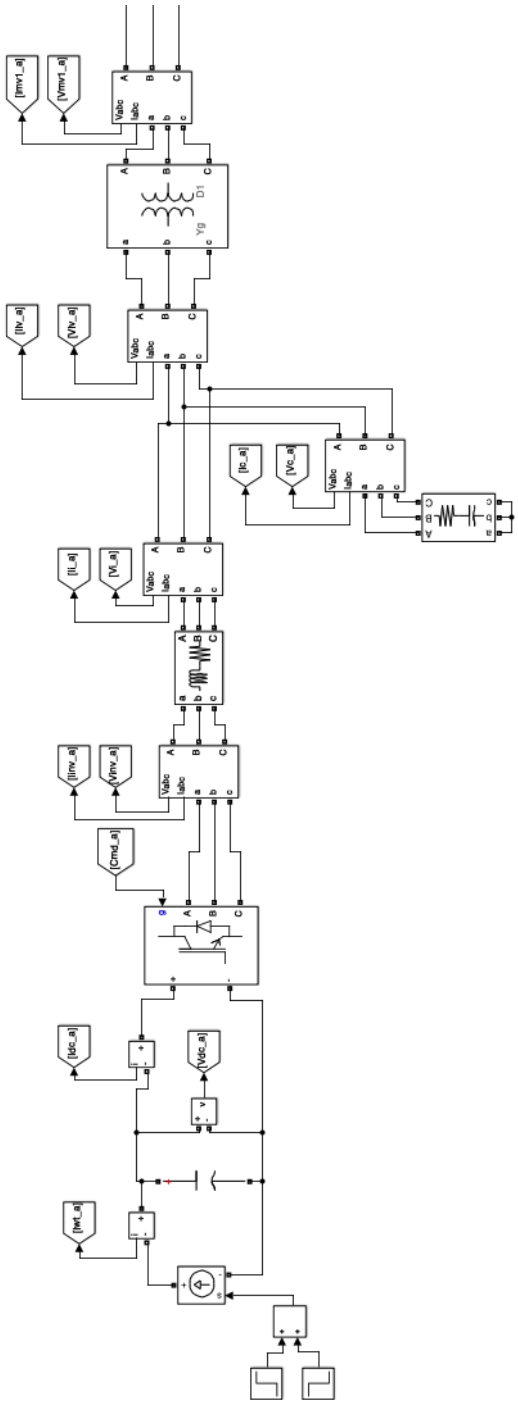

Figure 1: Generating unit A

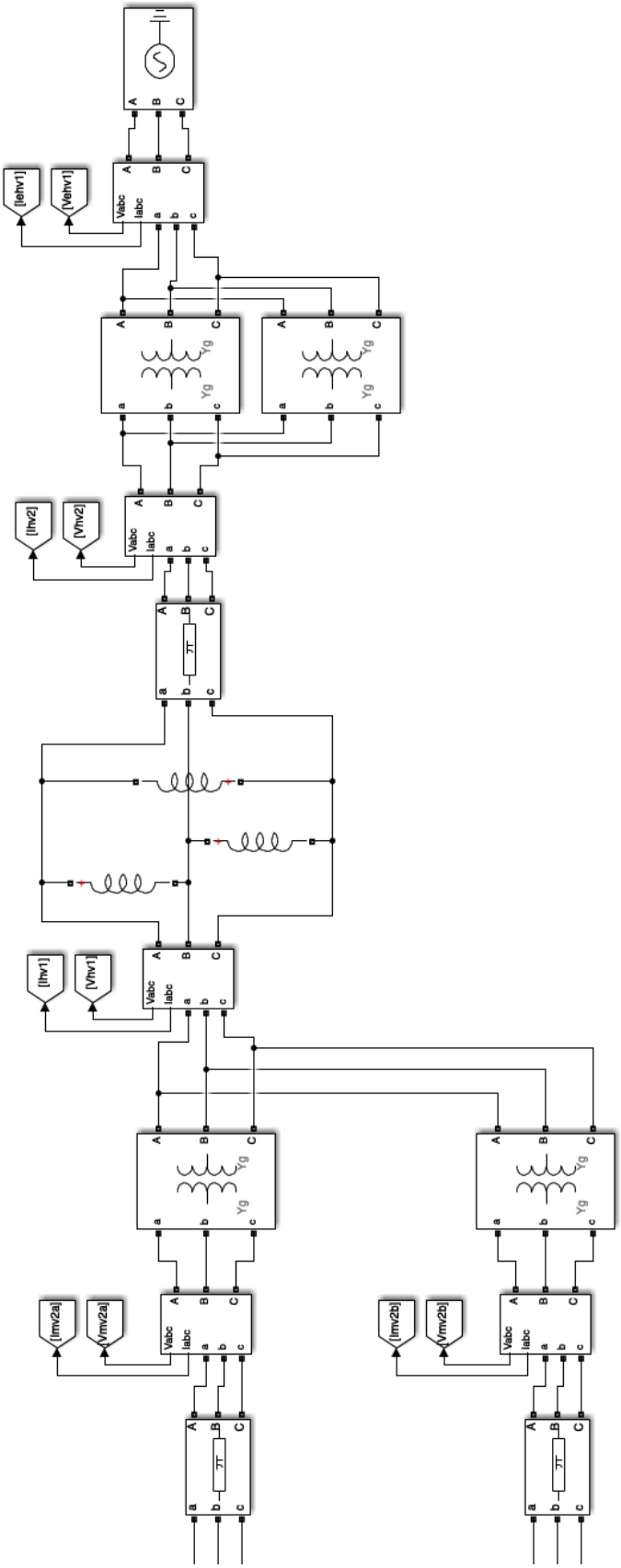

Figure 2: Model of the grid

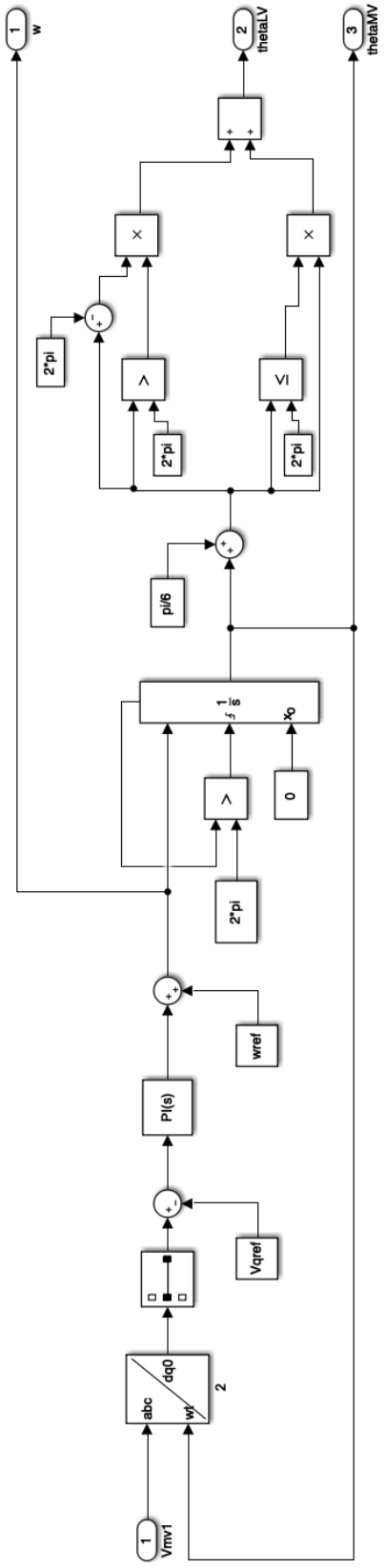

Figure 3: Phase-locked loop

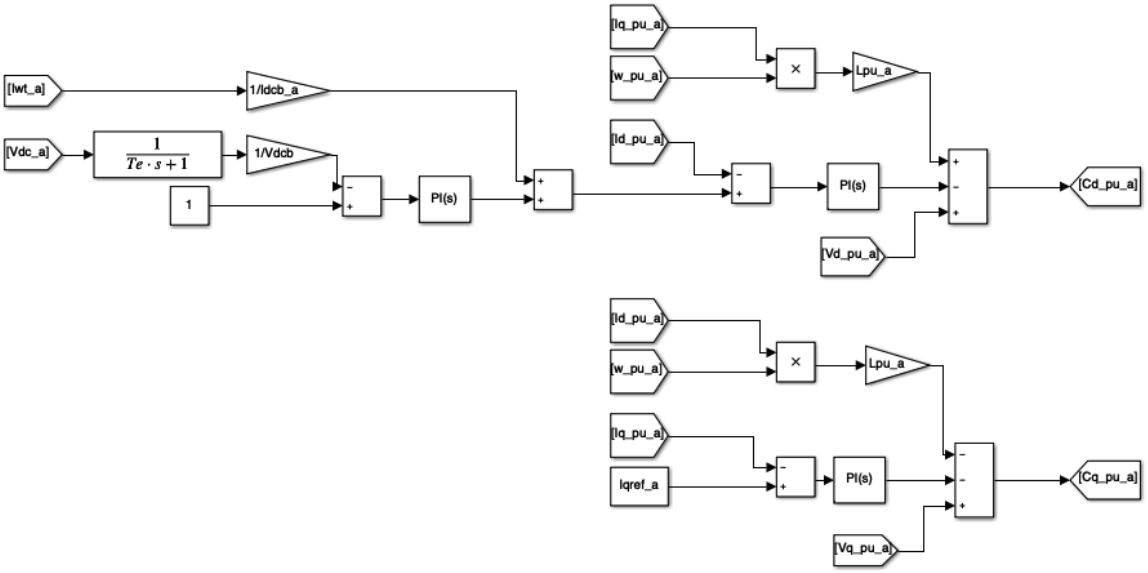

Figure 4: Control system for converter A

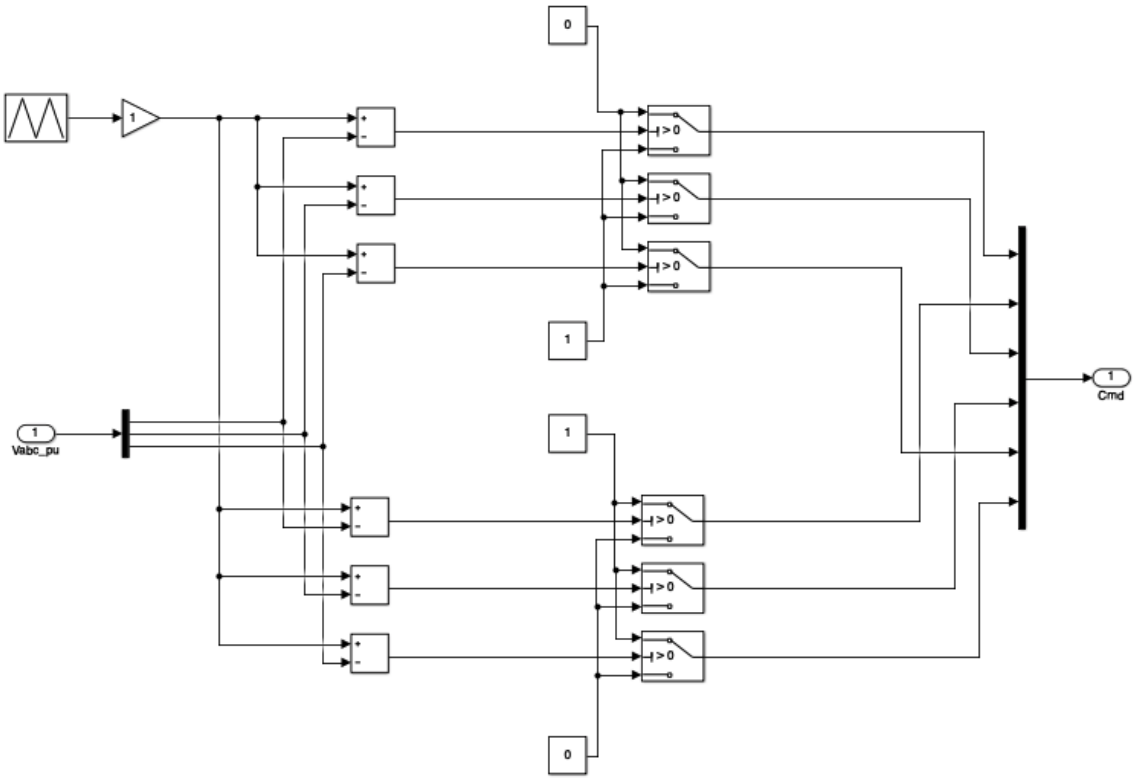

Figure 5: Pulse width modulator

C Matlab Script for Simulation Model

```
% Sample time: 1e-6;

%BASE VALUES, FREQUENCY
fb=50; %Grid frequency, Hz
wb=2*pi*fb;
fsw=2.5e3; %Switching frequency, Hz

Na=30;
Ma=6;
Nb=28;
Mb=7;

%BASE VALUES, GENERAL 1WT a
Sb_a=9e6*Na; %Sn, based on LV/MV transformer
Vll=1000; %V, rms of line-to-line voltage
Vb=sqrt(2)/sqrt(3)*Vll; %peak of phase to ground voltage
Ib_a=2/3*Sb_a/Vb;
Zb_a=Vb/Ib_a;

Vdcb=1720;

Idcb_a=Sb_a/Vdcb;
Zdcb_a=Vdcb/Idcb_a;

%BASE VALUES, GENERAL 1WT b
Sb_b=9e6*Nb; %Sn, based on LV/MV transformer
Ib_b=2/3*Sb_b/Vb;
Zb_b=Vb/Ib_b;
Idcb_b=Sb_b/Vdcb;
Zdcb_b=Vdcb/Idcb_b;

%Transformer LV/MV
fnLV=fb;
PnomLV=9e6;
VllLV=1000;
ZbLV=VllLV^2/PnomLV;

PlossLV=35e3;
ILV=PnomLV/(sqrt(3)*VllLV);
RtLV=(PlossLV/3)/ILV^2;
```

```
41 RtLVpu=RtLV/ZbLV;
42 Rt1LV=RtLVpu/2; %pu
43 Rt2LV=RtLVpu/2; %pu
44 RmLV=500; %pu, magnetization resistance (default value:500)
45 Lt1LV=0.09/2; %pu
46 Lt2LV=0.09/2; %pu
47 LmLV=500; %pu, magnetization inductance (default value:500)
48
49 %Transformer MV/HV
50 fnMV=fb;
51 PnomMV=200e6;
52 VllMV=34e3;%V1 ph-ph (Vrms)
53 ZbMV=VllMV^2/PnomMV;
54 VbMV=sqrt(2)/sqrt(3)*VllMV; %for plotting
55 IbMV=2/3*PnomMV/VbMV; %for plotting
56
57 PlossMV=300e3;
58 IMV=PnomMV/(sqrt(3)*VllMV);
59 RtMV=(PlossMV/3)/IMV^2;
60 RtMVpu=RtMV/ZbMV;
61 Rt1MV=RtMVpu/2; %pu
62 Rt2MV=RtMVpu/2; %pu
63 RmMV=500; %pu, magnetization resistance (default value:500)
64 Lt1MV=0.14/2; %pu
65 Lt2MV=0.14/2; %pu
66 LmMV=500; %pu, magnetization inductance (default value:500)
67
68 %Transformer HV/EHV
69 fnHV=fb;
70 PnomHV=200e6;
71 VllHV=220e3; %V1 ph-ph (Vrms)
72 VllEHV=400e3;
73 ZbHV=VllHV^2/PnomHV;
74 VbHV=sqrt(2)/sqrt(3)*VllHV; %for plotting
75 IbHV=2/3*PnomHV/VbHV; %for plotting
76 VbEHV=sqrt(2)/sqrt(3)*VllEHV; %for plotting
77 IbEHV=2/3*PnomHV/VbEHV; %for plotting
78
79 PlossHV=375e3;
80 IHV=PnomHV/(sqrt(3)*VllHV);
81 RtHV=(PlossHV/3)/IHV^2;
82 RtHVpu=RtHV/ZbHV;
```

```
Rt1HV=RtHVpu/2; %pu
Rt2HV=RtHVpu/2; %pu
RmHV=500; %pu, magnetization resistance (default value:500)
Lt1HV=0.12/2; %pu
Lt2HV=0.12/2; %pu
LmHV=500; %pu, magnetization inductance (default value:500)

%Parameters, 1WT a
R_igbt=1e-8; %Default in Simulink is 1e-3
deltaVdc=0.05*Vdcb;
Cdc_a=1/(4*fsw)*Ib_a/(deltaVdc);
Cdcpu_a=(1/(wb*Cdc_a))/Zdcb_a;
Lf_a=30e-6/Na;
Lfpu_a=wb*Lf_a/Zb_a;
Rf_a=0;
Rfpu_a=Rf_a/Zb_a;
Cf_a=3.3e-3*Na;
Cfpu_a=(1/(wb*Cf_a))/Zb_a;
Ltrafo_pu_a=(Lt1LV+Lt2LV);
Ltrafo_a=Ltrafo_pu_a*Zb_a/wb;
wres_a=sqrt((Lf_a+Ltrafo_a)/(Lf_a*Ltrafo_a*Cf_a));
Rd_a=(1/(3*wres_a*Cf_a));
Rdpu_a=Rd_a/Zb_a;

%Parameters, 1WT b
Cdc_b=1/(4*fsw)*Ib_b/(deltaVdc);
Cdcpu_b=(1/(wb*Cdc_b))/Zdcb_b;
Lf_b=30e-6/Nb;
Lfpu_b=wb*Lf_b/Zb_b;
Rf_b=0;
Rfpu_b=Rf_b/Zb_b;
Cf_b=3.3e-3*Nb;
Cfpu_b=(1/(wb*Cf_b))/Zb_b;
Ltrafo_pu_b=(Lt1LV+Lt2LV);
Ltrafo_b=Ltrafo_pu_b*Zb_b/wb;
wres_b=sqrt((Lf_b+Ltrafo_b)/(Lf_b*Ltrafo_b*Cf_b));
Rd_b=1/(3*wres_b*Cf_b);
Rdpu_b=Rd_b/Zb_b;

%GRID IMPEDANCES
%Export cable
lHV=100; %km
```

```
RgHV=0.03*lHV; %ohm
LgHV=0.38e-3*lHV; %H
CgHV=0.19e-6*lHV; %F
%MV array cable:
lWT=3;
%Zn_m,cable impedance between two WT:
RgMV=0.042*lWT; %ohm
LgMV=0.31e-3*lWT; %H
CgMV=0.32e-6*lWT; %F
%a
eq_a=1/5*(1+2+3+4+5); %equivalent impedance factor for one radial
RgMVa=RgMV*eq_a/Ma; % thevenin eq. of radials in parallel
LgMVa=LgMV*eq_a/Ma; % thevenin eq. of radials in parallel
CgMVa=CgMV/(eq_a/Ma); % thevenin eq. of radials in parallel
%b
eq_b=1/4*(1+2+3+4); %equivalent impedance factor for one radial
RgMVb=RgMV*eq_b/Mb; % thevenin eq. of radials in parallel
LgMVb=LgMV*eq_b/Mb; % thevenin eq. of radials in parallel
CgMVb=CgMV/(eq_b/Mb); % thevenin eq. of radials in parallel

%Shunt Reactor
Lsr=1.63;

%CONTROL SYSTEM, a
Idref_a=1;
Iqref_a=0;
Lpu_a=Lfpu_a+Ltrafo_pu_a;
Rpu_a=Rfpu_a+(Rt1LV+Rt2LV);
%PI-controller, Current control
Tsw=1/fsw;
Te=1.5*Tsw; % total delay
%e_c=1/sqrt(2);
e_c=1;
Kpc_a=Lpu_a/(2^2*e_c^2*wb*Te);
tauc_a=Lpu_a/(wb*Rpu_a);
Kic_a=Kpc_a/tauc_a;

%PI-controller, Voltage control
Tc_a=1/(wb*Cdcpu_a);
Vdpu=1;
Vdcpu=1;
K=Vdpu/Vdcpu;
```

```
167 Teq=2*Te;
168 a=2;
169 Tdcpu_a=Teq*a^2;
170 Kpv_a=Tc_a/(K*Teq*a);
171 Kiv_a=Kpv_a/Tdcpu_a;
172
173 %CONTROL SYSTEM, b
174 Idref_b=1;
175 Iqref_b=0;
176 Lpu_b=Lfpu_b+Ltrafo_pu_b;
177 Rpu_b=Rfpu_b+(Rt1LV+Rt2LV);
178 %PI-controller, Current control
179 Kpc_b=Lpu_b/(2^2*e_c^2*wb*Te);
180 tauc_b=Lpu_b/(wb*Rpu_b);
181 Kic_b=Kpc_b/tauc_b;
182 %PI-controller, Voltage control
183 Tc_b=1/(wb*Cdcpu_b);
184 Tdcpu_b=Teq*a^2;
185 Kpv_b=Tc_b/(K*Teq*a);
186 Kiv_b=Kpv_b/Tdcpu_b;
187
188 %PLL
189 e_pll=1;
190 wn=2*pi*10;
191 Vqref=0;
192 Kppll=2*e_pll*wn;
193 Kipll=wn^2;
194 wref=wb;
195
196 Vsource=sqrt(2)/sqrt(3)*VllEHV;
```

D Low-Order Harmonics in Benchmark System

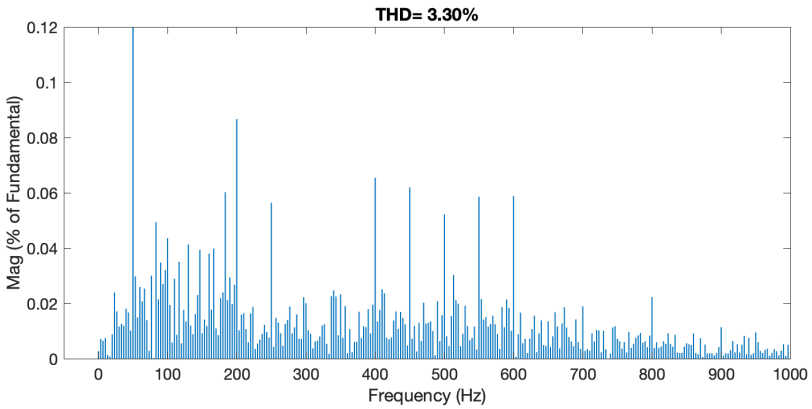

Figure 6: Close-up of voltage harmonic components at MV1a with rated power injected

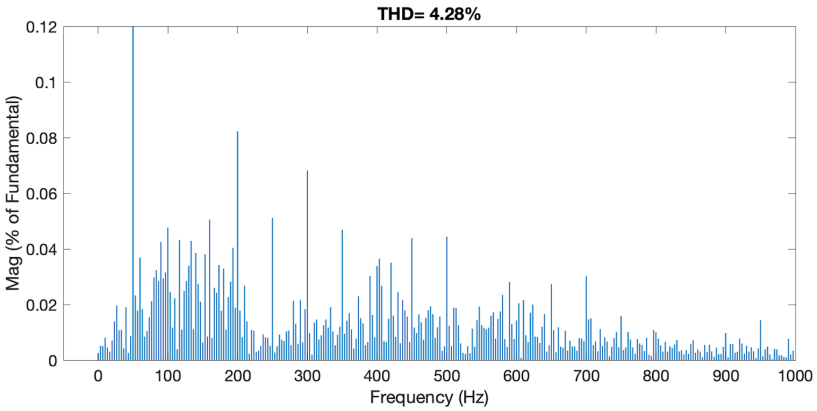

Figure 7: Close-up of voltage harmonic components at MV1b with rated power injected

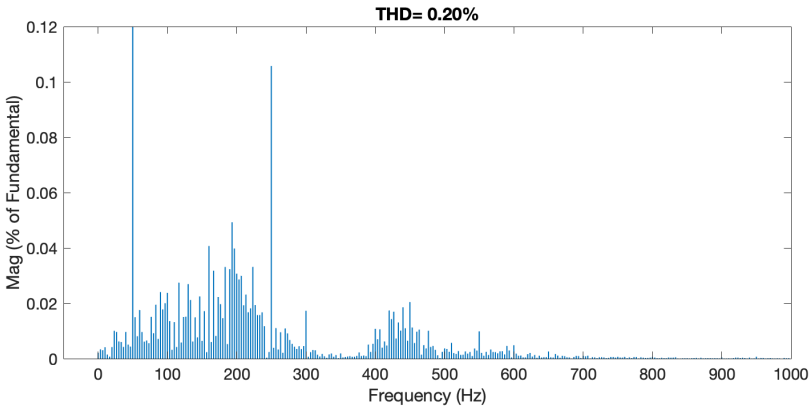

Figure 8: Close-up of voltage harmonic components at HV1 with rated power injected

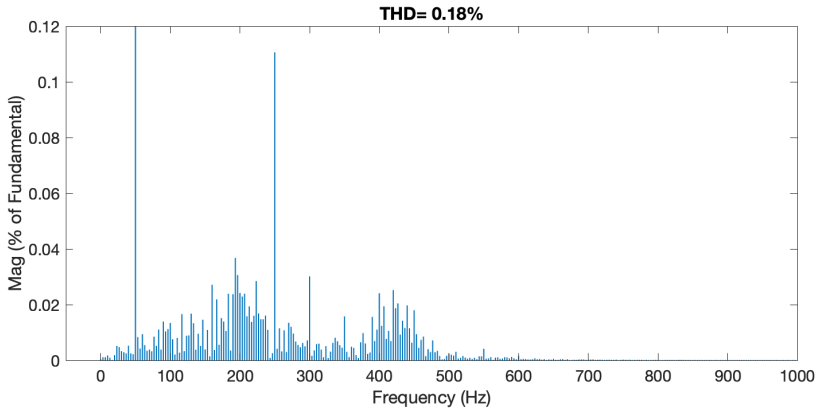

Figure 9: Close-up of voltage harmonic components at HV2 with rated power injected

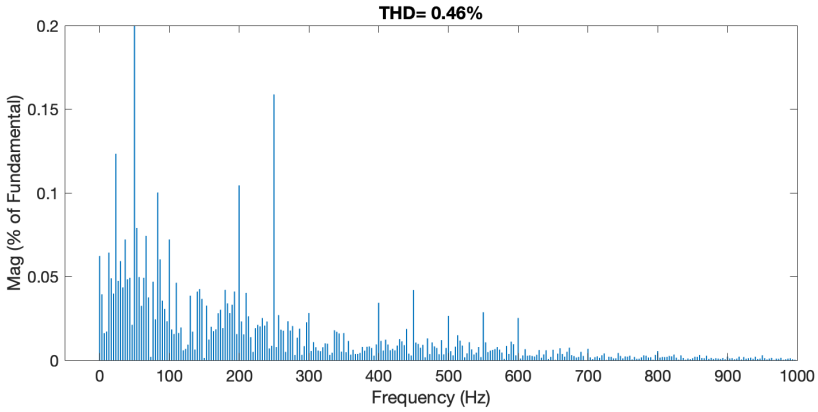

Figure 10: Close-up of current harmonic components at MV1a with rated power injected

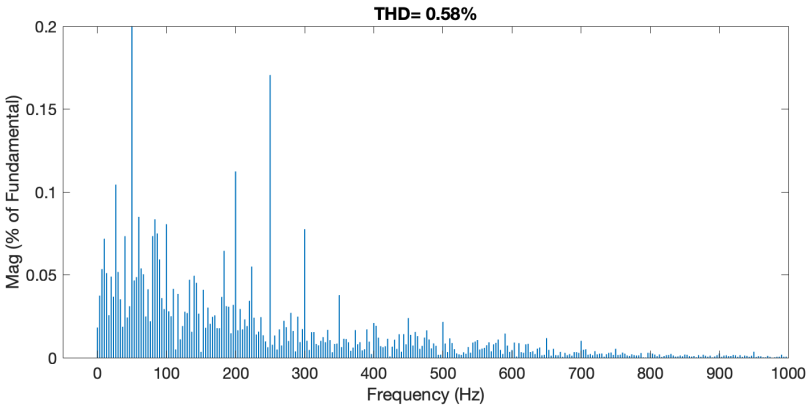

Figure 11: Close-up of current harmonic components at MV1b with rated power injected

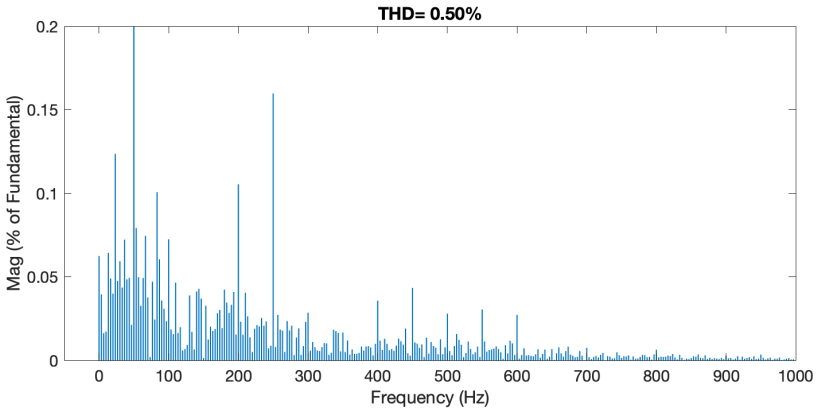

Figure 12: Close-up of current harmonic components at HV1 with rated power injected

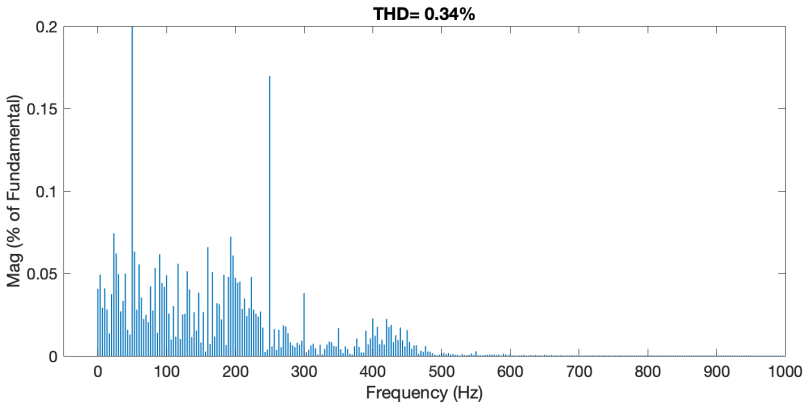

Figure 13: Close-up of current harmonic components at HV2 with rated power injected

Bibliography

[1] "Wind energy data." https://www.irena.org/wind, Feb. 2019.

[2] IRENA, "Global energy transformation: A roadmap to 2050," *International Renewable Energy Agency, Abu Dhabi*, 2018.

[3] V. Yaramasu, B. Wu, P. C. Sen, S. Kouro, and M. Narimani, "High-power wind energy conversion systems: State-of-the-art and emerging technologies," *Proceedings of the IEEE*, vol. 103, pp. 740–788, May 2015.

[4] L. H. Kocewiak, J. Hjerrild, and C. L. Bak, "Wind turbine converter control interaction with complex wind farm systems," *IET Renewable Power Generation*, vol. 7, pp. 380–389, July 2013.

[5] L. H. Kocewiak, B. L. Kramer, O. Holmstrøm, K. H. Jensen, and L. Shuai, "Resonance damping in array cable systems by wind turbine active filtering in large offshore wind power plants," *IET Renewable Power Generation*, vol. 11, no. 7, pp. 1069–1077, 2017.

[6] M. Lehmann, M. Pieschel, H. Kocewiak, M. Juamperez, S. Sahukari, and K. Kabel, "Active filtering with large-scale statcom for the integration of offshore wind power," in *Proc. The 17th International Workshop on Large-Scale Integration of Wind Power into Power Systems as well as Transmission Networks for Offshore Wind Farms*, (Stockholm, Sweden), 2018.

[7] T. Ackermann, *Wind Power in Power Systems*. Chichester, UK: John Wiley & Sons, Ltd, 2005.

[8] R. Teodorescu, M. Liserre, and P. Rodríguez, *Grid Converters for Photovoltaic and Wind Power Systems*. Chichester, UK: John Wiley & Sons, Ltd, 2011.

[9] L. H. Kocewiak, "Proposal for the creation of a new working group: Multi-frequency stability of converter-based modern power systems." https://www.cigre.org/userfiles/files/News/2018/TOR_WG_C4_49_Multi_frequency_stability_of_converter_based_modern_power_systems.pdf, Mar. 2018. CIGRE Study Committee C4.

[10] "Introducing CIGRE." https://www.cigre.org/GB/about/introducing-cigre, Jan. 2019.

[11] L. Motta and N. Faúndes, "Active / passive harmonic filters: Applications, challenges amp; trends," in *2016 17th International Conference on Harmonics and Quality of Power (ICHQP)*, pp. 657–662, Oct 2016.

[12] "IEEE Recommended Practice and Requirements for Harmonic Control in Electric Power Systems," *IEEE Std 519-2014 (Revision of IEEE Std 519-1992)*, pp. 1–29, June 2014.

[13] J. Arrillaga, *Power system harmonics*. West Sussex, England: J. Wiley & Sons, 2nd ed., 2003.

[14] E. W. Weisstein, "Fourier Series. From MathWorld - A Wolfram Web Resource." `http://mathworld.wolfram.com/FourierSeries.html`, Feb. 2019.

[15] N. Mohan, *Power electronics : converters, applications, and design*. Hoboken, N.J: Wiley, 3rd ed. ed., 2003.

[16] Y. Xue, D. Finney, and B. Le, "Charging current in long lines and high-voltage cables – protection application considerations," in *67th Annual Georgia Tech Protective Relaying Conference Atlanta, Georgia*, May 8–10, 2013.

[17] J. C4/B4.38, "Network modelling for harmonic studies," tech. rep., CIGRE, Apr. 2019.

[18] J. W. Nilsson, *Electric circuits*. Boston: Prentice Hall, 9th ed., 2011.

[19] E. Tedeschi, "Specialication course: Elk-23 power electronics in future power systems, lecture 12: Lecture notes." `https://ntnu.blackboard.com/bbcswebdav/pid-510916-dt-content-rid-18540633_1/courses/MERGE_TET4515_TET4525_TET4535_TET5505_H18/Lecture_12_2018ns.pdf`, Nov. 2018.

[20] E. Twining and D. G. Holmes, "Grid current regulation of a three-phase voltage source inverter with an lcl input filter," *IEEE Transactions on Power Electronics*, vol. 18, pp. 888–895, May 2003.

[21] D. Dhua, G. Yang, Z. Zhang, Kocewiak, and A. Timofejevs, "Harmonic active filtering and impedance-based stability analysis in offshore wind power plants," in *Proceedings of 16th Wind Integration Workshop*, IEEE, 2017.

[22] L. Kocewiak, J. Hjerrild, and C. Bak, "Harmonic analysis of offshore wind farms with full converter wind turbines," in *Proceeding of the 8th International Conference on Large-Scale Integration of Wind Power into Power Systems*, Energynautics GmbH, 2009.

[23] S. Sen, K. Yenduri, and P. Sensarma, "Step-by-step design and control of LCL filter based three phase grid-connected inverter," in *2014 IEEE International Conference on Industrial Technology (ICIT)*, pp. 503–508, Feb 2014.

[24] Y. Tang, P. C. Loh, P. Wang, F. H. Choo, and F. Gao, "Exploring Inherent Damping

Characteristic of LCL-Filters for Three-Phase Grid-Connected Voltage Source Inverters," *IEEE Transactions on Power Electronics*, vol. 27, pp. 1433–1443, March 2012.

[25] A. Reznik, M. G. Simões, A. Al-Durra, and S. M. Muyeen, "LCL-Filter Design and Performance Analysis for Grid-Interconnected Systems," *IEEE Transactions on Industry Applications*, vol. 50, pp. 1225–1232, March 2014.

[26] L. Malesani, L. Rossetto, P. Tenti, and P. Tomasin, "AC/DC/AC PWM converter with reduced energy storage in the DC link," *IEEE Transactions on Industry Applications*, vol. 31, pp. 287–292, March 1995.

[27] M. Vujacic, M. Hammami, M. Srndović, and G. Grandi, "Analysis of dc-Link Voltage Switching Ripple in Three-Phase PWM Inverters," *Energies*, vol. 11, p. 471, 02 2018.

[28] H. Brantsæter, L. Kocewiak, A. Rygg, and E. Tedeschi, "Passive Filter Design and Offshore Wind Turbine Modelling for System Level Harmonic Studies," *Energy Procedia*, vol. 80, pp. 401–410, 12 2015.

[29] S. D'Arco, J. A. Suul, and M. Molinas, "Implementation and analysis of a control scheme for damping of oscillations in VSC-based HVDC grids," in *2014 16th International Power Electronics and Motion Control Conference and Exposition*, pp. 586–593, Sep. 2014.

[30] L. Kocewiak, *Harmonics in large offshore wind farms*. PhD thesis, Department of Energy Technology, Aalborg University, 2012.

[31] P. S. Nascimento Filho, T. A. dos Santos Barros, M. G. Villalva, and E. Ruppert Filho, "Design methodology of P-res controllers with harmonic compensation for three-phase DC-AC grid-tie inverters with LCL output filter," in *2014 IEEE 15th Workshop on Control and Modeling for Power Electronics (COMPEL)*, pp. 1–8, June 2014.

[32] C. Bajracharya, M. Molinas, J. Suul, and T. M. Undeland, "Understanding of Tuning Techniques of Converter Controllers for VSC-HVDC," 06 2008.

[33] F. Blaabjerg, R. Teodorescu, M. Liserre, and A. V. Timbus, "Overview of Control and Grid Synchronization for Distributed Power Generation Systems," *IEEE Transactions on Industrial Electronics*, vol. 53, pp. 1398–1409, Oct 2006.

[34] "abc to Alpha-Beta-Zero, Alpha-Beta-Zero to abc." `https://se.mathworks.com/help/physmod/sps/powersys/ref/abctoalphabetazeroalphabetazerotoabc.html`, Dec. 2018.

[35] "Alpha-Beta-Zero to dq0, dq0 to Alpha-Beta-Zero." `https://se.mathworks.com/help/physmod/sps/powersys/ref/alphabetazerotodq0dq0toalphabetazero.html`, Dec. 2018.

[36] L. Harnefors, M. Bongiorno, and S. Lundberg, "Input-Admittance Calculation and Shaping

for Controlled Voltage-Source Converters," *IEEE Transactions on Industrial Electronics*, vol. 54, pp. 3323–3334, Dec 2007.

[37] K. Ogata, *Modern control engineering*. Upper Saddle River, N.J: Prentice-Hall, 4th ed., 2002.

[38] M. Liserre, F. Blaabjerg, and S. Hansen, "Design and control of an LCL-filter-based three-phase active rectifier," *IEEE Transactions on Industry Applications*, vol. 41, pp. 1281–1291, Sep. 2005.

[39] E. Tedeschi, "Specialication course: Elk-23 power electronics in future power systems, lecture 4: Lecture notes." `https://ntnu.blackboard.com/bbcswebdav/pid-462047-dt-content-rid-17398600_1/courses/MERGE_TET4515_TET4525_TET4535_TET5505_H18/VSC_Modeling_and_Control_Lecture_notes_2A_2017.pdf`, Sept. 2018.

[40] S. Sanchez, *Stability Investigation of Power Electronics Systems; A Microgrid Case*. PhD thesis, 2015.

[41] F. Marafao, S. Deckmann, J. Pomilio, and R. Machado, "Software-based PLL model: analysis and applications," 01 2004.

[42] A. M. dos Santos Alonso, "Distributed Harmonic Compensation in Single-Phase Low-Voltage Microgrids," Master's thesis, Universidade Estadual Paulista, 2018.

[43] E. V. Liberado, *Design and control of a power quality interface and its cooperation with distributed switching power interfaces*. PhD thesis, Universidade Estadual de Campinas, 2017.

[44] E. Tedeschi, "Specialication cource: Elk-23 power electronics in future power systems, lecture 5: Lecture notes." `https://ntnu.blackboard.com/bbcswebdav/pid-470173-dt-content-rid-17542089_1/courses/MERGE_TET4515_TET4525_TET4535_TET5505_H18/Lecture_notes3A.pdf`, Sept. 2018.

[45] J. D. Glover, *Power system analysis and design*. Stamford, Conn: Cengage Learning, 5th ed., 2012.

[46] M. H. Rashid, *Power Electronics Handbook*. Butterworth Heinemann, 3rd ed., 2011.

[47] M. Cespedes and J. Sun, "Impedance modeling and analysis of grid-connected voltage-source converters," *IEEE Transactions on Power Electronics*, vol. 29, pp. 1254–1261, March 2014.

[48] M. Kazem Bakhshizadeh, X. Wang, F. Blaabjerg, J. Hjerrild, Kocewiak, C. L. Bak, and B. Hesselbæk, "Couplings in phase domain impedance modeling of grid-connected converters," *IEEE Transactions on Power Electronics*, vol. 31, pp. 6792–6796, Oct 2016.

[49] "Impedance Measurement." `https://se.mathworks.com/help/physmod/sps/powersys/ref/impedancemeasurement.html`, June 2019.

[50] M. K. Bakhshizadeh, J. Hjerrild, L. Kocewiak, B. Hesselbaek, F. Blaabjerg, C. Bak, X. Wang, and F. Faria da Silva, "A numerical matrix-based method in harmonic studies in wind power plants," 11 2016.